

**Development of Fe-Ni based Metal Amorphous Nanocomposites for Electric
Motor Applications**

Submitted in partial fulfillment of the requirements for

the degree of

Doctor of Philosophy

in

Materials Science and Engineering

Natan M. Aronhime

B.S., Materials Science and Engineering, University of Maryland, College Park
M.S., Materials Science and Engineering, Carnegie Mellon University

Carnegie Mellon University
Pittsburgh, PA

August, 2018

© Natan M. Aronhime, 2018
All Rights Reserved

Acknowledgements

I'd like to thank my advisor, Prof. Michael McHenry, for bringing me onto his group, allowing me to conduct interesting and challenging research. His advice and his guidance over the last four years have been instrumental and his expertise has helped shape this work. I would also like to thank my committee members, Prof. Laughlin, Prof. Sokalski, and Dr. Ohodnicki for their help, ideas, and for always making time to chat when needed.

I am also grateful to my colleagues, Alex Leary, Vincent DeGeorge, Whitney Schoenthal, Michael Kurniawan, Alice Perrin, Yuval Krimer, Satoru Simizu, and Nazu for their help and camaraderie. I'd like to especially thank Vladimir Keylin, Alex Leary, and Vincent DeGeorge for teaching me many of the experimental techniques used throughout this thesis.

This work could not have been completed without the support of CMU's Materials Characterization Facility and its staff. I'd especially like to thank Adam Wise and Betsy Clark for all their help with TEM and XRD. I'd also like to thank Andrew Gamble with the Data Storage Systems Center for his help with the VSM tools.

I'd like to thank the ORISE program administered by ORAU and the DOE Solar Energy Technology Office and the Grid Modernization Laboratory Consortium through the SuNLAMP initiative under agreement #DE-EE-00031004 for financial support.

Finally, I'd like to thank my family for all of their love and support. My wife Yaella has been a constant source of strength, stability, inspiration, and

motivation. She has kept my spirits up, and without her care and laughter, much of this could not have happened. My son Nissim is a constant source of joy and wonder, and demonstrates daily that life is about learning and experimentation.

Abstract

Metal amorphous nanocomposite (MANC) soft magnetic materials (SMMs) offer a transformational technology to increase efficiency and limit rare-earth use for high-power, high-torque-density motors. These materials consist of nanocrystals that are usually ~ 10 nm in diameter embedded in an amorphous matrix. MANC SMMs can have usable peak inductions comparable to Si-steels with resistivities that allow the high switching frequencies required for high torques. High-frequency switching allows motor size reduction, thereby minimizing volume and weight and can enable new high-efficiency motor designs. In this thesis, Fe-Ni based MANCs are developed along with the analysis on their structural composition, crystallization kinetics, and magnetic properties.

A broad Fe-Ni composition space is explored, and an $(\text{Fe}_{70}\text{Ni}_{30})_{80}\text{Nb}_4\text{Si}_2\text{B}_{14}$ alloy is determined as being of primary interest. Crystallization products are determined to be both bcc and fcc for primary crystallization, while secondary crystallization produces an Cr_{23}B_6 phase. TTT diagrams for primary and secondary crystallization are determined for $(\text{Fe}_{70}\text{Ni}_{30})_{80}\text{Nb}_4\text{Si}_2\text{B}_{14}$ as well as for a Cu-containing alloy. Adding Cu was found to increase the crystallization rate for both primary and secondary crystallization. This is accompanied by a lowering of the Avrami exponent from 2.5 to 1.5. Magnetic properties are explored in depth, and strain-annealing is introduced as an effective method of tuning the permeability. In $(\text{Fe}_{70}\text{Ni}_{30})_{80}\text{Nb}_4\text{Si}_2\text{B}_{14}$, it increases the permeability from 40,000 to 16,000.

Adding dilute amounts of other early transition elements is found to effectively increase the resistivity, although permeability is affected as well. The base alloy has a resistivity of about 135 $\mu\Omega\text{-cm}$, while adding early transition elements can increase it to over 200 $\mu\Omega\text{-cm}$ while maintaining reasonable magnetic properties. Toroidal losses are measured and compared to other alloys in the literature and/or commercially available. $(\text{Fe}_{70}\text{Ni}_{30})_{80}\text{Nb}_4\text{Si}_2\text{B}_{14}$ was found to have losses of 2.1 W/kg and 6.0 W/kg at 1 T, 400 Hz, and 1 T, 1 kHz respectively. These losses are fit to the Steinmetz equation with fitting parameters. These fitting parameters are then used in COMSOL modeling of a switched reluctance motor, and are compared to a motor comprised of a 3.5%Si-steel.

Table of Contents

I. Introduction	1
<i>i. Context within the Materials Science Paradigm</i>	1
<i>ii. Motivation</i>	2
<i>iii. Fundamentals of Soft Magnetic Materials</i>	5
<i>iv. Historical development</i>	6
<i>v. The Bulk Fe-Ni Alloy System</i>	10
<i>vi. Losses</i>	11
<i>vii. MANC Synthesis</i>	15
II. Hypotheses	19
III. Crystallization Kinetics	20
<i>i. JMAK Kinetics</i>	20
<i>ii. Rigid Band Theory, Cohesive Energy, and the Slater-Pauling Curve</i>	22
<i>iii. Trends in Primary and Secondary Crystallization Temperatures</i>	24
<i>iv. Kinetics from Thermal Analysis and the Kissinger Equation</i>	26
<i>v. Activation Energy Determination from Thermal Analysis</i>	29
<i>vi. TTT Diagram Determination</i>	32
<i>vii. Kinetics from Magnetometry</i>	35
<i>viii. Strain-Annealing and Elongation</i>	36
<i>ix. Conclusions</i>	38
IV. Structure	39
<i>i. Basics of X-ray Diffraction</i>	39
<i>ii. Energy Dispersive XRD and Pressure</i>	40
<i>iii: Crystallization and Pressure Effects in the Fe-Nd-B system</i>	41
<i>iv. Allotropes and the Thermodynamics of Phase Transitions in Iron</i>	45
<i>v. Crystallization Products in the Fe-Ni MANC System</i>	47
<i>vi. Pressure Effects on Crystallization in the Fe-Ni MANC System</i>	54
<i>vii. Atom Probe Tomography</i>	58
<i>viii. Conclusions</i>	60
V. Magnetism and Magnetic Properties of Fe-Ni MANCs	62
<i>i. Methods for Magnetization Measurement</i>	62
<i>ii. Magnetic Dipoles, Susceptibility, and Permeability</i>	62
<i>iii. Mean Field Theory</i>	63
<i>iv. Heisenberg Exchange</i>	65
<i>v. Bethe-Slater Curve and Distributed Exchange</i>	66
<i>vi. Domains and Domain Walls</i>	67
<i>vii. Magnetostriction and Magnetic Anisotropy</i>	68
<i>viii. Magnetization and T_c trends in Fe-Ni MANCs</i>	70
<i>ix. Low Temperature Magnetic Phenomena</i>	71
<i>x. Strain-Annealing effects on B-H Loops</i>	72
<i>xi. Density of States and the Electronic Structure</i>	74
<i>xii. Resistivity</i>	76
<i>xiii. Virtual Bound States (VBS) and Resistivity</i>	78
<i>xiv. Effects of VBS Elements on Magnetic properties</i>	82
<i>xv. Introduction to FORC and the Preisach Distribution</i>	84
<i>xvi. Conclusions</i>	86
VI. Performance	88

<i>i. Toroidal Losses</i>	88
<i>ii. COMSOL Modeling</i>	91
<i>iii. Conclusions</i>	94
VII. Conclusions and Future Work	95
References:	98

Table of Figures

Figure 1.1: Global end-use of electricity	2
Figure 1.2: Price of Neodymium oxide from 2009-2015.....	3
Figure 1.3: (a) a model hysteresis loop for a permanent magnet, and (b) a model hysteresis loop for a soft magnet	6
Figure 1.4: Permeability and saturation induction for a variety of soft magnetic materials.....	7
Figure 1.5: Binary phase diagram for Fe-Ni.....	10
Figure 1.6: Comparison of the three sources of losses per magnetic cycle	13
Figure 1.7: Figure (a) Schematic of planar flow casting an amorphous alloy. (b) Detail of nozzle, melt puddle and solid ribbon.....	15
Figure 1.8: Illustration of T_0 diagram construction for a binary alloy.....	17
Figure 1.9: Sketch of Gibb's free energy curves for a liquid and two solid phases. Where the liquid intersects the solid lines are T_0 points.....	18
Figure 3.1: Schematic of primary crystallization and soft impingement. (a) Start of crystallization with small crystals and large glass former concentration gradient. (b) Intermediate stage, and (c) soft impingement	21
Figure 3.2: Cohesive energies for period 4 metals	22
Figure 3.3: The Slater-Pauling curve	23
Figure 3.4: (a) Crystallization temperature vs. electrons/atom. (b) Typical DSC curve showing exothermic peaks for primary and secondary crystallization with a heating rate of 40 °C/min	24
Figure 3.5: Kissinger plots for $(\text{Fe}_{30}\text{Ni}_{70})_{80}\text{Nb}_4\text{Si}_2\text{B}_{14}$ primary and secondary crystallization. Q for primary crystallization is 3.3 eV, and Q for secondary crystallization is 3.9 eV....	29
Figure 3.6: Activation energy for primary and secondary crystallization as a function of Ni fraction	30
Figure 3.7: TTT diagram for (a) primary and (b) secondary crystallization for $(\text{Fe}_{70}\text{Ni}_{30})_{80}\text{Nb}_4\text{Si}_2\text{B}_{14}$	33
Figure 3.8: TTT diagram for (a) primary and (b) secondary crystallization for $(\text{Fe}_{70}\text{Ni}_{30})_{79}\text{Nb}_4\text{Si}_2\text{B}_{14}\text{Cu}_1$	34
Figure 3.9: Magnetization vs. time for $(\text{Fe}_{30}\text{Ni}_{70})_{80}\text{Nb}_4\text{Si}_2\text{B}_{14}$ at temperature.....	35
Figure 3.10: The large-scale strain-annealer at CMU. The furnace can be seen in the center, and tension rollers are located on the sides.....	36
Figure 3.11: Percent elongation as a function of composition and applied stress	37
Figure 4.1: Sketch of a Paris-Edinburgh cell used at APS.....	41
Figure 4.2: Waterfall plots of synchrotron x-ray diffraction data for the bcc and fcc reflections for the α - and γ - phases of Fe respectively (a) NB1 2.2GPa, (b) NB1 5.0 GPa, (c) NB3 0.9 GPa, and (d) NB3 4.6 GPa.....	42
Figure 4.3: Fe nanostructure size scale as determined from Scherrer analysis of XRD data for the (002) reflection for the α - and γ -phases vs. temperature at 1.0 and 5 GPa, for sample composition (a) NB1 and (b) NB3. (c) and (d) are (002) peak area as a function of temperature	43
Figure 4.4: (a) P-T phase diagram and (b) heat capacity vs. temperature for pure iron	46
Figure 4.5: (a) γ -FeNi, (b) α -FeNi with random atomic assignment to lattice positions, and (c) Cr_{23}C_6	47
Figure 4.6: (a) and (b) $(\text{Fe}_{75}\text{Ni}_{25})_{80}\text{Nb}_4\text{Si}_2\text{B}_{14}$ at heated to 500 °C and 575 °C respectively. (c) and (d) $(\text{Fe}_{30}\text{Ni}_{70})_{80}\text{Nb}_4\text{Si}_2\text{B}_{14}$ heated to 450 °C and 525 °C respectively	48

Figure 4.7: XRD of annealed and strain-annealed alloys for (a) $(\text{Fe}_{30}\text{Ni}_{70})_{80}\text{Nb}_4\text{Si}_2\text{B}_{14}$, (b) $(\text{Fe}_{40}\text{Ni}_{60})_{80}\text{Nb}_4\text{Si}_2\text{B}_{14}$, (c) $(\text{Fe}_{45}\text{Ni}_{55})_{80}\text{Nb}_4\text{Si}_2\text{B}_{14}$, (d) $(\text{Fe}_{50}\text{Ni}_{50})_{80}\text{Nb}_4\text{Si}_2\text{B}_{14}$, (e) $(\text{Fe}_{60}\text{Ni}_{40})_{80}\text{Nb}_4\text{Si}_2\text{B}_{14}$, (f) $(\text{Fe}_{70}\text{Ni}_{30})_{80}\text{Nb}_4\text{Si}_2\text{B}_{14}$	49
Figure 4.8: XRD of (a) $\text{V}_{0.5}$, (b) V_5 , (c) $\text{Cr}_{0.5}$, (d) Cr_2 , (e) $\text{Nb}_{0.5}$, (f) Nb_2 , (g) $\text{Mo}_{0.5}$, and (h) Mo_5 alloys.....	50
Figure 4.9: (a) Bright field, (b) dark field, and (c) diffraction pattern for $(\text{Fe}_{70}\text{Ni}_{30})_{80}\text{Nb}_4\text{Si}_2\text{B}_{14}$ annealed at 420 °C	51
Figure 4.10: (a) Bright field, (b) dark field, and (c) diffraction pattern for $(\text{Fe}_{70}\text{Ni}_{30})_{80}\text{Nb}_4\text{Si}_2\text{B}_{14}$ annealed at 440 °C	52
Figure 4.11: (a) Bright field, (b) dark field, and (c) diffraction pattern for $(\text{Fe}_{70}\text{Ni}_{30})_{80}\text{Nb}_4\text{Si}_2\text{B}_{14}$ annealed at 480 °C	53
Figure 4.12: Crystallite size vs. temperature for $(\text{Fe}_{30}\text{Ni}_{70})_{80}\text{Nb}_4\text{Si}_2\text{B}_{14}$ at 5.6 GPa, $(\text{Fe}_{30}\text{Ni}_{70})_{80}\text{Nb}_4\text{Si}_2\text{B}_{14}$ at 1 atm, $(\text{Fe}_{65}\text{Ni}_{35})_{80}\text{Nb}_4\text{Si}_2\text{B}_{14}$ at 1 atm, and $(\text{Fe}_{72.5}\text{Ni}_{27.5})_{80}\text{Nb}_4\text{Si}_2\text{B}_{14}$ at 1 atm	56
Figure 4.13: EDXRD of $(\text{Fe}_{30}\text{Ni}_{70})_{80}\text{Nb}_4\text{Si}_2\text{B}_{14}$ before and after pressurization showing pressure induced crystallization	57
Figure 4.14: Schematic of atom probe tomography.....	58
Figure 4.15: Atom probe tomography 2D contour maps for Fe, Ni and B in (a) as-cast ribbon, (b) annealed ribbon, and (c) strain-annealed ribbon. All samples are 20 nm wide	60
Figure 5.1: M(T) for samples of nominal composition (a) $\text{Fe}_{87.4}\text{Nd}_{8.2}\text{B}_{4.4}$ (NB1) and (c) $\text{Fe}_{89.1}\text{Nd}_{5.9}\text{B}_{5.0}$ (NB3) showing transitions associated with the crystallization of an amorphous phase at 500 °C and a Curie transition at 770 °C in red and Brillouin function fits in blue. (b) and (d) are M vs. T cooling curves for NB1 and NB3 respectively. 2:14:1 phase T_c can be seen at 300 °C.....	65
Figure 5.2: The Bethe-Slater curve showing the relative positions of Mn, Fe, Co, and Ni.....	67
Figure 5.3: Sketch of demagnetized sample becoming magnetized via wall motion and domain rotation mechanisms.....	67
Figure 5.4: Saturation induction and Curie temperature for as-cast ribbon. Curie temperature for $\gamma\text{-FeNi}$ is in blue	70
Figure 5.5: Cooling and heating M vs. T curves for (a) as-cast and (b) annealed $(\text{Fe}_{70}\text{Ni}_{30})_{80}\text{Nb}_4\text{Si}_2\text{B}_{14}$	72
Figure 5.6: B vs. H loops for annealed and strain-annealed alloys.....	73
Figure 5.7: Circuit diagram depicting the 3-phase resistivity model	77
Figure 5.8: Schematic of 3d transition metal VBS in Fe matrix.....	78
Figure 5.9: Calculated DOS for fcc $\text{Fe}_{70}\text{Ni}_{30}$ with impurity d-electron LDOS	79
Figure 5.10: Resistivity of V, Cr, Nb, and Mo series	80
Figure 5.11: Permeability of annealed and strain-annealed V and Mo alloys	82
Figure 5.12: BH loops for the vanadium VBS series.....	83
Figure 5.13: BH loops for the molybdenum VBS series.....	84
Figure 5.14: Schematic FORC curve within a BH loop	84
Figure 5.15: Preisach distributions for (a) as-cast $(\text{Fe}_{70}\text{Ni}_{30})_{80}\text{Nb}_4\text{Si}_2\text{B}_{14}$ and (b) strain-annealed $(\text{Fe}_{70}\text{Ni}_{30})_{80}\text{Nb}_4\text{Si}_2\text{B}_{14}$	85
Figure 6.1: Losses for $(\text{Fe}_{70}\text{Ni}_{30})_{80}\text{Si}_2\text{Nb}_4\text{B}_{14}$ and Steinmetz fitting	88
Figure 6.2: Losses for $(\text{Fe}_{70}\text{Ni}_{30})_{79}\text{Si}_2\text{Nb}_4\text{B}_{14}\text{Cu}_1$ and Steinmetz fitting.....	90
Figure 6.3: Losses for $(\text{Fe}_{70}\text{Ni}_{30})_{79}\text{Si}_2\text{Nb}_4\text{B}_{14}\text{V}_1$ and Steinmetz fitting	90
Figure 6.4: (top) flux density for Si-steel, (bottom) flux density for $(\text{Fe}_{70}\text{Ni}_{30})_{80}\text{Nb}_4\text{Si}_2\text{B}_{14}$	91
Figure 6.5: Size comparison of Si-steel motors at 60 Hz and 400 Hz, and Fe-Ni MANC at 1 kHz	93

I. Introduction

i. Context within the Materials Science Paradigm

The materials science paradigm relates the synthesis, structure, properties, and performance of a material to each other, and each of these aspects is the focus of a chapter in this thesis. Synthesis of Fe-Ni metal amorphous nanocomposites (MANCs) is explored through the thermodynamics required to cast an amorphous alloy as described later in the introduction. To synthesize a MANC from an amorphous precursor, crystallization is required, and the crystallization kinetics are explored in Chapter 3. Chapter 4 explores the structure and phases of Fe-Ni MANCs through x-ray diffraction, transmission electron microscopy, and atom probe tomography. How pressure affects the structure and stable phases is also discussed. Chapter 5 is concerned with the relevant properties of Fe-Ni MANCs. Magnetization and Curie temperatures are determined, along with how strain-annealing affects the magnetic properties. Resistivity is also discussed in the context of alloying additions and virtual bound states. Lastly, chapter 6 is concerned with the performance of Fe-Ni MANCs. Toroidal cores were made and losses measured and Steinmetz parameters were determined. These parameters were then used in COMSOL modeling of a switched reluctance motor. Losses in the Fe-Ni MANC are then compared with losses in a Si-steel design at high frequency.

ii. Motivation

Electric motors are ubiquitous in our everyday lives from household tools, to industrial applications, to modern electric vehicles. It has been estimated that 19,000 TW-h of electricity was produced in 2006, with just under 50% going to motors as seen in Fig. 1.1¹. As such, even small improvements in efficiency can generate large energy savings. Electric motors use *soft and/or hard ferromagnets* to produce or direct spatio-temporally varying magnetic flux. Soft and hard magnets are differentiated by their coercivities as discussed below in chapter 1.2. New materials have the highest potential to reduce losses (~ 58%) between the *rotor and stator*. In motors, the rotor is the part that rotates in response to the

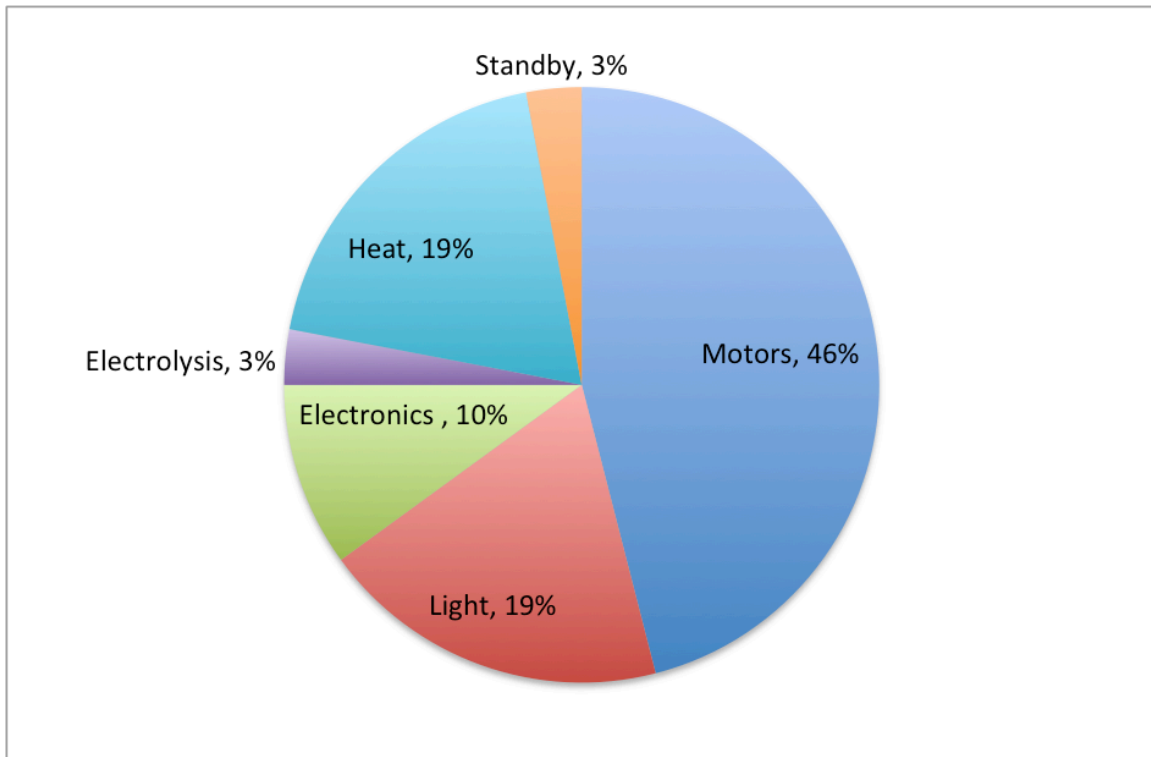


Figure 1.1: Global end-use of electricity. Adapted from Waide and Brunner¹.

excitation applied to the stationary stator. While permanent magnet (PM) motors

are popular due to rare-earth (RE) PMs, and advances in electronics; soft magnetic materials (SMMs) also provide significant opportunities for energy savings²⁻⁴. Supply constraints on RE elements (China controls $\sim > 80\%$)⁵, led to the classification of REs as very critical elements making novel approaches that reduce or eliminate RE PMs highly desirable^{6,7}. Figure 1.2 shows the price of Neodymium oxide from 2009-2015⁸.

Metal Amorphous Nanocomposite (MANC) SMMs offer a transformational

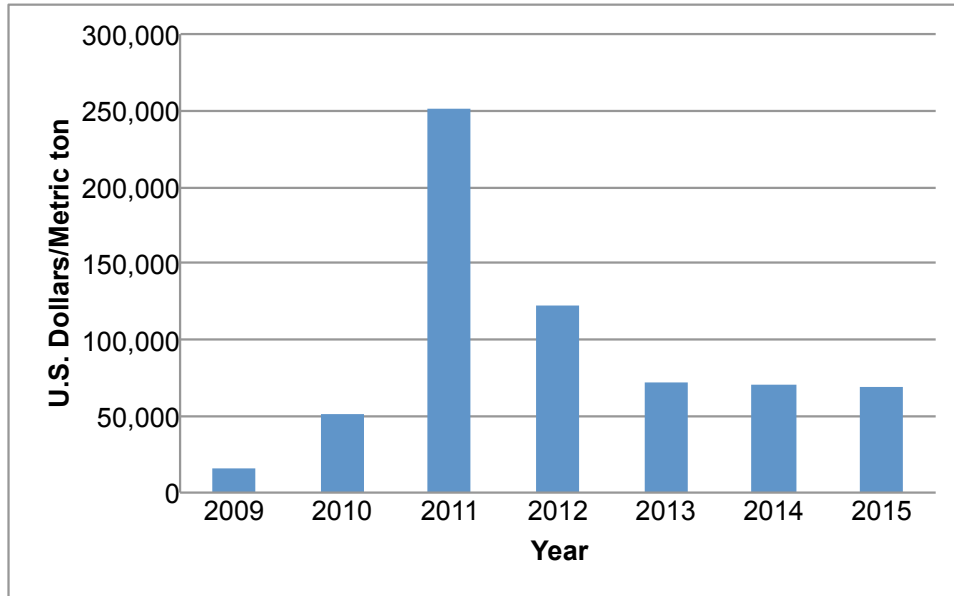


Figure 1.2: Price of Neodymium oxide from 2009-2015⁸.

technology to increase efficiency and limit RE use for high power, high torque density motors. Hybrid motor designs employ a REPM as the rotor and cheaper, non-critical high induction soft magnetic material as the stator. Laminated silicon steels have been traditionally used as a SMM in stators but newer materials can reduce motor size^{3,4}. **Amorphous** SMM's have been more recently investigated in a variety of motor designs⁹⁻¹². Amorphous materials are defined as lacking crystalline periodicity. The most recently developed advanced MANC SMMs¹³ can have usable

peak inductions comparable to Si-steels with resistivities¹⁴ that allow high switching frequencies required for high torques in motor applications. High inductions and high frequency switching allows motor size reduction minimizing volume and weight that can enable new high efficiency motor topologies. This is leveraged on property improvements in MANCs targeting 1-10 kHz frequencies in geometries amenable to stators in high-speed motors^{3,4}. While new MANC motors recently described in work by Silveyra^{3,4} consider Co-based MANCs due to the high temperature stability and attractive mechanical properties, lower cost substituents^{15,16} and replacement of Co by Fe- or Ni-based materials may favorably impact the economics of such motors. A cost comparison of various elements frequently used in MANCs is summarized in Table I.I. It is notable that B is significantly more expensive than any of the other elements. Ferroboron use as a B source can reduce costs and very recently, work is being done to replace B with significantly cheaper B₄C¹⁶. Using values in the table below, an (Fe₇₀Ni₃₀)₈₀Nb₄Si₂B₁₄ alloy would cost \$21.77/lb. On the other hand, a Co-rich alloy, such as Co_{77.2}Fe_{1.4}Mn_{1.4}Si₂B₁₄Nb₄ would cost over twice as much at \$56.06/lb.

Table I.I: Cost comparison of various elements frequently used in MANCs^{15,17-19}.

	M (gr/mol)	Price (\$/lb)
Fe	55.85	0.176
Co	58.93	40.26
Ni	58.69	6.2
Mn	54.94	0.93
Cu	63.55	3.08
Si	28.09	2.1
B	10.81	600

Nb	92.91	34
----	-------	----

iii. Fundamentals of Soft Magnetic Materials

Materials exhibiting *ferromagnetism* are those for which the electron spin dipole moments are ordered in the absence of magnetic field over a volume called a *magnetic domain* below a temperature called the *Curie temperature, T_c* . In an applied field of sufficient strength, a magnetically saturated material has a single magnetic domain encompassing the entire sample volume. In zero field it is energetically favorable to have multiple domains to minimize *demagnetization fields*, which are fields emanating from free north poles to free south poles. When an external field is applied, there are two ways by which the domains can align with the direction of the field: (1) domain growth or (2) domain rotation. In domain growth, domains that are already aligned in the field direction expand at the expense of their neighbors by domain wall movement. Domain rotation is when instead of wall motion, individual atomic moments, coupled by *magnetic exchange interactions*, within the domains rotate to align in an applied field.

Magnetic materials are broadly split into two group, *soft magnets* and *hard/permanent magnets*. The two groups are differentiated by their *coercivities* (H_C), with soft magnets having much lower values and permanent magnets difficult to demagnetize. Coercivity is defined as the field required to take a saturated sample back to zero magnetization. Other important magnetic parameters are *saturation magnetization* (M_S), *permeability* (μ), and *remnant magnetization* (M_R). Saturation magnetization is the magnitude of the magnetization of a single

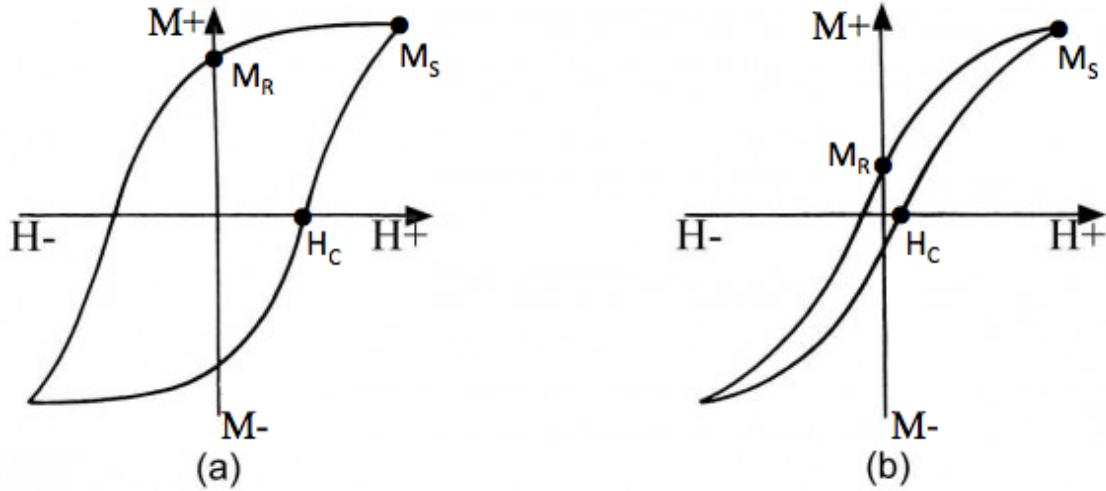


Figure 1.3: (a) a model hysteresis loop for a permanent magnet, and (b) a model hysteresis loop for a soft magnet.

magnetic domain, and permeability relates the strength of the external field to the magnitude of the induced internal field. Remnant magnetization is the value of the magnetization of a sample once the field is removed after the sample was saturated. Hysteresis loops showing the difference between hard and soft magnets, and magnetic properties are shown in Fig. 1.3. Developing the correct balance of these properties for various applications drives much of the current research in magnetic materials.

iv. Historical development

Michael Faraday first demonstrated the **law of induction** using an Fe core. As the electricity industry developed and accepted AC currents, Fe cores proved to be too lossy due to their low resistivity, which led to high **classical eddy current losses**. Classical eddy current losses are described by eq. 1.3.1:

$$P_e = bf^2B^2 \quad (1.4.1)$$

with the coefficient b given by eq. 1.3.2

$$b = \frac{(\pi \cdot t)^2}{\rho} \quad (1.4.2)$$

where t is the thickness and ρ is the resistivity. For this reason, silicon steels have been studied since the 1880's²⁰ and had market dominance by the 1930's²¹. Silicon steels are still the industry standard for high voltage AC power transformers. For more specialized applications, higher inductions are required which led to the development of Fe-Co alloys that have found use in military and commercial aerospace applications and where cost is less of a concern. Commercial FeCo alloys include Permendur, Supermendur and Hiperco. Fe-Co alloys have the highest

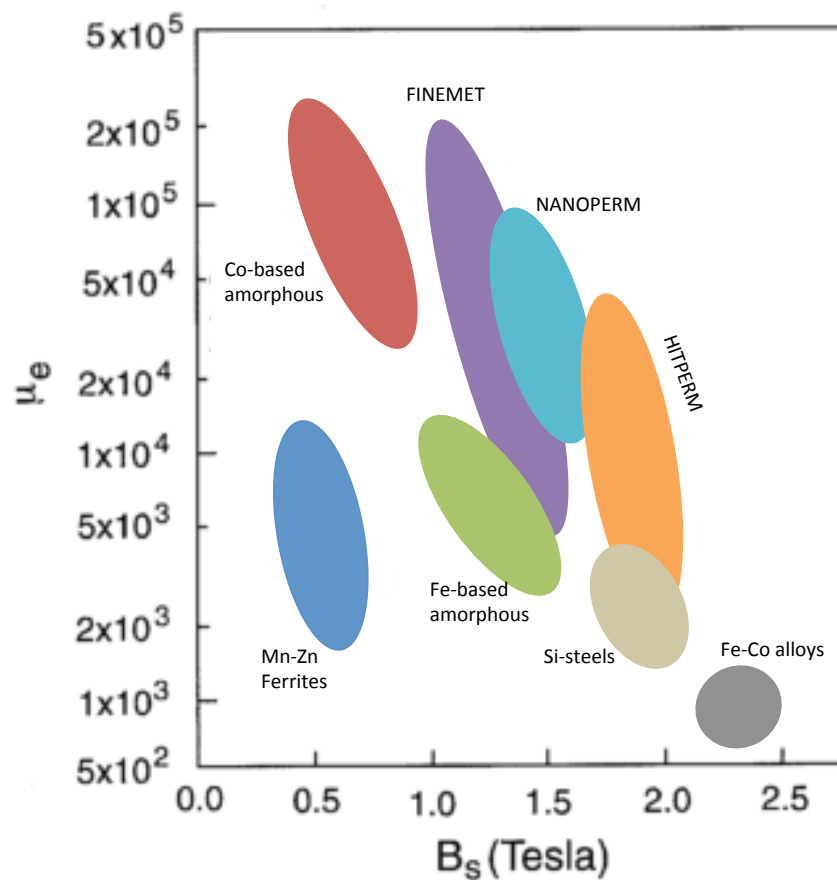


Figure 1.4: Permeability and saturation induction for a variety of soft magnetic materials. Adapted from McHenry et al¹³.

inductions of transition metal alloys. This can be understood in relation to the **Slater-Pauling curve**²², which is discussed in more depth in chapter 3.2. Other applications, such as sensors and motors, require higher permeabilities than that of Si-steel. For these applications Fe-Ni alloys, permalloys^{23,24}, were developed. A figure of merit plot for SMMs as a function of permeability and induction can be seen in Fig. 1.4.

More recently, amorphous materials were developed, and the succession paralleled that for the crystalline alloys described above, i.e. Fe- and Fe-Si- based, Co- based, then Ni- based amorphous alloys were developed. An amorphous structure lacks crystalline periodicity, and so atoms do not have set distances and angles between each other beyond one or a few nearest neighbor shells. The benefit of an amorphous structure is in increasing the resistivity, which is a direct result of the absence of crystalline periodicity, which has the consequence of lowering the classical eddy current losses. Creating magnetic amorphous metals was accomplished by adding B, P, or Si to the magnetic elements to act as glass formers. With these simple amorphous alloys, it was observed that the magnetic properties would deteriorate upon crystallization due to the large size of the crystallites²⁵. More recently, attention has shifted to nanocomposite materials. Metal/ amorphous nanocomposites (MANCs) have nanocrystallites, nucleated and grown in a **primary crystallization process**, embedded in an amorphous matrix, with crystals typically between 1-50 nm in diameter^{13,26,27}.

Nanocomposite, Fe-Si systems were the first commercialized, by Hitachi Metals, under the trade name FINEMET²⁸. Fe-based nanocomposites called

NANOPERM²⁹, which suffer from low T_c 's, but have high permeabilities and low magnetostrictive coefficients were subsequently developed. Fe-Co nanocomposites (HITPERM³⁰) were then studied, and followed more recently by Co-based nanocomposites³⁰. While low T_c FeNi -based nanocomposites have been investigated for magnetocaloric applications³¹⁻³⁴, relatively little work has been done to date on high induction Fe-Ni nanocomposites, which is the focus of this thesis. Fe-Ni nanocomposites allow for a wide range of compositions where we can avoid α -Fe nanocrystals in favor of metastable γ -FeNi, even at Fe-rich compositions, which have attractive properties described below.

Several well-known and important Fe-Ni crystalline alloys have attractive properties for applications²³. The 50-50 alloy has the highest saturation magnetization. On the more Ni-rich side, 78% Ni Permalloys are important due to their zero-magnetostriction coefficient and high permeability. Since not all properties can be optimized at once, the composition must be chosen with particular device applications in view. Fe-rich Fe-Ni alloys have been studied recently for use in magnetocaloric cooling applications due to near room temperature T_c 's^{31,32}. Certain Fe-rich Fe-Ni alloys have inductions and Curie temperatures that are attractive for power applications. A peak in the composition dependence of the magnetic induction for metastable fcc FeNi magnets can only be exploited in alloys processed to maintain this metastable state.

v. The Bulk Fe-Ni Alloy System

In bulk, γ -Fe is only stable at very low temperatures, but adding Ni stabilizes the γ phase over the majority of the composition spectrum³⁵ as seen in the phase diagram in Fig. 1.5. While the ordered FeNi_3 alloy is stable at lower temperatures as opposed to γ -FeNi, it is kinetically difficult to attain³⁶, allowing for easy retention of

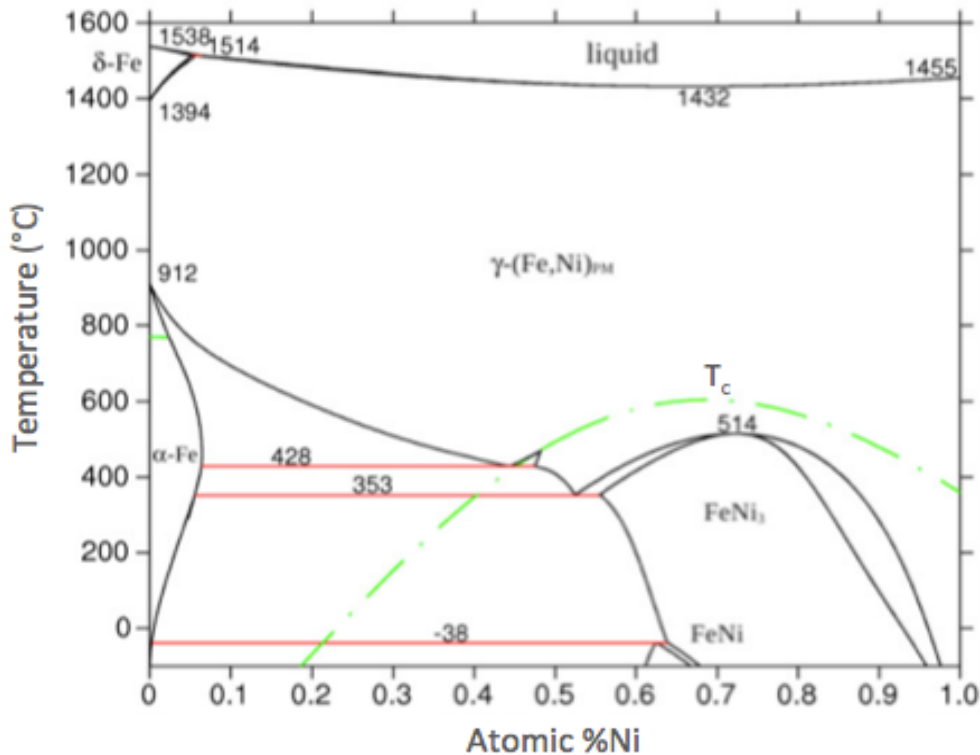


Figure 1.5: Binary phase diagram for Fe-Ni, adapted from³⁵.

the disordered phase at low temperatures. On the Fe-rich side of the phase diagram, again the kinetics are very slow, requiring cooling on the order of a few degrees a day in order to accurately determine the phase boundaries. For Fe-rich alloys, the fcc γ -phase is stable at high temperatures and metastable at low (including room) temperature. An important alloy at the Fe-rich end is Invar³⁷, which has almost zero thermal expansion for a range of temperatures around room temperature. In FeNi-

based MANCS it is notable that a metastable nanocrystalline fcc γ -phase can be observed in MANCs over a range of Fe:Ni stoichiometries³⁴. In addition, L1₀ Fe-Ni alloys with interesting magnetic properties have been observed in meteorites³⁸⁻⁴¹.

From the perspective of soft magnetic materials, Ni-rich Fe-Ni alloys are very important. This is due to the fact that the magnetostriction and magnetocrystalline anisotropy have a zero crossing near 80% Ni, which allow these alloys to attain coercivities of about 0.5 A/m and initial permeabilities near 200,000⁴². Mu-metal is such a Ni-rich alloy with very high permeabilities and is used in magnetic shielding applications.

vi. Losses

AC losses in a magnetic material can be separated into those arising from (1) magnetic hysteresis, (2) conventional eddy currents and (3) anomalous eddy currents. Each of these losses have a different frequency dependence. Hysteresis losses relate to the area inside the hysteresis loop of a material that is the energy/volume lost over one magnetic cycle as illustrated above. Since it is a constant amount per cycle, the total power lost is linear with time. Hysteresis losses can be decreased if the coercivity of the materials is lowered. This is one reason why using a nanocomposite material is beneficial. Reducing crystallite size below a certain amount significantly lowers H_c , thereby lowering DC hysteretic losses as described in the *random anisotropy model*^{21,43,44}. The mechanism for this is due to the small structural correlation lengths, or grains, associated with a nanocomposite material. The exchange length is the length over which the direction of magnetization cannot significantly vary^{43,45}. Exchange length, L_0 , is proportional to

$(A/K_1)^{1/2}$ where A is the exchange stiffness and K_1 is the magnetic anisotropy. For a hard magnetic material a typical exchange length is ~ 1 nm, whereas for soft magnets it is an order of magnitude greater, such as ~ 20 nm for Fe. In amorphous and nanocomposite systems, the anisotropy energy is averaged over a number of grains, N, within a magnetically coupled volume as expressed by:

$$N = \frac{V_{ex}}{V} = \left(\frac{L_{ex}}{D} \right)^3 \quad (1.6.1)$$

where V is the volume of a grain, V_{ex} is the exchange volume, and L_{ex} is the length of the exchange coupled volume. The average magnetocrystalline anisotropy can then be written as:

$$\langle K_1 \rangle = \frac{K_1}{\sqrt{N}} \quad (1.6.2)$$

From the preceding equations, L_{ex} can be expressed as:

$$L_{ex} = \sqrt{\frac{A}{\langle K_1 \rangle}} = L_0 \left(\frac{L_0}{D} \right)^3 \quad (1.6.3)$$

which leads to:

$$\langle K_1 \rangle = K_1 \left(\frac{D}{L_0} \right)^6 \quad (1.6.4)$$

Since H_c is proportional to the anisotropy, at small grain sizes, H_c also decreases as D^6 . In short, because the correlation lengths are small, exchange interactions force the magnetic moments to align parallel, regardless if they are in a magnetocrystalline easy direction. As such, over several correlation lengths, the magnetic anisotropy, from which the coercivity is rooted, is reduced⁴³. It should be

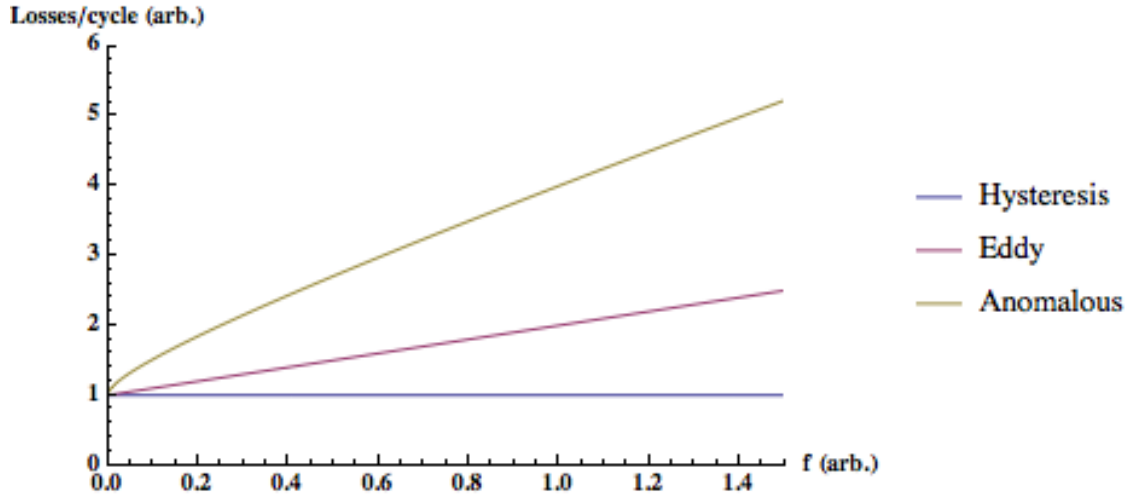


Figure 1.6: Comparison of the three sources of losses per magnetic cycle. Adapted from [17].

noted that in systems with coherent uniaxial induced anisotropies, H_C follows a D^3 law due to the prevalence of the uniaxial anisotropy over the random magnetocrystalline anisotropy⁴⁶.

Classical eddy current losses relate to the fact that an AC current produces an alternating magnetic field, which induces eddy currents in the material. These currents give rise to I^2R power losses that heat the material. Eddy current losses are mathematically expressed above in eq. 1.4.1.

It follows from eq. 1.4.2 that to minimize classical eddy currents, we want thin cross sections and high resistivity². Thin cross sections are obtained through melt-spinning the alloy. The relevant variables are wheel speed, casting temperature, ejection pressure, and nozzle-wheel gap distance. Casting ribbons thinner than about $13 \mu\text{m}$ is difficult due to the formation of pinholes, which impact how the ribbons are wound into a magnetic core⁴⁷. Standard silicon-steels used in motors have lamination thickness near 0.6 mm. By using a ribbon that is $25 \mu\text{m}$ thick, eddy losses would be reduced by two orders of magnitude, all-else being

equal. Hysteresis loss and eddy current loss are often expressed in terms of the **Steinmetz equation**⁴⁸:

$$P = kf^\alpha B_m^\beta \quad (1.6.1)$$

with P as power loss, and k, α , and β are empirical fits to data.

To model the resistivity of a nanocomposite, it is fruitful to consider three phases: the crystalline, amorphous, and a shell phase comprised primarily of glass formers and growth inhibitor atoms¹⁴. Of the three, the crystalline phase has the lowest resistivity, and because the shell has the highest concentration of glass formers, it has the highest resistivity. Without the shell, we would assume the path of least resistance would be to maximize the distance travelled in crystallite in relation to amorphous matrix. However, the high resistivity shell complicates this. From previous modeling¹⁴, we know to maximize resistivity we want small crystalline grain sizes, high glass former concentration in the shell, and a thick shell around the crystals.

The third source of loss is **anomalous eddy currents**. Anomalous losses are due to eddy currents that accompany domain wall movement when the magnetization of the material is switched. Anomalous losses can be expressed as:

$$P_a \propto f^\gamma B^\gamma \quad (1.6.2)$$

where γ is greater than one and depends on the domain width and lamination thickness²¹. This can be reduced if a magnetic anisotropy is induced such that the magnetic domains are aligned transverse to the ribbon direction in the absence of a magnetic field⁴⁹. The relative importance of each source of loss as a function of frequency can be seen in Fig. 1.6.

vii. MANC Synthesis

In order to produce a MANC, an amorphous precursor must first be cast. This is accomplished by first synthesizing a compositionally homogeneous ingot by arc melting. The ingot is then remelted and cast using a rapid solidification process (RSP) to produce an amorphous ribbon. The rapid solidification process used in this

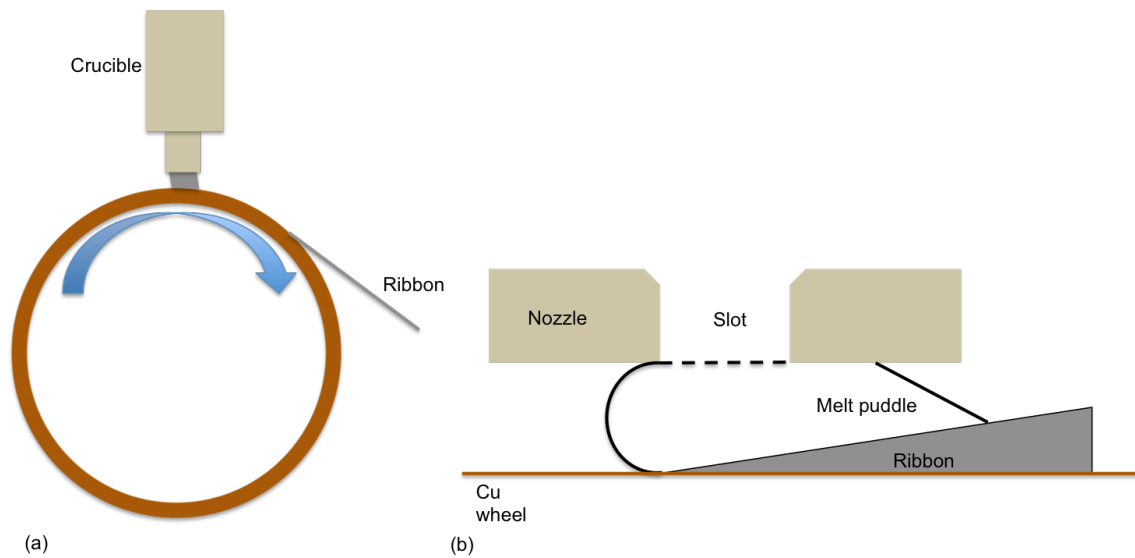
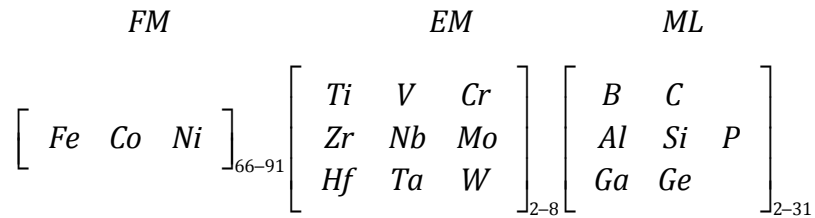


Figure 1.7: (a) Schematic of planar flow casting an amorphous alloy. (b) Detail of nozzle, melt puddle and solid ribbon.

work is **planar flow casting** (PFC). In PFC, the ingot is placed into a BN crucible within a vacuum chamber that is then heated with an RF induction coil. The BN crucible is placed close to the chilled wheel. Pressurized argon is then used to eject the melt out of a slotted nozzle orifice at the bottom of the crucible. The melt is ejected to form a stable melt pool resident, for ~ 1 ms, on a water chilled copper wheel. This cools the melt at a rate of 10^6 K/s that is fast enough to prevent the atoms from finding their equilibrium positions on a crystalline lattice, resulting in an amorphous ribbon. The resulting ribbons are typically ~ 20 μm in thickness and

1-2 mm wide. Fig. 1.7 (a) shows an overview of the process, and (b) shows the detail of the liquid melt and ribbon around the nozzle⁵⁰.

In order to determine whether a given alloy will be castable into an amorphous ribbon, it is helpful to consult the following matrix proposed by Suzuki⁵¹ and extended by Willard⁵². FM are the ferromagnetic elements, EM are early



transition metals, and ML are metalloids. EMs act as growth inhibitors, suppressing crystallite size. MLs work as glass formers, helping to ensure the alloy solidifies with an amorphous structure.

Glass formability can be thermodynamically described in terms of T_0 lines as seen in Fig. 1.7. The ***glass-forming ability (GFA)*** of a material explains the suppression of nucleation and growth of the stable crystalline phase⁵³. This involves preventing the elements in the liquid from partitioning into the crystalline phase/s. A material's GFA is related to its reduced glass-forming temperature (T_{rg}), which is expressed by:

$$T_{rg} = \frac{T_g}{T_L} \tag{1.7.1}$$

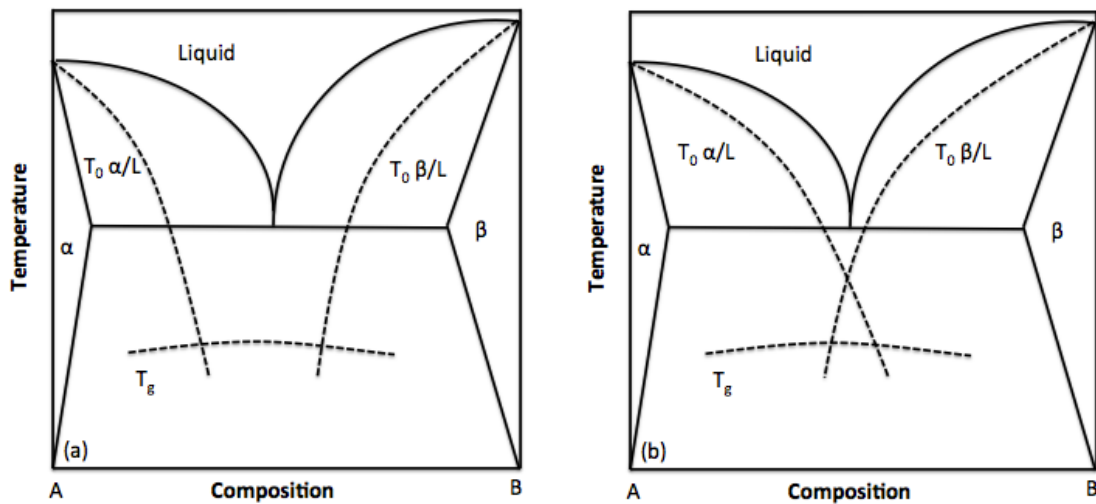


Figure 1.8: Illustration of T_0 diagram construction for a binary alloy^{57,58}.

where T_g is the glass transition temperature and T_L is the liquidus temperature. Below T_g , the structure is frozen, but above T_g , the material is capable of viscous flow⁵⁴⁻⁵⁶. For ease of glass formation, T_g should be maximized and T_L should be minimized. Glass formation thermodynamics is illustrated in the T_0 diagram in Fig. 1.8. The T_0 curve describes all points where the liquid and solid phase free energies are equal^{57,58} (such as the points of intersection seen in Fig. 1.9). For compositions between the T_0 curves, the liquid can lower its free energy only by diffusion into the α and β phase. Outside the T_0 curves, the liquid can form solid crystals without diffusion. Within the T_0 curves, if we quench the melt below the T_g rapidly enough, diffusion cannot occur and a liquid atomic structure is frozen in. In addition to T_0 lines and chemical composition, there are other important considerations for glass formability. These include the rate of heat flow out of the melt, the velocity of the interface between the ribbon and liquid, and the ratio of the latent heat to the specific heat of the liquid phase¹³.

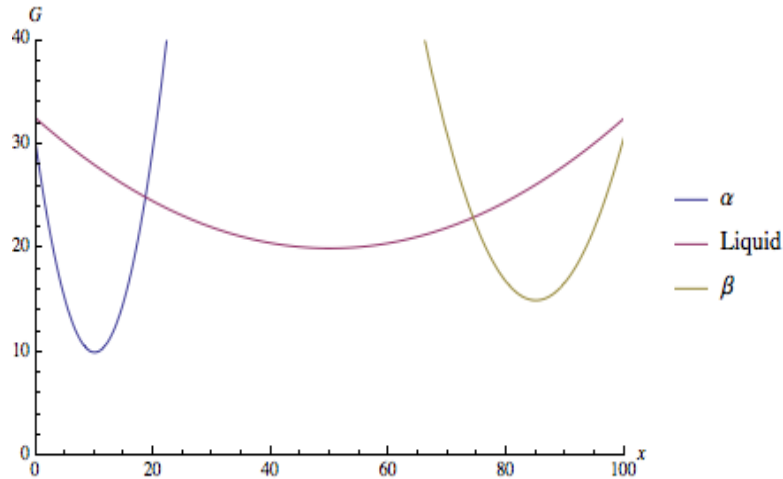


Figure 1.9: Sketch of Gibb's free energy curves for a liquid and two solid phases. Where the liquid intersects the solid lines are T_0 points.

Fabricating MANCs at an industrial scale is accomplished through a derivative of melt spinning called planar flow casting. In planar flow casting, the BN crucible orifice is a slit, and the crucible is placed close to the wheel. This ensures that the produced ribbon will be the same width as the slit orifice. Planar flow casting allows for better control of the melt pool and its residence time on the rotating Cu wheel heat sink and therefore aids glass formability.

II. Hypotheses

The goal of this thesis work is to develop Fe-Ni MANCs and to understand phase relations and the kinetic constraints on nanostructures which influence the properties of resulting MANCs for use in electric motors. In this pursuit, we will demonstrate:

1. An Fe-Ni based alloy can be developed with saturation induction and coercivity attractive for use in motor applications
2. We will be able to tune the anisotropy by strain-annealing, a method of applying stress to the ribbon while it is annealed, to achieve longitudinal anisotropy
3. Resistivity can be tuned with the addition of early transition elements that provide resonant scattering through **Friedel virtual bound states**⁵⁹ (defined below in section 5.13)
4. Pressure can be used to change diffusional energy barriers to refine the microstructure
5. Crystallization kinetic studies will explain the stability of the nanocomposite within a temperature range of interest as well as predicting the volume fraction of nanocrystals as a function of time and temperature following nanocrystallization

Each of these topics is developed more fully in the subsequent chapters of this document, along with examples of preliminary and published work toward this end.

III. Crystallization Kinetics

i. JMAK Kinetics

Crystallization is a ***solid-state phase transformation*** typically controlled by nucleation and growth. The extent of a phase transformation can be visualized by plotting the volume fraction transformed vs. temperature and time in what is called a ***TTT diagram***. The kinetics required to construct a TTT diagram can be derived from Johnson-Mehl-Avrami-Kolmogorov⁶⁰⁻⁶² (JMAK) kinetics. With JMAK kinetics, the rate constant, k , is expressed as:

$$k = k_0 \exp\left(\frac{-Q}{k_B T}\right) \quad (3.1.1)$$

where Q is the ***activation energy*** for crystallization. The rate constant in JMAK has several assumptions, namely:

1. Nucleation and growth are isothermal
2. Nucleation is homogenous
3. Growth is isotropic
4. Q is independent of time and temperature

The JMAK equation for volume fraction transformed can then be written:

$$X = 1 - \exp(-(k(t - t_i))^n) \quad (3.1.2)$$

where t_i is the incubation time, and n is between 1 and 4 depending on dimensionality and the nucleation and growth mechanism. Unfortunately, the above assumptions are not necessarily true for MANCs, leading to further complexity to the kinetics analysis⁶³⁻⁶⁶.

In real MANC systems, the growing crystals do not impinge one another, but there is a “soft impingement” that results from the superposition of diffusional composition profiles of species in the intervening amorphous phase. This overlap affects the overall growth kinetics. When a crystal first forms, the growth is interface controlled due to the crystal’s small surface area. Once the crystal is bigger than the critical nucleus size (r_c), the growth rate will be diffusion controlled. As a crystal grows, the region around it becomes depleted in the primary crystalline elements, and enriched in glass formers and growth inhibitors. The concentration of glass formers is denoted c^* . A new crystal cannot form if it is within the critical radial distance of an existing crystallite since it would never grow larger than the critical radius. In classical JMAK kinetics, crystals are assumed to grow until they

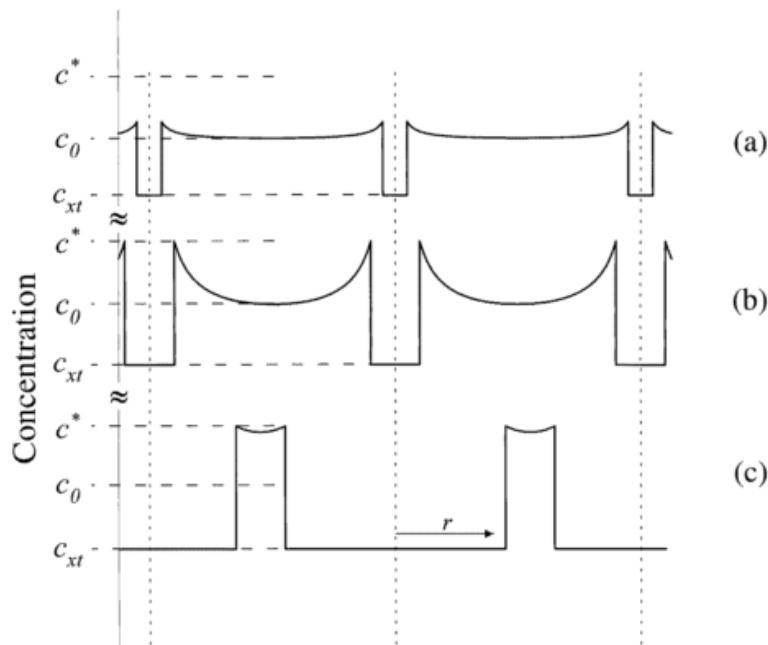


Figure 3.1: Schematic of primary crystallization and soft impingement. (a) Start of crystallization with small crystals and large glass former concentration gradient. (b) Intermediate stage, and (c) soft impingement. Adapted from Pradell et. al⁶⁷.

strike upon another crystal. However, before crystals contact one another, their respective diffusion profiles begin to overlap leading to the soft impingement

introduced above. This causes a reduction in growth rate due to a reduction in concentration gradient⁶⁷. A schematic of soft impingement is shown in Fig. 3.1, where c_0 is the glass former concentration far from the crystal interface, and c_{xt} is the concentration of glass formers in the crystals, which is assumed to be small due to low solubility. Due to the nature of soft impingement, crystals will not form a percolated network.

ii. Rigid Band Theory, Cohesive Energy, and the Slater-Pauling Curve

While magnetism and magnetic properties will be fully discussed in chapter 5 of this work, it is worth examining the principles of rigid band theory, cohesive

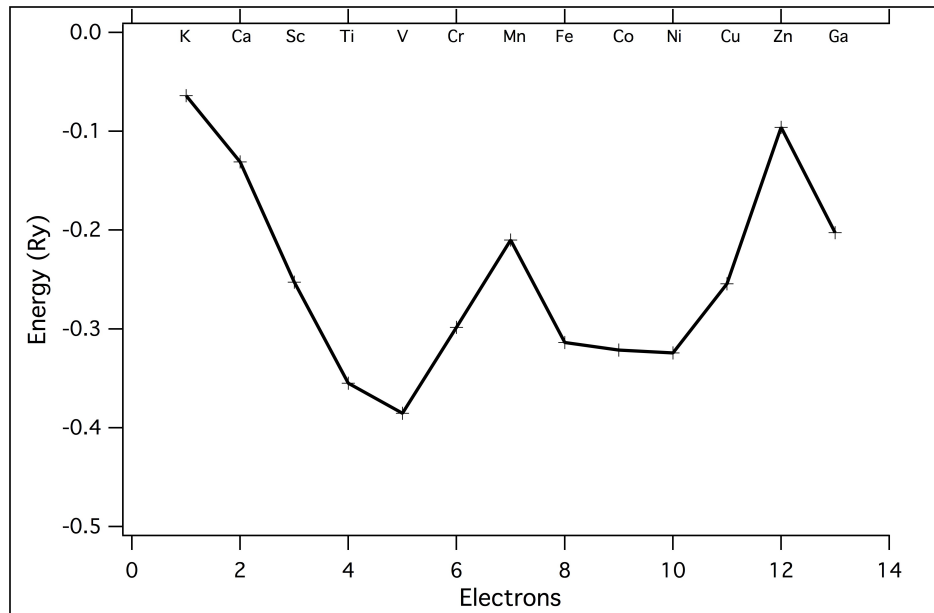


Figure 3.2: Cohesive energies for period 4 metals.

energies, and the Slater-Pauling curve here due to their relevance for crystallization. The Friedel model of the density of states (DOS) utilizes a narrow parabolic DOS for s-orbital states, and broad rectangular DOS for d-orbital states. By integrating the DOS, a cohesive energy can be calculated^{59,68}. When the cohesive energy is plotted

as a function of element across a period in the periodic table, a roughly parabolic curve is obtained with a parabolic hump, with opposite curvature, centered at Mn⁶⁹,

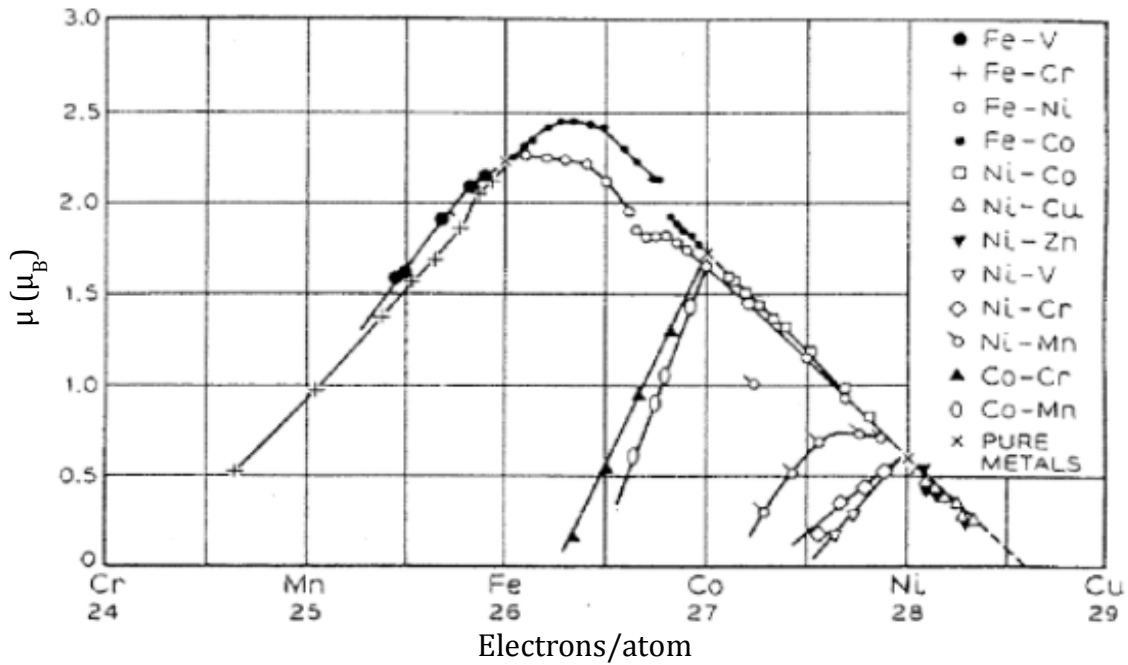


Figure 3.3: The Slater-Pauling curve. Adapted from Bozorth (1951)¹⁰⁹.

which arises from magnetic exchange interactions. The cohesive energy can be seen in Fig. 3.2. In transition series (4d- and 5d-) that do not have elements with stable ferromagnetic ground states, the deviation from a simple parabolic Energy vs. electron count is not observed.

For alloys, it is helpful to employ a rigid band model, which assumes the d-band is not significantly affected by alloying, but rather the band simply empties or fills depending on the composition. Simplified models, such as the rigid band model, provide a useful framework for thinking about band structures and determining first order approximate solutions. For more detailed studies, first order calculations are necessary. Within the rigid band model, around a given solute atom in an alloy, a reduction in magnetic moment occurs that depends on the difference in valence

between the solute atom and the matrix. The average magnetic moment is then the composition weighted average of local moments²⁶. This calculation provides the basis for the Slater-Pauling curve^{70,71} which predicts composition dependent alloy magnetizations that can be used in the exercise of alloy engineering for specific applications. The Slater-Pauling curve can be seen in Fig. 3.3.

iii. Trends in Primary and Secondary Crystallization Temperatures

The general procedure for MANC synthesis has been outlined above in section 1.7. When developing new MANC alloys, it is critical to understand the crystallization kinetics of both primary and secondary crystallization. The kinetics of primary crystallization should be understood, because it yields the useful metastable state exploited in applications. Secondary crystallization kinetics should

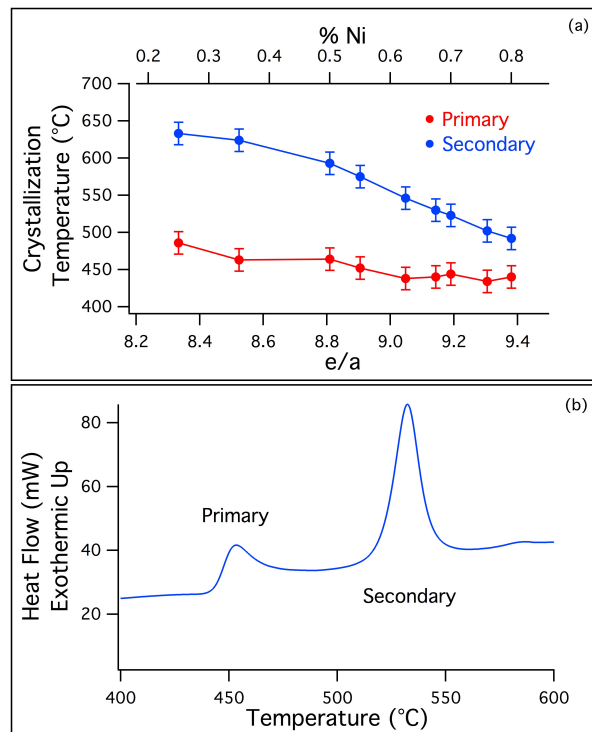


Figure 3.4: (a) Crystallization temperature vs. electrons/atom. (b) Typical DSC curve showing exothermic peaks for primary and secondary crystallization with a heating rate of 40 °C/min.

be understood because it reflects the transformation to be avoided because it destroys the desired MANC nanostructural features, namely the crystallization of the residual amorphous phase.

Primary and secondary crystallization temperatures for alloys across the Fe-Ni spectrum are illustrated in Fig. 3.4 (a) as a function of the average number of s and d electrons per metal atom in the alloy. Primary crystallization is defined as the event during which only Fe and Ni crystallize. Secondary crystallization is defined as when the remaining glass former enriched amorphous phase crystallizes. Electrons per atom is determined by calculating the number of electrons per transition metal atom as a function of alloy composition⁷². Fig. 3.4 (b) shows a typical DSC curve with clear primary and secondary exothermic crystallization events. The glass formers are identical in all compositions, with only the relative amounts of Fe and Ni changing. Because Fe and Ni have nearly identical atomic diameters, the systematic variation in the crystallization temperatures is strongly correlated with electron concentration⁷³ and the bonding characteristics of the alloy. It has been previously proposed that the bonds produced by the overlap between the s-p orbitals of the metalloids and the s-d orbitals of the transition metals are strengthened by a lower number of d-electrons, or a lower e/a value, thereby stabilizing the amorphous phase. A lower e/a value corresponds to increasing the number of bonding states, while a higher e/a value increases the number of antibonding states⁷².

This stabilization of the amorphous phase at higher Fe contents can also be viewed from the perspective of the Freidel model⁵⁹ of the density of states. As

discussed earlier, with the Friedel model, a roughly parabolic cohesive energy, E_c , can be calculated as a function of electron/atom ratio across a period^{59,68}. Crystalline Fe is less cohesive than Ni, so we would expect the amorphous phase to be more stable with respect to secondary crystallization as the alloy is enriched in Fe. This is because with higher Fe content, the energy is lowered by a smaller amount with crystallization as compared to a Ni-rich alloy.

iv. Kinetics from Thermal Analysis and the Kissinger Equation

DSC not only be used to obtain crystallization temperatures, but can also obtain the activation energies⁷⁴, Q , associated with crystallization events as well. Kissinger first reported the calculation of Q from DSC data⁷⁵. Kissinger derived his equation by starting with the reaction rate equation:

$$\frac{dx}{dt} = k_0(1-x)^n e^{\frac{-Q}{RT_p}} \quad (3.4.1)$$

where dx/dt is the reaction rate, k_0 is the rate constant, n is the order of reaction, and T_p is the peak reaction rate temperature. The maximum reaction rate occurs when dx^2/d^2t equals zero. This yields:

$$0 = \frac{Q\phi}{RT_p^2} - k_0 n(1-x)^{n-1} e^{\frac{-Q}{RT_p}} \quad (3.4.2)$$

where ϕ is the heating rate. The product $n(1-x)^{n-1}$ may be taken as equal to one, and then the derivative of eq. 3.3.2 yields:

$$\frac{d\left(\ln\frac{\phi}{T_p^2}\right)}{d\left(\frac{1}{T_p}\right)} = \frac{-Q}{R} \quad (3.4.3)$$

This can be easily rearranged to the well-known Kissinger equation:

$$\ln\left(\frac{\phi}{T_p^2}\right) = -\frac{Q_K}{RT_p} \quad (3.4.4)$$

The subscript on Q refers to the fact that this activation energy is derived from the Kissinger equation. Practically, to obtain Q from DSC, all that is needed is DSC data using multiple heating rates.

After Kissinger, there were several other methods either extending Kissinger analysis, or starting from different assumptions. Here it is of interest to examine the Augis and Bennett method⁷⁶, which is an extension of the Kissinger method, but allows for the calculation of the Avrami exponent as well.

For the Augis and Bennett method, we will take the temperature to be:

$$T = T_0 + \phi t \quad (3.4.5)$$

where T_0 is the initial temperature, and the volume fraction transformed will be the same as for JMAK seen above in eq. 3.1.2. Next, the rate constant times time is written:

$$kt = k_0 t \cdot \exp\left[-\frac{\Delta Q}{R(T_0 + \phi t)}\right] \quad (3.4.6)$$

from which it can be derived that:

$$(kt)^n \exp\left[n \frac{\Delta Q}{RT_m}\right] = \left(\frac{T_m - T_0}{\phi}\right)^{-n} \left[1 - \frac{1}{n \left(1 + \frac{\Delta Q(T_m - T_0)}{RT_m^2}\right)^2} \right] \quad (3.4.7)$$

with T_m being the temperature at the peak maximum. The value $\Delta Q T / RT^2 \gg 1$, so the term in the brackets can be ignored. With further simplification, it can be shown that the activation energy is the slope of the plot:

$$\ln\left(\frac{\phi}{T_m - T_0}\right) \text{ vs. } \frac{1}{T_m} \quad (3.4.8)$$

The authors admit however that for a common range of activation energies, the results from their method and the Kissinger method are nearly identical.

In order to obtain the Avrami exponent, we will first replace kt in eq. 3.3.6 with u , and then take the time derivative of the volume fraction transformed. This yields:

$$\frac{\partial X}{\partial t} = \frac{\partial u}{\partial t} n u^{n-1} (1-X) \quad (3.4.9)$$

With a Taylor series expansion around values of $T=T_m$, the thermal analysis peak can be described by:

$$\frac{\partial X}{\partial t} = n \frac{\Delta Q}{RT^2} \exp\left(n\tau \frac{\Delta Q}{RT^2}\right) \exp\left[-\exp\left(n\tau \frac{\Delta Q}{RT^2}\right)\right] \quad (3.4.10)$$

where τ is the difference between T and T_m . If $\Delta\tau_{FWHM}$ is the full width at half maximum of the peak, then the Avrami exponent can be estimated by:

$$n = \frac{2.5}{\Delta\tau_{FWHM}} \frac{T_m^2}{\frac{Q}{R}} \quad (3.4.11)$$

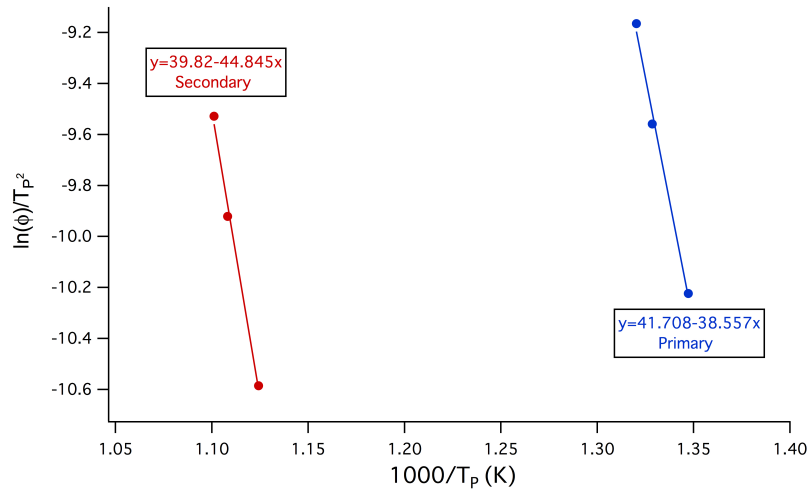


Figure 3.5: Kissinger plots for $(\text{Fe}_{30}\text{Ni}_{70})_{80}\text{Nb}_4\text{Si}_2\text{B}_{14}$ primary and secondary crystallization. Q for primary crystallization is 3.3 eV, and Q for secondary crystallization is 3.9 eV.

This method provides an error of < 10% as long as Q/RT is greater than 30, which is typical in most cases⁷⁷.

Example Kissinger plots can be seen in Fig. 3.5 for $(\text{Fe}_{30}\text{Ni}_{70})_{80}\text{Nb}_4\text{Si}_2\text{B}_{14}$ for both primary and secondary crystallization. For primary, Q is determined to be 3.3 eV, and for secondary Q is determined to be 3.9 eV. Q determination across the Fe-Ni composition spectrum is discussed in the following section.

v. Activation Energy Determination from Thermal Analysis

DSC data was collected on a range of alloys using 20, 40, and 60 °C/min. The activation energies for primary (Q_1) and secondary (Q_2) crystallization, and the difference between the two are depicted in Fig. 3.6. Activation energies were determined by the Kissinger method. Similar to crystallization temperatures discussed in section 3.2, the values of Q for primary and secondary crystallization approach one another at high Ni contents. This implies that the remaining amorphous phase after primary crystallization in Ni-rich alloys is less stable than the remaining amorphous phase in Fe-rich alloys. It is also possible that the kinetic barrier to diffusion is lower with higher Ni content, and that allows the amorphous phase to crystallize more easily. While polymorphic transformations are observed in Co-based alloys, they have not yet been observed in Ni-based MANCs^{78,79}. Activation energies were also calculated using the Augis and Bennett method, although no significant difference was seen from the Kissinger method. Using eq. 3.3.11 on $(\text{Fe}_{70}\text{Ni}_{30})_{80}\text{Nb}_4\text{Si}_2\text{B}_{14}$ yields an Avrami exponent of 2.5. This corresponds typically to 3-dimensional growth with continuous nucleation limited by

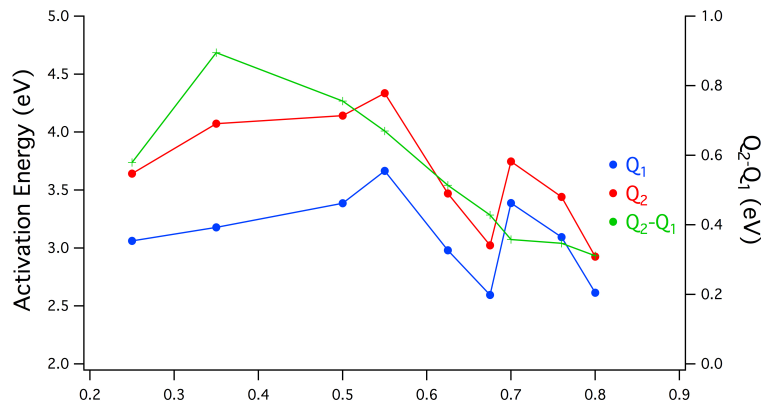


Figure 3.6: Activation energy for primary and secondary crystallization as a function of Ni fraction.

diffusion^{74,80}. For $(\text{Fe}_{70}\text{Ni}_{30})_{79}\text{Nb}_4\text{Si}_2\text{B}_{14}\text{Cu}_1$, the calculated Avrami exponent is 1.5, which corresponds to 3-dimensional growth with instantaneous nucleation. This is similar to the development of FINEMET²⁸. The values of the Avrami exponent calculated by the Augis and Bennett method have an error of $< 10\%$ ⁷⁷. A summary of Avrami parameters can be seen in Table III.I. In addition, Q_1 is 3.05 eV for the Cu containing alloy, while it is 3.3 eV for the Cu free alloy. This suggests that crystallization occurs more easily in the alloy with copper. TTT diagrams for both alloys are presented in the next section.

It is now worth discussing the physical meaning of Q . In JMAK kinetics, Q is some weighted average of individual Q 's of the occurring mechanisms, such as those for nucleation and for diffusion. There is also no reason why these activation energies should remain constant over the course of the transformation⁸¹. While it is theoretically possible to determine the change of the effective Q during a transformation, it is significantly more difficult to disentangle the individual contributions to the effective Q . With that said, as will be seen in the following section, we expect that at the temperatures where we typically anneal the samples,

Table III.I: Nucleation types and associated growth geometries and Avrami parameters (n)

Nucleation Type	Growth Geometry	n (for chemical reaction, linear law)	n (for diffusion, parabolic law)
Instantaneous Nucleation (site saturation)	Bulk 1-D	1	0.5
	Bulk 2-D	2	1
	Bulk 3-D	3	1.5
Constant Rate (homogenous nucleation)	Bulk 1-D	2	1.5
	Bulk 2-D	3	2
	Bulk 3-D	4	2.5

crystallization is diffusion limited, not nucleation limited. We therefore expect the diffusional activation energy (Q_d) to be greater than the nucleation activation energy (Q_n). Further, we expect nucleation for secondary crystallization to occur heterogeneously since the primary crystallites can act as nucleation sites. Therefore, it is likely that the activation energy for secondary crystallization is dominated by the diffusion term.

vi. TTT Diagram Determination

Developing the proper microstructure in MANCs is critical to optimizing the magnetic properties. To this end, it is beneficial to have a time-temperature-transformation (TTT) diagram for primary crystallization. In addition, due to the deleterious effects of secondary crystallization, it is important to know that a MANC device will not undergo secondary crystallization during the projected lifetime of a device at operating temperature.

The determination of the TTT diagram for both primary and secondary crystallization followed a modified procedure outlined by DeGeorge et al.⁸² Here, DSC was used in the following steps:

1. Standard constant heating from 30 °C to 40 °C below the temperature used for the isotherm
2. Time and temperature isotherm is held allowing for crystallization to occur to various stages of completion
3. Ballistic cooling to cease any ongoing crystallization from step 2
4. Standard constant heating to above the temperature at which crystallization will complete.

These steps apply for both primary and secondary crystallization. A second identical DSC scan is then taken with the same sample in the device and used as a

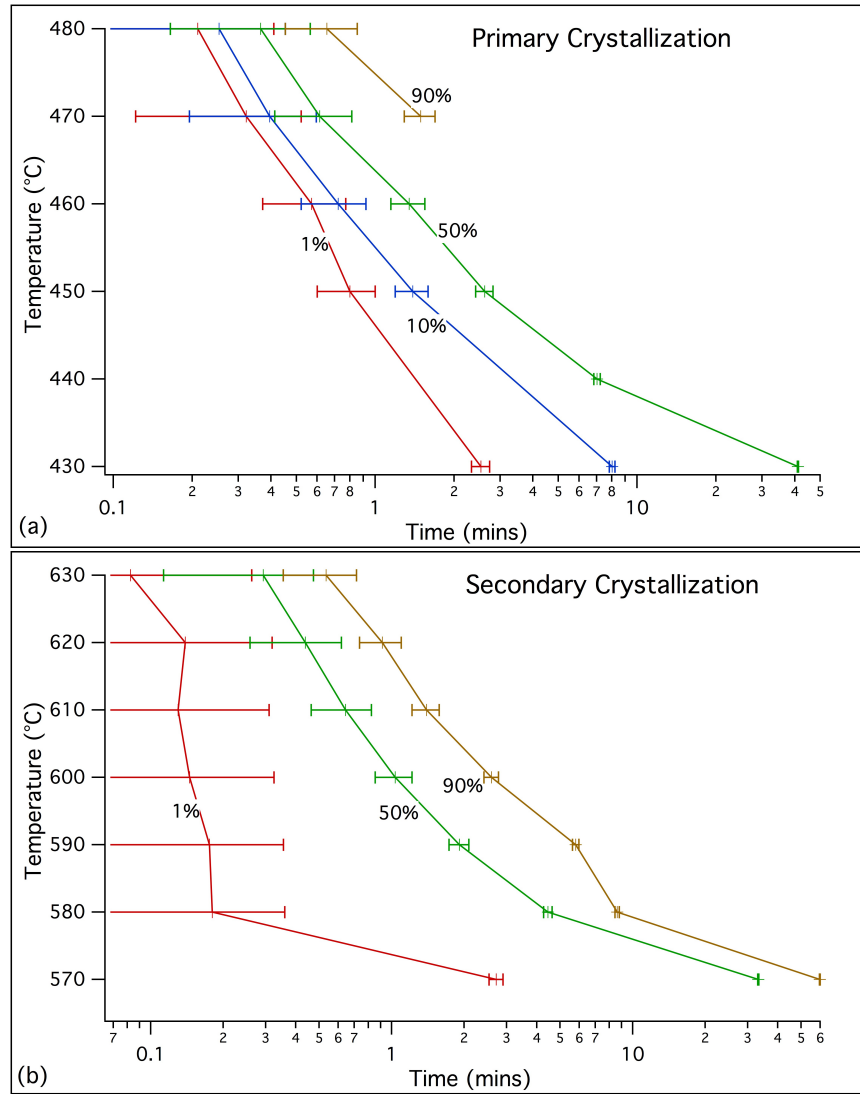


Figure 3.7: TTT diagram for (a) primary and (b) secondary crystallization for $(\text{Fe}_{70}\text{Ni}_{30})_{80}\text{Nb}_4\text{Si}_2\text{B}_{14}$.

baseline to subtract from the first. This method assumes that between steps 2 and 4, full crystallization occurs, regardless of the details of step 2. Comparing the heat evolved between steps 2 and 4, the fraction of crystallization can be determined. TTT diagrams for primary and secondary crystallization in $(\text{Fe}_{70}\text{Ni}_{30})_{80}\text{Nb}_4\text{Si}_2\text{B}_{14}$ can be seen in Fig. 3.7 (a) and (b) respectively.

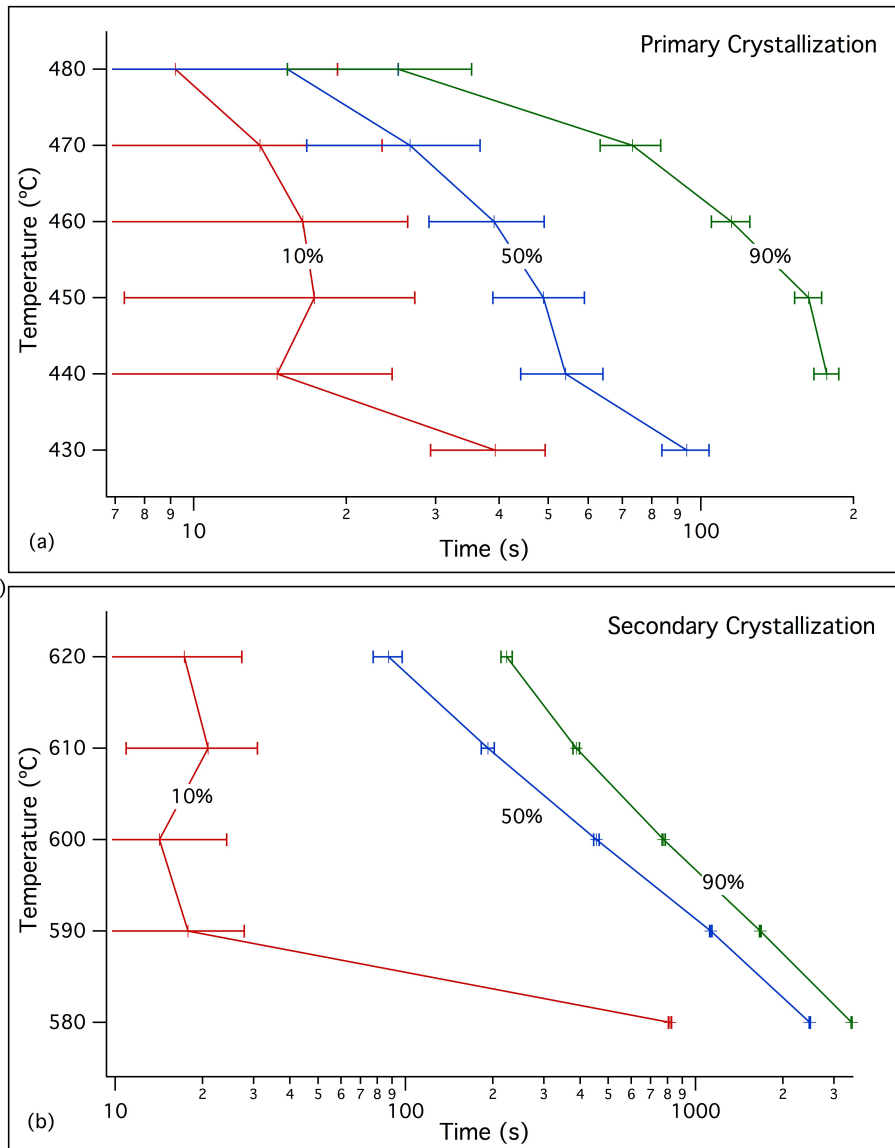


Figure 3.8: TTT diagram for (a) primary and (b) secondary crystallization for $(\text{Fe}_{70}\text{Ni}_{30})_{79}\text{Nb}_4\text{Si}_2\text{B}_{14}\text{Cu}_1$.

Based on the TTT diagrams, Kissinger determination of Q , and on equations 3.1.1, and 3.1.2, times can be predicted for arbitrary degrees of crystallization at arbitrary temperatures. From a device standpoint, we may want to avoid 1% secondary crystallization due to the deleterious effects. At 200 °C, 1% secondary crystallization is not predicted to occur for $9 \times 10^{11} \pm 6 \times 10^{11}$ years. At 300 °C, 50,000 \pm 30,000 years are predicted. At 350 °C, 90 \pm 60 years are predicted. At 400 °C, the amorphous phase is predicted to be stable for less than a year.

Fig. 3.8 depicts TTT diagrams for primary and secondary crystallization for $(\text{Fe}_{70}\text{Ni}_{30})_{79}\text{Nb}_4\text{Si}_2\text{B}_{14}\text{Cu}_1$. It can be easily seen that primary crystallization occurs much more rapidly for the Cu containing alloy than for the Cu free alloy. At 300 °C, $2,000 \pm 1,000$ years are predicted. At 350 °C, 13 ± 6 years are predicted. Secondary crystallization also occurs more easily than in Cu-free alloy, which can be seen by a lowering of Q_2 from 3.9 to 3.1 when Cu is added to the alloy. It is worth noting that these TTT diagrams consist only of the bottom half of a traditional TTT diagram (below the “nose”.) This tells us that at these annealing temperatures, crystallization is diffusion limited.

vii. Kinetics from Magnetometry

Magnetization versus time experiments can help determine aspects of the crystallization kinetics. The details of magnetometry are discussed below in section 5.1. Fig. 3.9 depicts magnetization as a function of time at various temperatures for

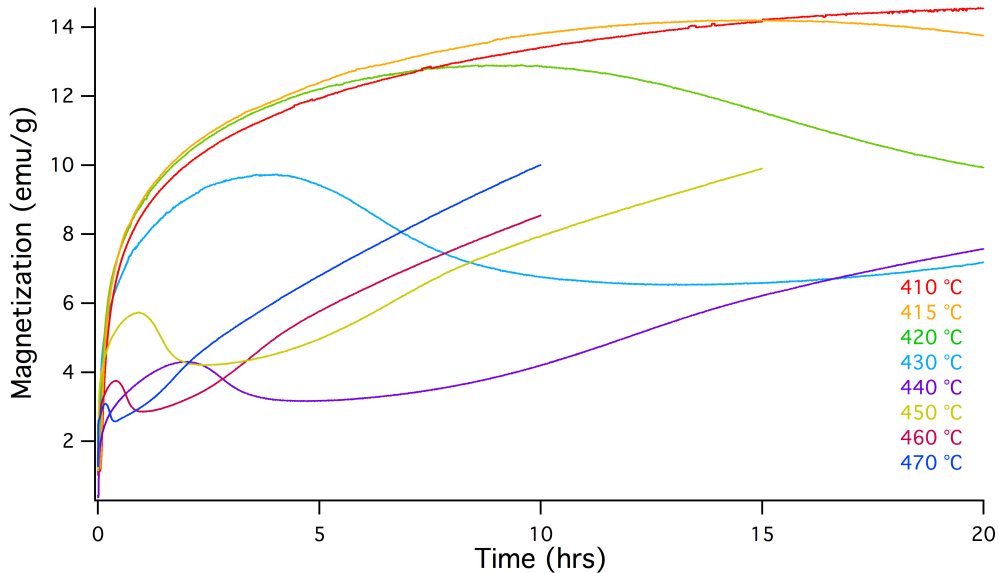


Figure 3.9: Magnetization vs. time for $(\text{Fe}_{30}\text{Ni}_{70})_{80}\text{Nb}_4\text{Si}_2\text{B}_{14}$ at temperature.

a $(\text{Fe}_{30}\text{Ni}_{70})_{80}\text{Nb}_4\text{Si}_2\text{B}_{14}$ sample. At all temperatures above 420 °C, the magnetization reaches a maximum, decreases, and then increases again. In order for this to occur, the secondary crystallites must consume some of the crystals formed during primary crystallization. Secondary crystallization occurs at these low temperatures due to the relative instability of the amorphous phase in high Ni alloys, and possibly also due to lower migrational energy as noted earlier. With higher Fe, secondary crystallization is not observed at lower temperatures. The decrease in the maximum magnetization is due to approaching the Curie temperature of the primary crystallites (~ 500 °C).

As primary crystallization occurs, the amorphous matrix becomes enriched in glass forming atoms. Once the ratio of Fe and Ni to B and Nb lowers enough, the amorphous matrix may be able to undergo a diffusionless polymorphic transition to the 23:6 phase⁷⁹.

viii. Strain-Annealing and Elongation



Figure 3.10: The large-scale strain-annealer at CMU. The furnace can be seen in the center, and tension rollers are located on the sides.

Strain-annealing is a process where a strain is applied to amorphous ribbon during the crystallization process. On an industrial scale strain-annealer, it is possible to vary the strain along the length of the ribbon. Because strain-annealing tunes the permeability, it is possible to vary the permeability spatially within a device. The large-scale strain-annealer at CMU is shown in Fig. 3.10. Strain-annealing is used to tune the permeability of the material and to help decrease anomalous losses. Here, it is noted that significant flow is seen in some alloys during strain annealing. Elongation as a function of %Ni and applied stress can be seen in Fig. 3.11. At 200 MPa, all alloys have approximately the same elongation. However, when the stress is increased to 300 MPa, elongation is clearly higher at the 50-50 Fe-Ni composition. This elongation does not occur simply above the glass transition temperature, but largely occurs once the ribbon is near or at the crystallization temperature. The benefit of this behavior is that it may allow for easy stamping/shaping of the alloy at elevated temperatures for complex geometry applications. The mechanism of this elongation is currently being investigated.

Such significant elongations may be characterized as superplastic deformation. A metallic glass above its T_g becomes a viscous supercooled liquid capable of viscous flow. The viscosity between T_g and the crystallization temperature can change by seven orders of magnitude^{83,84}. The mechanism of the significant elongations seen in Fe-Ni MANCs could be examined in the future by creep tests and/or high temperature tensile tests⁸⁵.

ix. Conclusions

JMAK kinetics were discussed and provide the basis for kinetics analysis and constructing TTT diagrams. Primary and secondary crystallization temperatures are determined by DSC, with the two approaching one another at high Ni concentrations. This is due to the higher electron concentration present at higher amounts of Ni. A summary of using thermal analysis to determine kinetic parameters is presented via Kissinger analysis and the Augis and Bennett method. These allow for determination of activation energies for primary and secondary crystallization, along with the determination of the Avrami exponent for primary. TTT diagrams for primary and secondary crystallization are presented for $(\text{Fe}_{70}\text{Ni}_{30})_{80}\text{Nb}_4\text{Si}_2\text{B}_{14}$ and $(\text{Fe}_{70}\text{Ni}_{30})_{79}\text{Nb}_4\text{Si}_2\text{B}_{14}\text{Cu}_1$. The TTT diagrams showed that adding copper increased the rate of crystallization for both primary and secondary crystallization, which is corroborated by their respective activation energies. In addition, TTT diagrams allowed for predictions of device stability assuming 1% secondary crystallization is to be avoided. Lastly, trends of elongation as a function of composition and applied stress were examined. Hypothesis 5 stated:

“Crystallization kinetic studies will explain the stability of the nanocomposite within a temperature range of interest as well as predicting the volume fraction of nanocrystals as a function of time and temperature following nanocrystallization”

This hypothesis has been demonstrated in this chapter.

IV. Structure

i. Basics of X-ray Diffraction

Once a ribbon has been cast by planar flow casting, a quick check of amorphisivity can be done by a bend test⁸⁶. However, for conclusive results, x-ray diffraction (XRD) must be done. The governing equation for XRD is Bragg's law:

$$2d \sin \theta = n\lambda \quad (4.1.1)$$

d is the crystallographic inter-planar spacing, θ is the angle, and λ is the x-ray wavelength used. In an ideal crystalline material, the diffraction pattern will consist of a series of delta functions whose locations correspond to Bragg's law.

In a real material, instead of delta functions, the diffraction pattern will consist of a series of Gaussian-like peaks, whose locations will correspond to Bragg's law, but their widths and relative heights will depend on factors such as crystallite size and shape, crystal texturing, and instrumental broadening. With measured peaks, it is possible to estimate the size of the crystallites by using the Scherrer equation:

$$\tau = \frac{K\lambda}{\beta \cos \theta} \quad (4.1.2)$$

where K is a dimensionless shape factor (typically 0.9), and β is the breadth of the diffraction peak in radians. However, in addition to crystallite size, crystal strain can cause peak broadening as well. This strain can arise from various crystal defects or coherency strains inherent in the system.

For an amorphous material, there are no crystallographic planes, so there are no inter-planar spacings. Instead, there is a distribution of interatomic spacings

which lead to a broad peak called an amorphous halo. This halo is centered at the angle that corresponds to the mean interatomic spacing^{87,88}.

ii. Energy Dispersive XRD and Pressure

XRD can also be done using an energy dispersive technique. In ED-XRD, the angle of measurement is fixed, and a spectrum of x-ray energies, and hence, wavelengths, are used. Using a Paris Edinburg cell on Sector 16-BM-B (HPCAT) at the Advanced Photon Source⁸⁹⁻⁹¹, high pressure ED-XRD can be done. For each experiment, the sample and a Au calibration standard are loaded into a custom gasket assembly containing a hexagonal boron nitride capsule as described by Yamada et al.⁸⁹ The initial pressure for each experiment can be determined by applying the equation of state to the room temperature lattice parameter of Au under load⁹². Direct current through a graphite sleeve surrounding the capsule heated the sample and calibration material. For ED-XRD, the Bragg law can be written where the energy for a reflection E_{hkl} is measured in keV and lattice spacing d_{hkl} is given in Å for a fixed angle θ_0 ^{93,94}

$$E_{hkl} = \frac{6.199}{d_{hkl} \sin(\theta_0)} \quad (4.2.1)$$

The corresponding Scherrer equation for ED-XRD is:

$$D = \frac{K \times 6.199}{\beta_s \sin(\theta_0)} \quad (4.2.2)$$

where D is crystallite size.

Experimentally, pressure studies in this text were done using a Paris-Edinburg cell on Sector 16-BM-B (HPCAT) at the Advanced Photon Source

(APS)^{89,90}. The sample and a Au calibration standard were loaded into a gasket assembly containing a hexagonal-BN capsule as described by Yamada et al⁸⁹. Direct current through a graphite sleeve inside the BN capsule provides heat to the sample and Au foil. Pressure is applied pneumatically via a tungsten carbide and steel anvil. A sketch of a Paris-Edinburgh cell can be seen in Fig. 4.1.

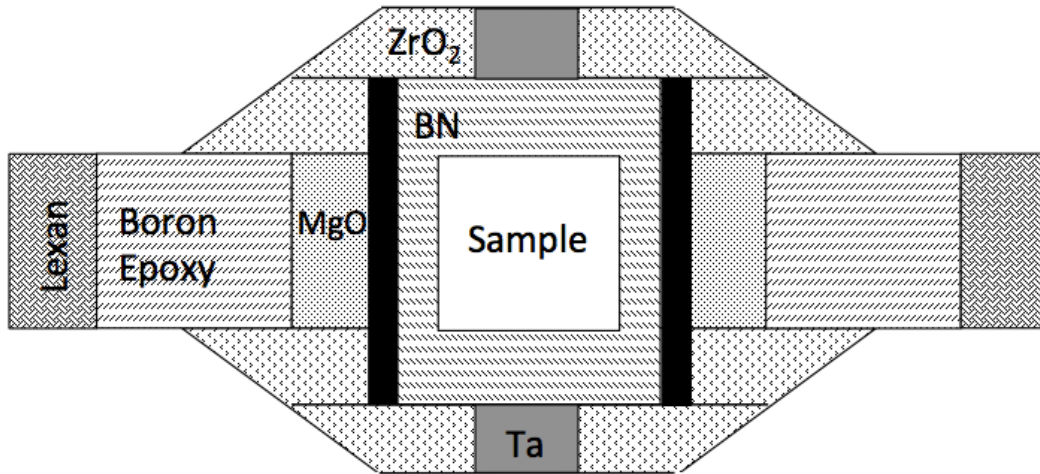


Figure 4.1: Sketch of a Paris-Edinburgh cell used at APS. Adapted from Kono et al.⁹⁰

iii: Crystallization and Pressure Effects in the Fe-Nd-B system

$\text{Fe}_{87.4}\text{Nd}_{8.2}\text{B}_{4.4}$ (NB1) and $\text{Fe}_{89.1}\text{Nd}_{5.9}\text{B}_{5.0}$ (NB3) amorphous alloys were fabricated in order to study pressure effects on the crystallization temperature, and grain growth of Fe crystallites in a technologically important hard/soft magnetic nanocomposite phase. FeNdB materials are state of the art permanent magnets in offering the largest magnetic energy products recorded. However, they are subject to the issues of rare earth criticality discussed above and therefore there have been significant worldwide efforts aimed at optimizing properties further in RE-lean hard/soft nanocomposite systems. In these nanocomposites, pressure effects on

the $\alpha \rightarrow \gamma$ phase transformation can be examined which can be compared with those seen in Fe-Ni systems in the future.

The compositions reported here were chosen to abut the 4% B isopleth in the Fe-Nd-B phase diagram⁹⁵. Fig. 4.2 shows waterfall plots of ED-XRD data for body centered cubic (bcc) {011} and face centered cubic (fcc) {111} and {002} reflections for the α - and γ -phases of Fe, respectively at two pressures each. The plots show peak intensity from 30-80 keV and clearly show the $\alpha \rightarrow \gamma$ -phase transformation. Peak intensity near 38 keV is due to Nd fluorescence. The bcc {002} and fcc {002} reflections were fit to Gaussian/Lorentzian shapes from which the nominal nanostructure size of the α -Fe and γ -Fe was estimated using a Scherrer analysis^{96,97}.

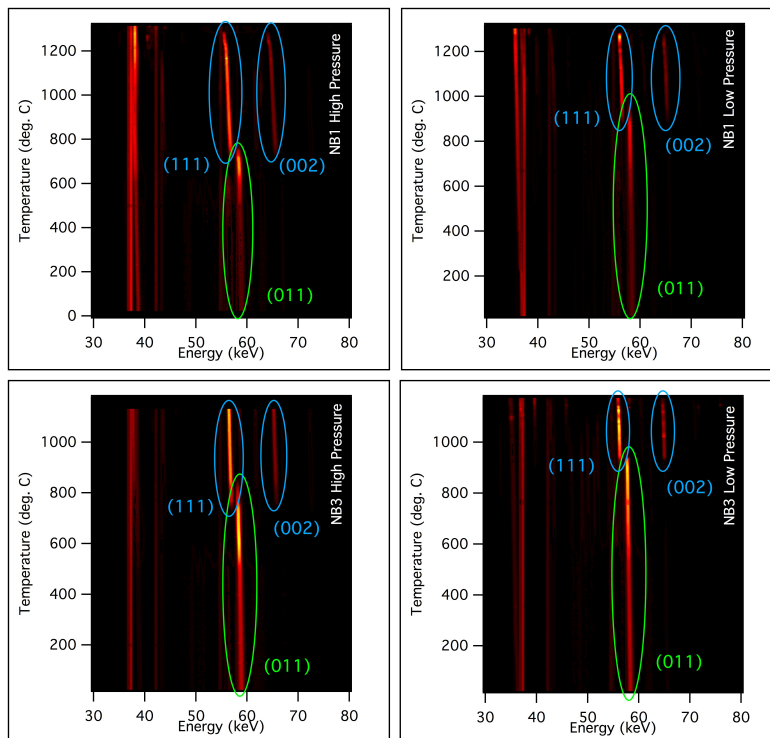


Figure 4.2: Waterfall plots of synchrotron x-ray diffraction data for the bcc and fcc reflections for the α - and γ - phases of Fe respectively (a) NB1 2.2GPa, (b) NB1 5.0 GPa, (c) NB3 0.9 GPa, and (d) NB3 4.6 GPa.

From these plots it can be seen that there is a range of temperatures over which the α -Fe and γ -Fe coexist in the ternary system.

The Fe nanostructure size scale is determined from Scherrer analysis of x-ray diffraction data. The {002} peaks for bcc and fcc were fitted with a Gaussian curve. For a Gaussian, the width of the peak is simply related to the integral breadth by:

$$\beta = w\sqrt{\pi} \quad (4.4.1)$$

where β is the integral breadth and w is the width. Instrumental broadening is then removed from the peak integral breadth via quadratic subtraction. The resulting integral breadth can be attributed to crystal size and strain effects. Ignoring the strain effects, the calculated integral breadth β_s was used to estimate the crystal size using the Scherrer equation for energy dispersive x-ray diffraction seen in eq. 4.2.2.

The Scherrer analysis of the peak breadths for the bcc {002} and fcc {002} reflections for the α - and γ - phases as a function of temperature at the experimental

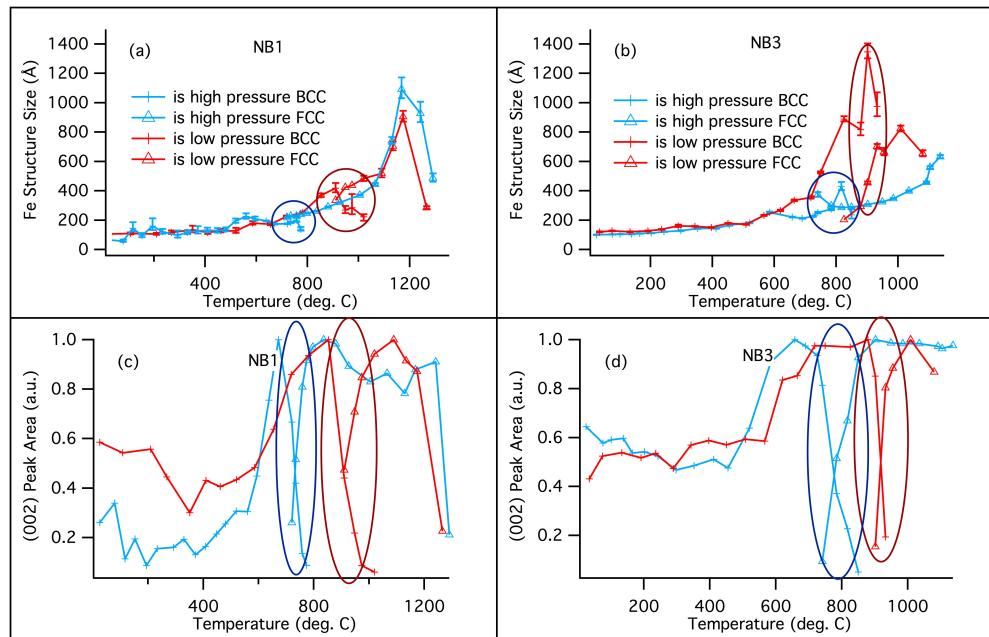


Figure 4.3: Fe nanostructure size scale as determined from Scherrer analysis of XRD data for the (002) reflection for the α - and γ -phases vs. temperature at 1.0 and 5 GPa, for sample composition (a) NB1 and (b) NB3. (c) and (d) are (002) peak area as a function of temperature.

pressures are shown in Figure 4.3. Data for composition (a) NB1 and (b) NB3, respectively, for flakes heated to over 1000 °C show the evolution of the characteristic size of the Fe nanostructures. In both cases the as-cast samples have some nominally 10-12 nm α -Fe in the amorphous matrix. The characteristic size scale of the α -Fe increases significantly on approaching the $\alpha \rightarrow \gamma$ -phase transformation temperature with noticeable pressure dependence of this growth. Above the $\alpha \rightarrow \gamma$ -phase transformation temperature the γ -Fe phase continues to grow. This growth appears to be significantly suppressed at higher pressures. In contrast to the isopleth published⁹⁵ for atmospheric pressure, both compositions appear to have an ~ 100 °C range of temperature over which the α and γ -phases coexist.

A region of coexistence between the α and γ phases over a range of temperatures is possible in ternary and the multicomponent systems and has been seen for example in Fe-Ni-Zr-B(Cu) systems³⁴. The coexistence is potentially related to differences in particle size and interfacial effects, but differences between flake and powdered samples are ambiguous at present. The coexistence regions are marked with ovals in the figure. The area of coexistence is easily seen in (c) and (d). These are plots of the {002} peak areas with temperature. The high temperature Fe structure size decrease in (a) and (c) are due to melting.

The pressure dependence of the Fe particle size growth is consistent with a defect mediated diffusional growth process⁹⁸. In the as-cast state, these materials contain significant amorphous phase content and the diffusion of Fe atoms can be

suppressed by pressure. Suppression of diffusion by pressure will be examined in more detail below in section **IV.vi**.

In the context of Herzer's random magnetic anisotropy model for soft magnetic nanocomposites⁴³ an exchange length is calculated as proportional to $(A/K)^{1/2}$ where A is the exchange stiffness and K is the magnetic anisotropy. For a hard material like the 2:14:1 phase, this length is ~ 1 nm whereas for soft Fe it is an order of magnitude greater, ~ 20 nm. In this light, the data of Fig. 4.3 is quite significant. The soft-Fe size is considerably smaller than its exchange length for $T < \sim 600$ °C. Both Scherrer and peak area analysis indicate considerable coarsening in the vicinity of the $\alpha \rightarrow \gamma$ -phase transformation. It is perhaps not surprising that the rate of attachment of Fe from any remaining amorphous phase to the FCC phase is correlated to increased coarsening. Note that the suppression of the $\alpha \rightarrow \gamma$ -phase transformation temperature with pressure is anomalous and can be explained in terms of magnetic contributions to the enthalpy and entropy of the phase transformation⁹¹.

These results motivate similar work to be done on the Fe-Ni MANC system. Below we will examine how pressure affects the phase stability and the structure in Fe-Ni MANCs. Because Fe is a primary component of these nanocomposites, it is worth examining the peculiarities of the thermodynamics and phase transitions in pure Fe.

iv. Allotropes and the Thermodynamics of Phase Transitions in Iron

Understanding the role of magnetism on polymorphism of iron, i.e., answering the question of what the conditions are that stabilize the various

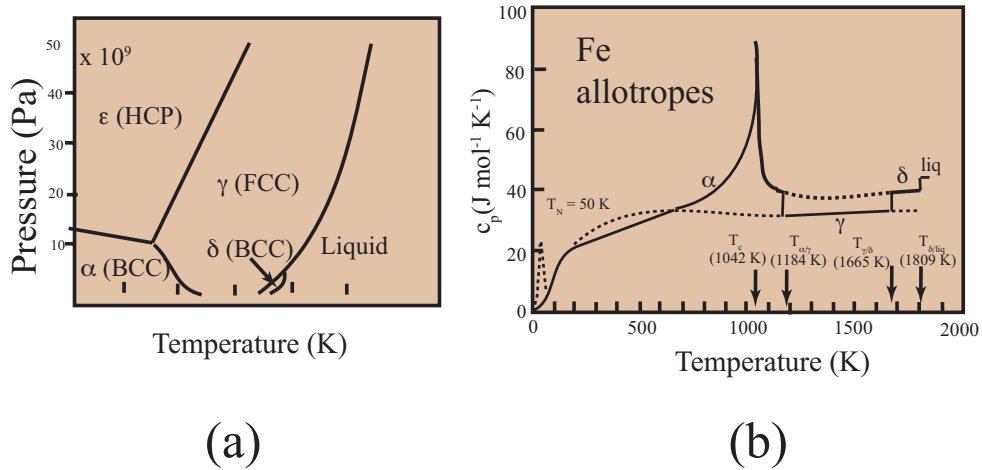


Figure 4.4: (a) P-T phase diagram⁹⁹ and (b) heat capacity vs. temperature for pure iron⁵⁷.

allotropes of iron help to design Fe-containing alloys. Iron has two phases with different crystal structures at atmospheric pressure: the bcc α and the fcc γ . In the ground state the bcc ferromagnetic α -phase is stable. At atmospheric pressure and 1184 K α -Fe transforms into γ -Fe, which is stable up to 1665 K where it transforms to the paramagnetic bcc δ -Fe. At pressures in excess of 10 GPa an hcp allotrope, ϵ -Fe, is observed as shown in Fig. 4.4 (a)⁹⁹. Polymorphism of iron, and especially the α - γ transformation, is the basis for the occurrence of a broad range of structures and technologically important properties in iron alloys. Without it, the wide spectrum of applications of iron alloys would have not been possible.

Structural transformations in iron occur with a first order transformation as in the liquid-solid transformation^{26,100}. Such a transformation is accompanied by a sudden change in the entropy and other physical properties and has a latent heat. γ -Fe below its stability range would have ordered antiferromagnetically (AF) below

about 50 K as illustrated in the heat capacity data of Fig. 4.4(b). In this regard Fe disobeys a general rule of polymorphism that the high temperature crystal structure is closer packed (e.g., fcc or hcp) than the low temperature structure (e.g., bcc). The reason for this exception lies in the unusual magnetic properties of iron^{26,101}. Magnetic field effects are increasingly being studied in their influence on phase equilibria^{102,103}.

v. Crystallization Products in the Fe-Ni MANC System

When the amorphous ribbon is cast, amorphisivity is first checked with a bend test⁸⁶, and then confirmed with XRD. As can be seen in Fig. 4.6, Fe-rich alloys

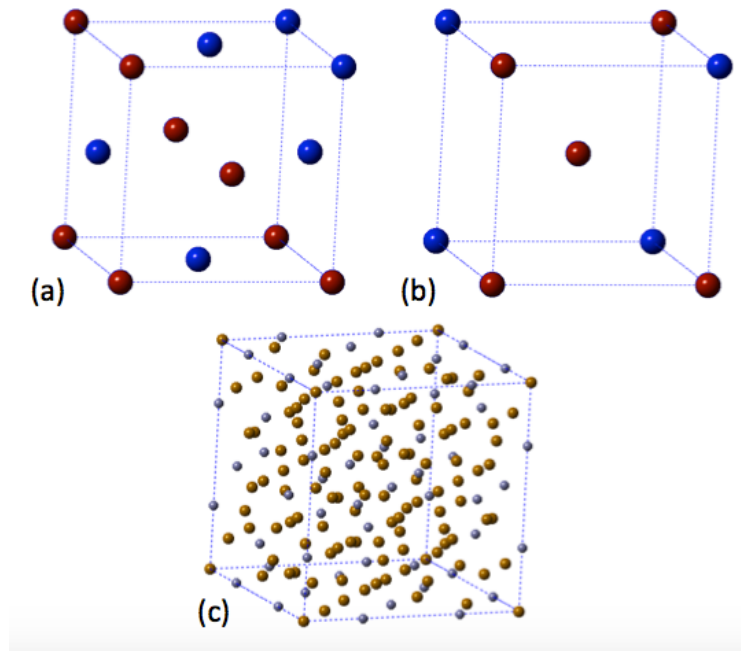


Figure 4.5: (a) γ -FeNi, (b) α -FeNi with random atomic assignment to lattice positions, and (c) Cr_{23}C_6

develop α -FeNi, while Ni-rich alloys develop γ -FeNi during primary crystallization. In addition, secondary crystallization products are identified as a Cr_{23}C_6 -type compound. These three crystal structures can be seen in Fig. 4.5. Secondary crystallization^{104,105} is particularly easy and occurs at lower temperatures for Ni-

rich alloys as discussed above in chapter 3.5. It has been calculated that the Ni_{23}B_6 structure is unstable, but ternary additions help stabilize the Ni rich 23:6 phase structure more effectively than the Fe-rich 23:6 phase structure¹⁰⁴. Because of the stability of the amorphous phase, and the better magnetic properties of the Fe-rich alloys, further experiments focused on the Fe-rich end of the spectrum.

Ribbon from across the Fe-Ni spectrum were annealed, and strain annealed at 440 °C for 10 minutes. Strain annealing was done at both 200 and 300 MPa. XRD results from these samples are shown in Fig. 4.7. All samples showed γ -FeNi as the primary crystallization product. The $(\text{Fe}_{30}\text{Ni}_{70})_{80}\text{Nb}_4\text{Si}_2\text{B}_{14}$ samples show Cr_{23}C_6 -type peaks due to secondary crystallization^{104,105} which occurs at lower temperatures for this alloy than for the more Fe-rich alloys. Scherrer analysis

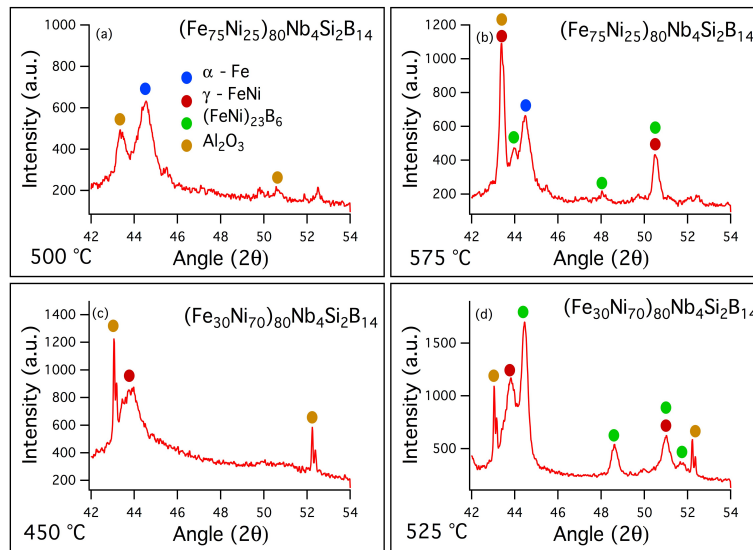


Figure 4.6: (a) and (b) $(\text{Fe}_{75}\text{Ni}_{25})_{80}\text{Nb}_4\text{Si}_2\text{B}_{14}$ at heated to 500 °C and 575 °C respectively. (c) and (d) $(\text{Fe}_{30}\text{Ni}_{70})_{80}\text{Nb}_4\text{Si}_2\text{B}_{14}$ heated to 450 °C and 525 °C respectively.

provided no experimentally significant evidence for a difference between crystal sizes of annealed and strain-annealed samples. Calculated crystal sizes ranged from

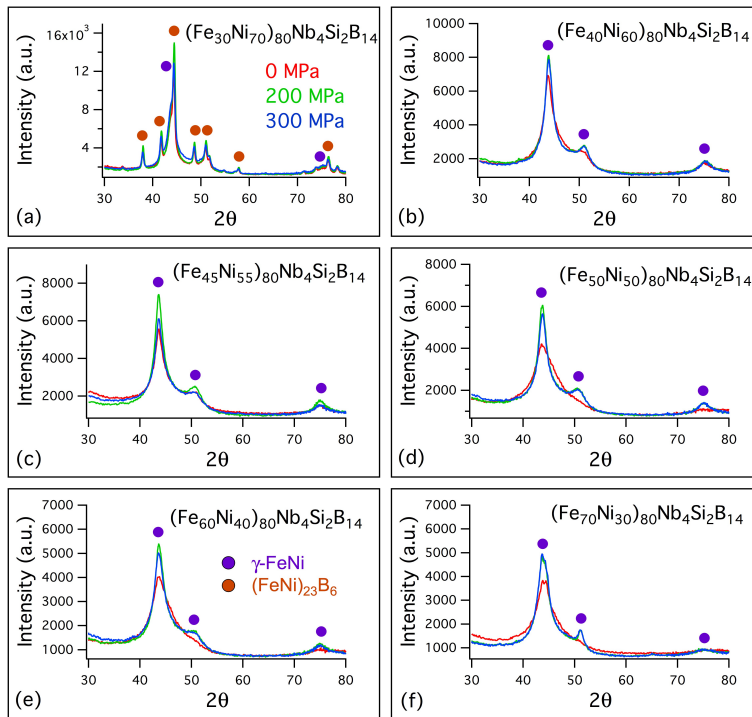


Figure 4.7: XRD of annealed and strain-annealed alloys for (a) $(\text{Fe}_{30}\text{Ni}_{70})_{80}\text{Nb}_4\text{Si}_2\text{B}_{14}$, (b) $(\text{Fe}_{40}\text{Ni}_{60})_{80}\text{Nb}_4\text{Si}_2\text{B}_{14}$, (c) $(\text{Fe}_{45}\text{Ni}_{55})_{80}\text{Nb}_4\text{Si}_2\text{B}_{14}$, (d) $(\text{Fe}_{50}\text{Ni}_{50})_{80}\text{Nb}_4\text{Si}_2\text{B}_{14}$, (e) $(\text{Fe}_{60}\text{Ni}_{40})_{80}\text{Nb}_4\text{Si}_2\text{B}_{14}$, (f) $(\text{Fe}_{70}\text{Ni}_{30})_{80}\text{Nb}_4\text{Si}_2\text{B}_{14}$.

12-20 nm. It is also worth noting, that since Fe and Ni are so close on the periodic table, ordering in the $L1_0$ or $L1_2$ phase would be difficult to detect from a standard XRD scan. As such, a 24 hour scan was done on an annealed $(\text{Fe}_{30}\text{Ni}_{70})_{80}\text{Nb}_4\text{Si}_2\text{B}_{14}$ sample, but no superlattice peaks could be resolved.

Alloys were made with V, Cr, Nb, and Mo additions in order to examine how these elements affect electrical and magnetic properties as detailed in Chapter V. Fig. 4.8 shows the XRD of some of these alloys, which were annealed and strain-annealed. It can be observed that an fcc (002) peak is visible, but any lower angle peak is washed out in the residual amorphous peak.

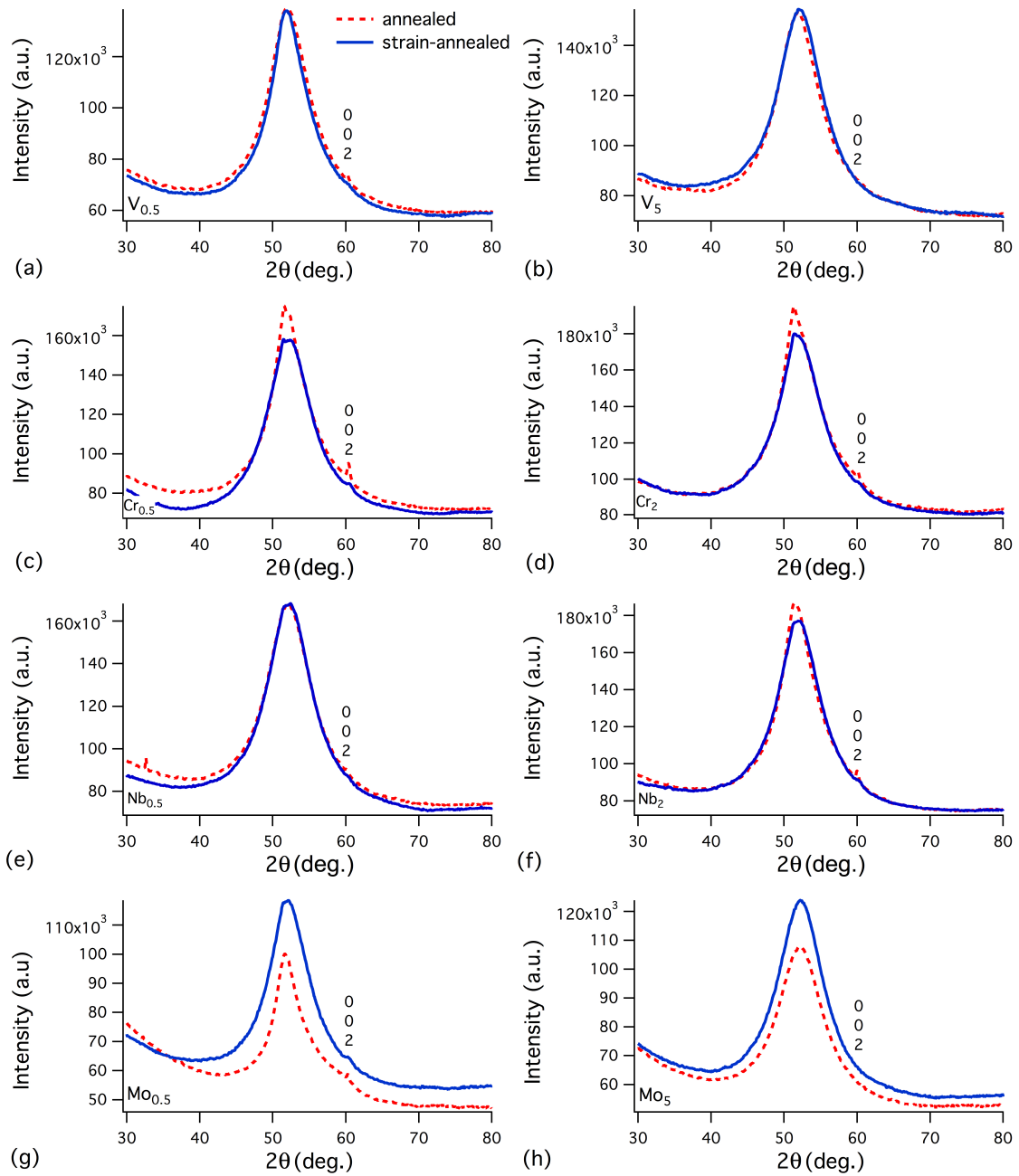


Figure 4.8: XRD of (a) $V_{0.5}$, (b) V_5 , (c) $Cr_{0.5}$, (d) Cr_2 , (e) $Nb_{0.5}$, (f) Nb_2 , (g) $Mo_{0.5}$, and (h) Mo_5 alloys.

Transmission electron microscopy (TEM) has also been performed on $(\text{Fe}_{70}\text{Ni}_{30})_{80}\text{Nb}_4\text{Si}_2\text{B}_{14}$ with heat treatments of 420 °C, 440 °C, and 480 °C under Ar

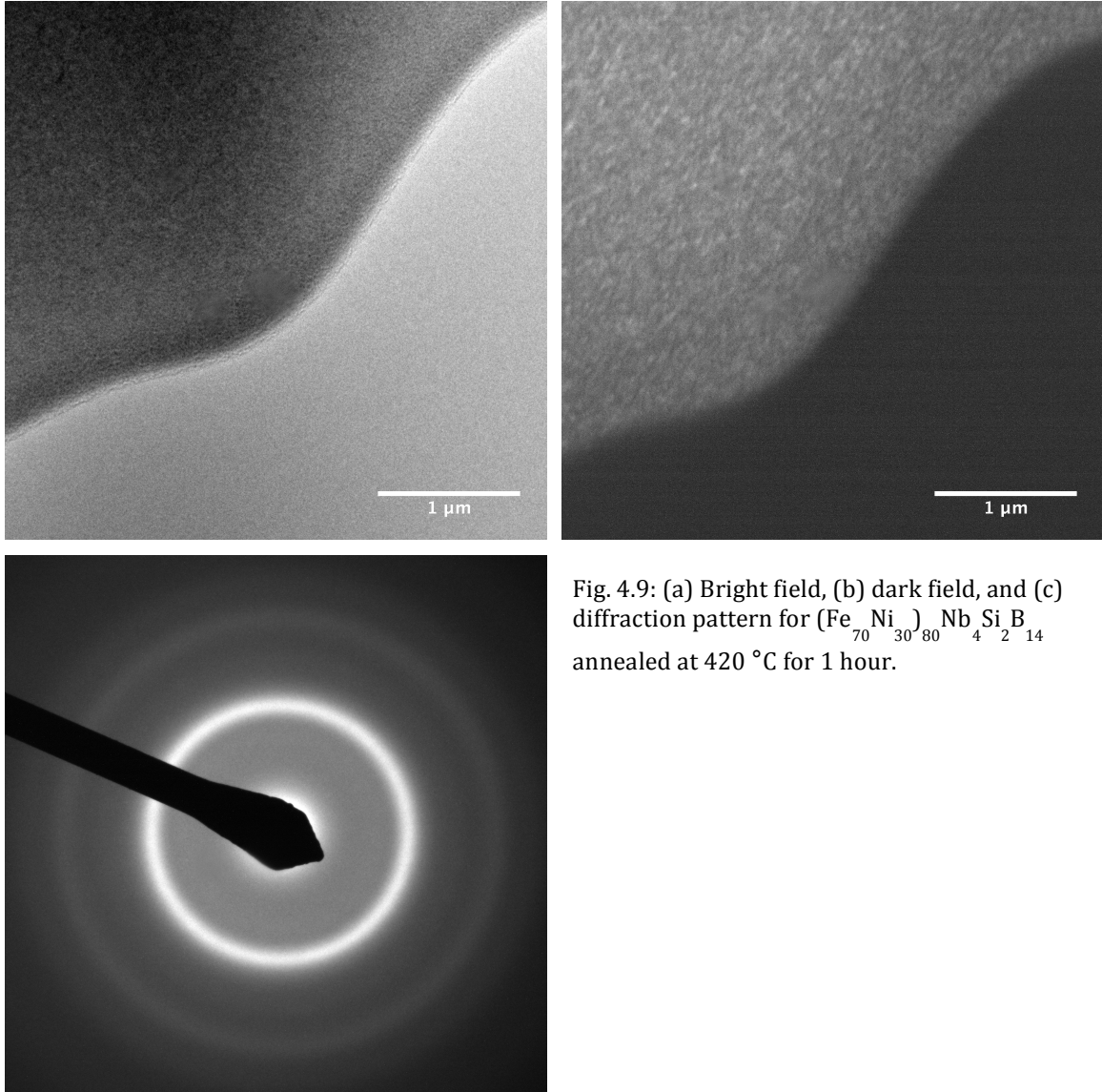


Fig. 4.9: (a) Bright field, (b) dark field, and (c) diffraction pattern for $(\text{Fe}_{70}\text{Ni}_{30})_{80}\text{Nb}_4\text{Si}_2\text{B}_{14}$ annealed at 420 °C for 1 hour.

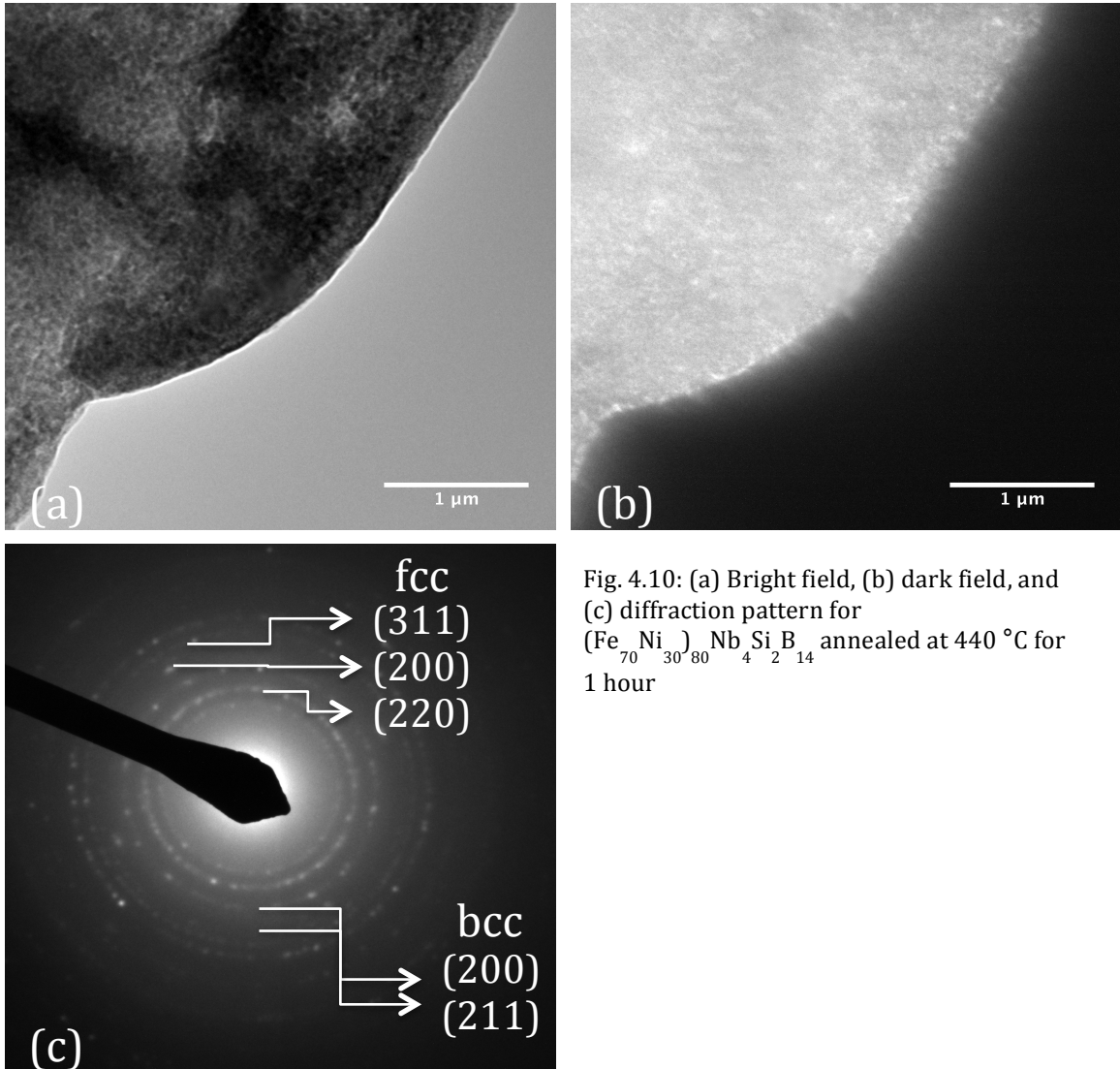


Fig. 4.10: (a) Bright field, (b) dark field, and (c) diffraction pattern for $(\text{Fe}_{70}\text{Ni}_{30})_4\text{Nb}_4\text{Si}_2\text{B}_{14}$ annealed at 440 °C for 1 hour

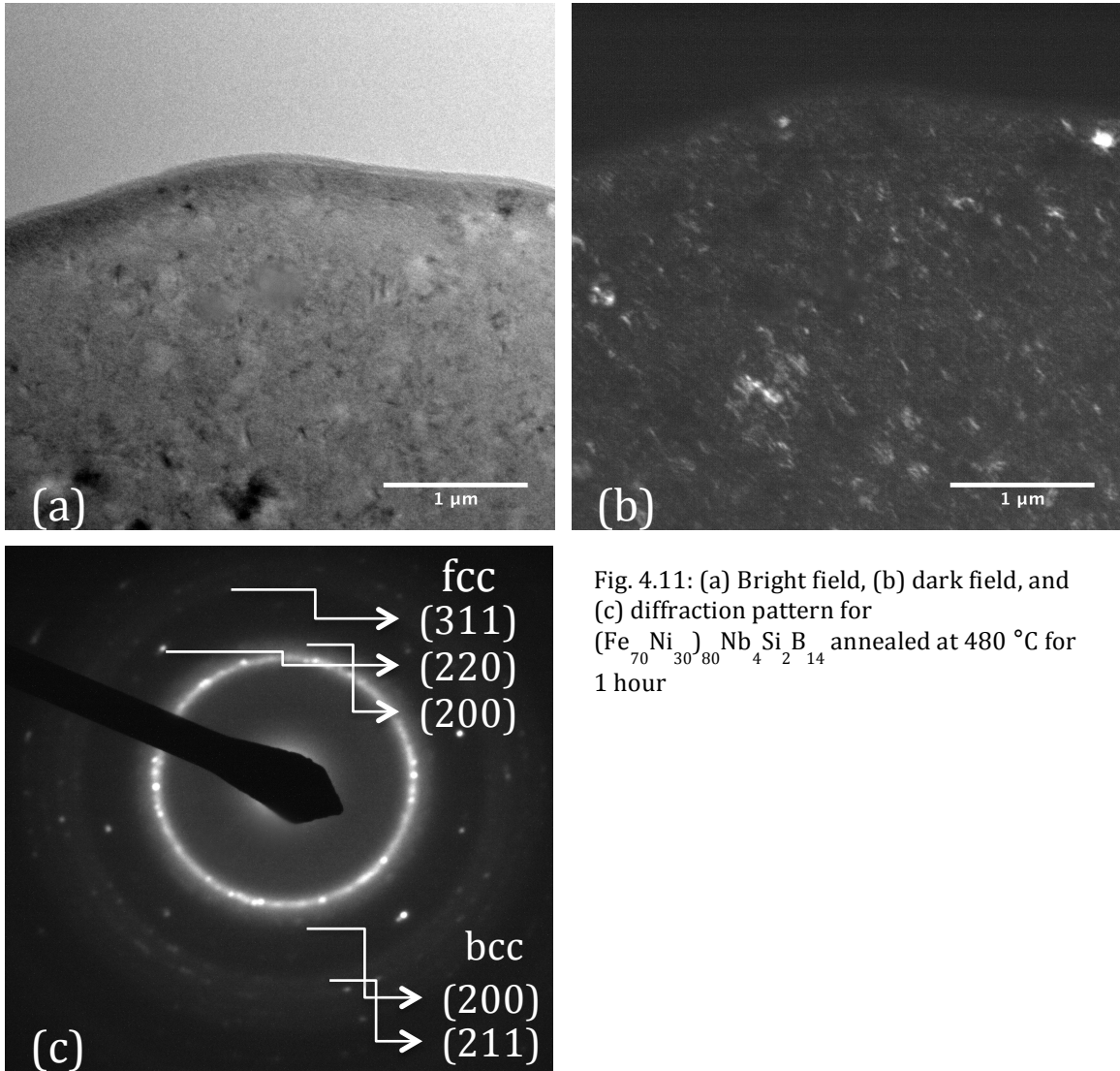


Fig. 4.11: (a) Bright field, (b) dark field, and (c) diffraction pattern for $(\text{Fe}_{70}\text{Ni}_{30})_4\text{Nb}_4\text{Si}_2\text{B}_{14}$ annealed at 480 °C for 1 hour

atmosphere. Bright field, dark field, and diffraction images were all collected and can be seen in Figures 4.9-4.11. (a) frames show the bright field images, (b) frames show dark field, and (c) show the diffraction patterns. The diffraction images for 420 °C show broad amorphous peaks, while 440 °C and 480 °C show rings arising from both γ -FeNi and α -FeNi. The 480 °C images shows signs of larger grains, which can be clearly seen in the dark field image. The dark field image for 420 °C shows very small crystallites, but it is hard to discern. For 440 °C, crystallites can be more clearly made out, but they are still small. TEM shows evidence of α -FeNi while XRD

did not. This is because the (111) peaks for γ -FeNi and α -FeNi are very close, and also overlap the amorphous halo. The higher order α peaks are very weak, and therefore were not detected in XRD.

vi. Pressure Effects on Crystallization in the Fe-Ni MANC System

Much like in the Fe-Nd-B system discussed in section 4.4, a Paris-Edinburgh cell was used at APS for EDXRD for some specific Fe-Ni MANC alloys. Structures of $(\text{Fe}_{30}\text{Ni}_{70})_{80}\text{Nb}_4\text{Si}_2\text{B}_{14}$ samples were determined at 1.5 GPa and 5.6 GPa, respectively. Structures of $(\text{Fe}_{65}\text{Ni}_{35})_{80}\text{Nb}_4\text{Si}_2\text{B}_{14}$ was determined at 4.9 GPa, and $(\text{Fe}_{75}\text{Ni}_{25})_{80}\text{Nb}_4\text{Si}_2\text{B}_{14}$ was determined at 4.8 GPa. These three alloys were also measured at atmospheric pressure in a high temperature XRD (HTXRD) along with an $(\text{Fe}_{72.5}\text{Ni}_{27.5})_{80}\text{Nb}_4\text{Si}_2\text{B}_{14}$ alloy.

Table IV.I: Summary of crystallization temperature and primary crystal phase identity at tested pressures for $(\text{Fe}_{30}\text{Ni}_{70})_{80}\text{Nb}_4\text{Si}_2\text{B}_{14}$, $(\text{Fe}_{65}\text{Ni}_{35})_{80}\text{Nb}_4\text{Si}_2\text{B}_{14}$, $(\text{Fe}_{72.5}\text{Ni}_{27.5})_{80}\text{Nb}_4\text{Si}_2\text{B}_{14}$, and $(\text{Fe}_{75}\text{Ni}_{25})_{80}\text{Nb}_4\text{Si}_2\text{B}_{14}$.

Composition	Pressure	Crystallization Temperature (°C)	Phase
$(\text{Fe}_{30}\text{Ni}_{70})_{80}\text{Nb}_4\text{Si}_2\text{B}_{14}$	Atm	423	γ
	1.5 GPa	460	γ
	5.6 GPa	N/A	γ
$(\text{Fe}_{65}\text{Ni}_{35})_{80}\text{Nb}_4\text{Si}_2\text{B}_{14}$	Atm	450-500	γ
	4.9 GPa	600	γ
$(\text{Fe}_{72.5}\text{Ni}_{27.5})_{80}\text{Nb}_4\text{Si}_2\text{B}_{14}$	Atm	450/550	α/γ
	4.8 GPa	530	γ

Table IV.I summarizes the primary crystallization temperatures and resulting phases for the alloys examined here. As predicted by the Fe-Ni equilibrium phase diagram, $(\text{Fe}_{30}\text{Ni}_{70})_{80}\text{Nb}_4\text{Si}_2\text{B}_{14}$ only forms γ -FeNi during primary crystallization. $(\text{Fe}_{72.5}\text{Ni}_{27.5})_{80}\text{Nb}_4\text{Si}_2\text{B}_{14}$ and $(\text{Fe}_{75}\text{Ni}_{25})_{80}\text{Nb}_4\text{Si}_2\text{B}_{14}$ both form α -FeNi

first, and then γ -FeNi at somewhat higher temperatures as indicated in Table IV.I. Crystallite size by Scherrer analysis as a function of temperature for various alloys can be seen in Fig. 4.12. The same procedure was followed as discussed previously in sections 4.2 and 4.3, and a representative EDXRD scan is shown in Fig. 4.13. Phases that are stable for an extended temperature range generally grow as temperature is increased. A significant difference between γ -FeNi growth can be seen for $(\text{Fe}_{30}\text{Ni}_{70})_{80}\text{Nb}_4\text{Si}_2\text{B}_{14}$ at atmospheric pressure and 5.6 GPa. At atmospheric pressure, the crystallites grow from ~ 8 nm to over 35 nm over a 250 °C temperature change. However, at 5.6 GPa of pressure, the γ -FeNi crystallite growth is suppressed, with size staying near 10 nm. Grain growth is a diffusion driven process, suggesting that the application of pressure suppresses diffusion by reducing the overall free volume available in the amorphous phase. The diffusivity, D , in an amorphous material generally follow an Arrhenius type temperature dependence:

$$D = D_0 \exp\left[-\frac{\Delta H}{k_B T}\right] \quad (5.6.1)$$

where D_0 is the diffusivity constant, and ΔH is the activation enthalpy for diffusion. Eq. 5.6.1 can be rewritten in terms of Gibbs free energy, which has pressure and volume dependence, where the activation volume for diffusion can be expressed as:

$$\Delta V = \left(\frac{\partial \Delta G}{\partial p}\right)_T \quad (5.6.2)$$

The diffusion mechanism for some amorphous metals has been described as collective motion of chains of atoms. This collective motion has a large activation

volume associated with it, and would therefore be highly dependent on pressure^{106,107}. For Fig. 4.12, it should be noted that strain effects are ignored as in

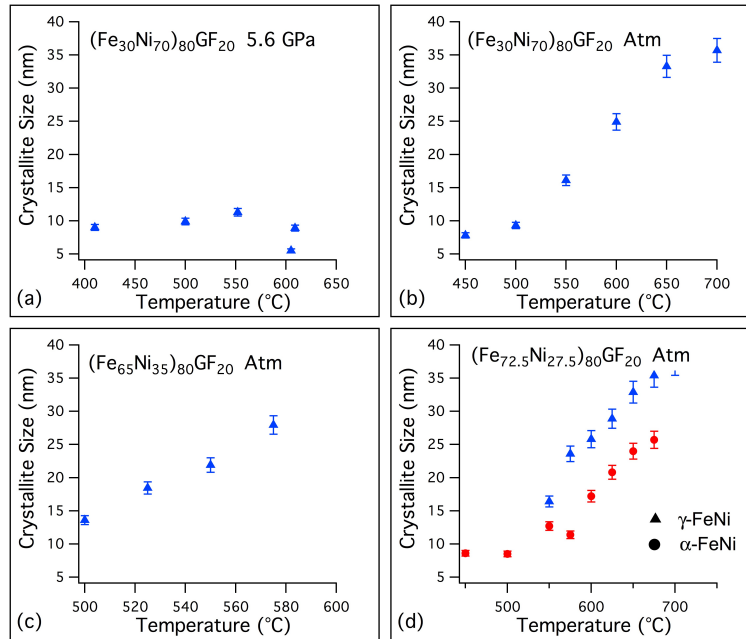


Figure 4.12: Crystallite size vs. temperature for $(\text{Fe}_{30}\text{Ni}_{70})_{80}\text{Nb}_4\text{Si}_2\text{B}_{14}$ at 5.6 GPa, $(\text{Fe}_{30}\text{Ni}_{70})_{80}\text{Nb}_4\text{Si}_2\text{B}_{14}$ at 1 atm, $(\text{Fe}_{65}\text{Ni}_{35})_{80}\text{Nb}_4\text{Si}_2\text{B}_{14}$ at 1 atm, and $(\text{Fe}_{72.5}\text{Ni}_{27.5})_{80}\text{Nb}_4\text{Si}_2\text{B}_{14}$ at 1 atm.

section 4.3, since the pressure applied is isotropic. Scherrer analysis could not be done for $(\text{Fe}_{75}\text{Ni}_{25})_{80}\text{Nb}_4\text{Si}_2\text{B}_{14}$, $(\text{Fe}_{30}\text{Ni}_{70})_{80}\text{Nb}_4\text{Si}_2\text{B}_{14}$ 1.5 GPa, and $(\text{Fe}_{65}\text{Ni}_{35})_{80}\text{Nb}_4\text{Si}_2\text{B}_{14}$ 4.9 GPa due to overlapping diffraction peaks.

At atmospheric pressure, $(\text{Fe}_{75}\text{Ni}_{25})_{80}\text{Nb}_4\text{Si}_2\text{B}_{14}$ develops α -FeNi first, followed by γ -FeNi. However, at 4.8 GPa, only γ -FeNi is determined to crystallize. This is because the close packed phase is favored at elevated pressures. The data from this section and chapter 4.5 can be compared to HTXRD performed on $(\text{Fe}_{70}\text{Ni}_{30})_{88}\text{Zr}_7\text{B}_4\text{Cu}_1$ ³⁴. In $(\text{Fe}_{70}\text{Ni}_{30})_{88}\text{Zr}_7\text{B}_4\text{Cu}_1$, α -FeNi crystallizes first, followed by an $\alpha \rightarrow \gamma$ transition. Upon cooling, the γ phase remains.

With the application of 5.6 GPa of pressure, $(\text{Fe}_{30}\text{Ni}_{70})_{80}\text{Nb}_4\text{Si}_2\text{B}_{14}$ underwent primary crystallization at room temperature as seen in Fig. 4.13. Unlabeled peaks in Fig. 4.13 cannot be uniquely identified. While primary crystallization temperature (T_{x1}) increased when pressure increased from atmospheric to 1.5 GPa, it decreased to at least room temperature as pressure increased further to 5.6 GPa. As mentioned before, the initial increase in T_{x1} can be attributed to a suppression of diffusion. The decrease in T_{x1} at higher pressures however can be explained by an increase in the change of Gibb's free energy between the amorphous and crystalline phase as pressure increases. The change in Gibb's free energy of crystallizing a

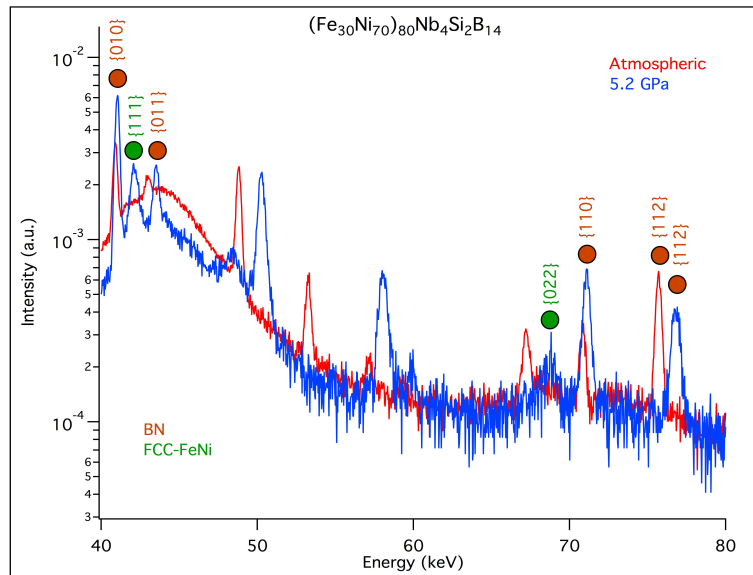


Figure 4.13: EDXRD of $(\text{Fe}_{30}\text{Ni}_{70})_{80}\text{Nb}_4\text{Si}_2\text{B}_{14}$ before and after pressurization showing pressure induced crystallization.

spherical particle in an amorphous matrix can be expressed as¹⁰⁸:

$$\Delta G(T,P) = \frac{1}{6}\pi d^3(\Delta G_v + \Delta G_s) + \pi d^2\gamma + P\Delta V \quad (4.6.3)$$

d is crystallite size, ΔG_v is the change in free energy for forming the crystal volume, ΔG_s is the elastic strain resulting from the change in volume, γ is the interfacial

strain energy, and ΔV the volume change from forming the crystal nucleus. As such, the volume change from the transformation becomes more important as the pressure increases, allowing crystallization despite of the suppression of diffusion.

vii. Atom Probe Tomography

Atom probe tomography (APT) is a powerful tool for examining the structure and partitioning of materials. This technique uses a needle shaped specimen that is cooled to cryogenic temperatures. A laser then ablates ions off from the sample, a

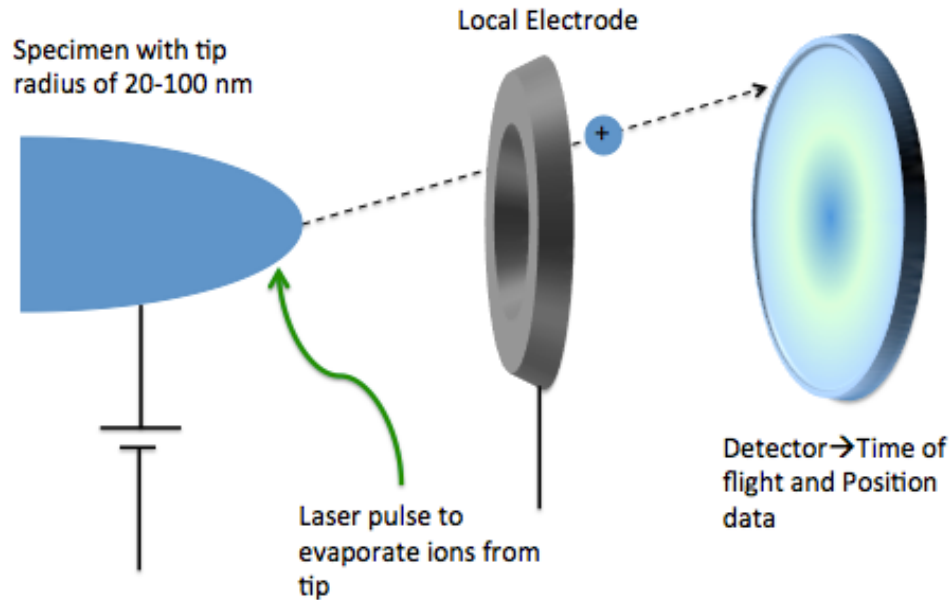


Figure 4.14: Schematic of atom probe tomography.

which are then accelerated by an electrode to a detector, which measures both time of flight and position. This technique is shown schematically in Fig. 4.14. APT produces 3-dimensional atom maps of a sample and can generate isosurfaces and 2D contour maps. Here, APT was done on $(\text{Fe}_{70}\text{Ni}_{30})_{80}\text{Nb}_4\text{Si}_2\text{B}_{14}$ alloys as-cast, annealed at 440 °C for 10 minutes, and strain-annealed at 440 °C and 300 MPa for 10 minutes.

2D surface contours of Fe, Ni, and B can be seen in Fig. 4.15. In the annealed and strain-annealed samples, clear partitioning between the B and the Fe-Ni can be seen, while none is seen in the as-cast sample. Composition estimates for the crystalline and residual amorphous phases can be determined from the minimum and maximum percentages for each element. The crystallites will correspond to the maximum of the Fe and Ni, while the amorphous phase will correspond to the maximum B and minimum Fe and Ni. For both the annealed and strain-annealed, the Fe:Ni ratio is approximately 1.7:1. The Fe to Ni ratio in the overall alloy as determined by APT is approximately 1.8:1, so the crystallites seem to maintain the Fe to Ni ratio of the parent alloy. It should be noted that the overall composition as determined by APT is different than the nominal composition of $(\text{Fe}_{70}\text{Ni}_{30})_{80}\text{Nb}_4\text{Si}_2\text{B}_{14}$. However, the nominal composition is very nearly correct as determined by Inductively Coupled Plasma-Optical Emission Spectrometry (ICP-OES) with an error of +/- 3% relative to the reported value. The amorphous phase as determined from Fe-Ni minima and B maximum has an Fe-Ni to B ratio of about 3.7, which is close to the 23:6 (~3.8) phase composition.

Within the annealed specimens, there appears to be some amount of Fe-Ni partitioning as well. This may have to do with the formation of γ -FeNi and α -FeNi as observed with TEM diffraction, where the α -FeNi would be more Fe-rich, and the γ -FeNi would be more Ni-rich.

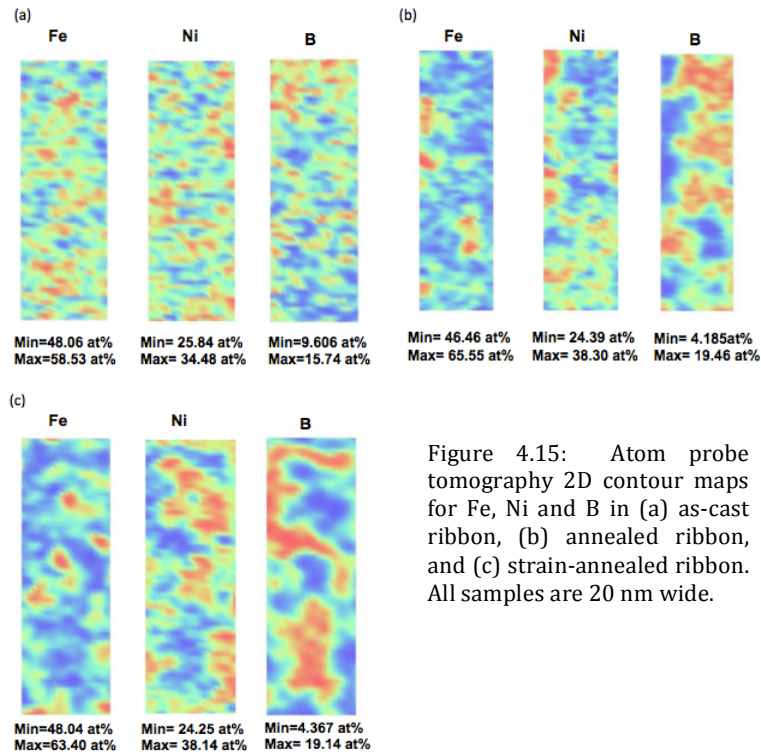


Figure 4.15: Atom probe tomography 2D contour maps for Fe, Ni and B in (a) as-cast ribbon, (b) annealed ribbon, and (c) strain-annealed ribbon. All samples are 20 nm wide.

viii. Conclusions

The fundamentals of XRD and ED-XRD with high pressure were presented. The thermodynamics and the importance of the magnetic phenomena on phase stability were discussed. It was shown that pressure suppresses crystal growth and the $\alpha \rightarrow \gamma$ -phase transformation temperature. In the Fe-Ni MANC system, most compositions show γ -FeNi as the primary crystal product, except Fe-rich compositions which show α -FeNi or both α -FeNi and γ -FeNi. All compositions show $(\text{FeNi})_{23}\text{B}_6$ as the secondary crystal product. Generally, pressure was found to raise the crystallization temperature. The exception being high pressure for $(\text{Fe}_{30}\text{Ni}_{70})_{80}\text{Nb}_4\text{Si}_2\text{B}_{14}$ which crystallized without any heating. TEM confirmed that the alloy of primary interest, $(\text{Fe}_{70}\text{Ni}_{30})_{80}\text{Nb}_4\text{Si}_2\text{B}_{14}$ contains both α -FeNi and γ -FeNi

after primary crystallization. APT demonstrates that the crystallites maintain the same Fe:Ni ratio as the parent phase, and that the residual amorphous phase is near the 23:6 phase composition. There is also clear partitioning of the B out of the Fe and Ni regions, and some Fe/Ni partitioning as well. This chapter has demonstrated hypothesis 4, which states that pressure can be used to refine the microstructure of Fe-Ni MANCs along with arguments regarding the 23:6 phase stability.

V. Magnetism and Magnetic Properties of Fe-Ni MANCs

i. Methods for Magnetization Measurement

One of the most basic techniques for measuring the magnetization of a sample is through vibrating sample magnetometry (VSM). VSM works off Faraday's law of induction. An electromagnet is used to create a DC magnetic field in the sample area, and the sample is attached to the bottom of a plastic or quartz tail, which is connected to a vibrating head. When the sample is magnetized, its vibrations induce a current in a set of pickup coils that are attached to the electromagnet pole pieces. The induced current is measured, and is proportional to the magnetization of the sample.

Another tool, especially useful for soft magnetic samples, is an AC permeameter (AMH), which has two experimental setups. First is a single strip tester, and the other is a toroidal sample tester, however they both work off the same principle. The magnetic sample is encased with primary and secondary windings, and an AC excitation of variable frequency is applied to the primary windings. This induces an AC magnetization in the magnetic material, which in turn induces a current in the secondary windings that is proportional to the magnetization.

ii. Magnetic Dipoles, Susceptibility, and Permeability

Magnetism arises from the spin and angular movement of electrons that create a magnetic dipole along the axis of rotation. Magnetization (M) is then simply the sum of all the dipoles over a unit volume. The behavior of the magnetization as a function of applied field, H , is captured by the *susceptibility*, χ , as:

$$M = \chi H \quad (5.2.1)$$

For paramagnetic materials, the susceptibility is on the order of 10^{-5} - 10^{-2} , and for diamagnetic materials, it is $\sim -10^{-5}$. For ferromagnetic materials, it is of course significantly higher. Permeability, μ , relates the induction to applied field as:

$$B = \mu H \quad (5.2.2)$$

where the permeability μ is the product of a materials relative permeability, μ_r , and the permeability of free space, μ_0 . Relative permeability is related to susceptibility by the simple relationship:

$$\mu_r = 1 + \chi \quad (5.2.3)$$

In soft magnetic materials, μ_r can attain very high values on the order of 10^6 such as in permalloys. With such high permeabilities, only small applied fields are required to saturate the sample.

iii. Mean Field Theory

Ferromagnets are defined as having spontaneous magnetizations even without an applied field. One of the first theories as to why this was the case was proposed by Weiss. Weiss said there is an internal field which is proportional to the magnetization. This magnetization is described by a Brillouin function:

$$B_j(x) = \frac{2j+1}{2j} \coth\left(\frac{2j+1}{2j}x\right) - \frac{1}{2j} \coth\left(\frac{x}{2j}\right) \quad (5.3.1)$$

where x is given by:

$$x = \frac{\mu M}{k_B T} \quad (5.3.2)$$

and j is the spin-orbit coupling. Brillouin fits for Fe-Nd-B samples can be seen in Fig. 5.1 with $j=1/2$ for which the Brillouin function collapses to a hyperbolic tangent function. A Brillouin fit can be used to estimate the percentage of a particular phase in a sample, and can be compared to a mass balance analysis. The Brillouin function was fit to the window of data below the temperature where crystallization occurs, as such, the only phase contributing to the $M(T)$ curve is α -Fe. The mass percentage of α -Fe in the sample is then calculated by dividing the magnetization due to the presence of α -Fe by the specific magnetization of α -Fe, 220 emu/g. For NB1, this yields α -Fe percentages of 5.5% and 32.3% for NB1 as-cast and crystallized respectively. For NB3, this yields 9.1% and 30.0% for as-cast and crystallized respectively. These phase percentage balances can be compared to similar calculations based on atomic percentages. If all the Nd is assumed to form the 2:14:1 phase, and any remaining B forms Fe_2B , then the remaining Fe is the percentage of α -Fe in the sample. For composition NB1, this yields 29.2% α -Fe, and 43.7% α -Fe in NB3. NB1 is quite close to the value from the magnetization data, NB3 is not. This is probably due to the presence of other phases in the sample. The NB3 composition, to the right of the 2:14:1 line compound, is in a phase field in which a T2 phase, described as incommensurate modulated intergrowths of borides into Fe may also have larger T_c making analysis more complicated. Lastly, the difference in T_c for α -Fe in the heating and cooling curves is attributed to the difference in heating and cooling rates.

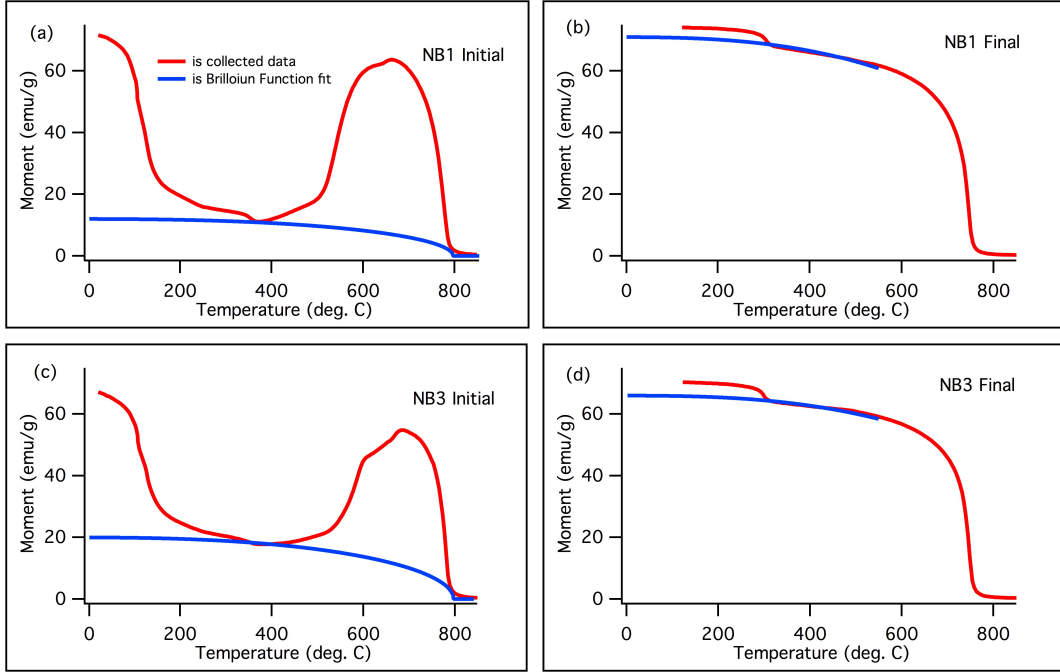


Figure 5.1: $M(T)$ for samples of nominal composition (a) $\text{Fe}_{87.4}\text{Nd}_{8.2}\text{B}_{4.4}$ (NB1) and (c) $\text{Fe}_{89.1}\text{Nd}_{5.9}\text{B}_{5.0}$ (NB3) showing transitions associated with the crystallization of an amorphous phase at 500 °C and a Curie transition at 770 °C in red and Brillouin function fits in blue. (b) and (d) are M vs. T cooling curves for NB1 and NB3 respectively. 2:14:1 phase T_c can be seen at 300 °C.

iv. Heisenberg Exchange

The Weiss mean field theory raises the question of what the origin of this internal field is. The answer is electron exchange interactions. Exchange interactions arise from the two principles of Coulombic interactions and the Pauli exchange principle⁴⁵. By minimizing the interaction energy between neighboring electrons, the Heisenberg Hamiltonian is written:

$$H = -2J_{ex} \sum_i S_i \cdot S_j \quad (5.4.1)$$

with S being an electron spin state. When J_{ex} is positive, neighboring electrons align parallel, while if J_{ex} is negative, neighboring electrons align antiparallel. By combining the mean field theory and the Heisenberg exchange energy, and

assuming only nearest neighbors have significant interactions, then the Curie temperature can be expressed as:

$$T_C = \frac{2ZJ_{ex} S(S+1)}{3k_B} \quad (5.4.2)$$

with Z being the number of atomic neighbors. The magnitude of the exchange interaction determines how well the dipole moments of neighboring electrons are aligned. The stronger the exchange, the more aligned they will be. Temperature acts to misalign the dipole moments in order to increase the entropy of the system. Once the temperature effects overwhelms the exchange interaction, the material become paramagnetic instead of ferromagnetic. This temperature is defined as the Curie temperature.

v. Bethe-Slater Curve and Distributed Exchange

The Bethe-Slater curve grew out of questioning why only Fe, Co, and Ni among the 3d transition metals exhibit ferromagnetism. Slater had previously calculated the ratio of the interatomic spacing to the diameter of the d-electron shell^{109,110}, which Bethe then used to plot the exchange energy against²¹. The resulting Bethe-Slater curve resembles an inverted potential well diagram as seen in Fig. 5.2. The zero crossing along the x-axis is taken to be at 1.5, and negative exchange implies antiferromagnetic interactions. With the Bethe-Slater curve, it can be inferred that the overall exchange interactions between atoms depend on atomic spacing, such that were γ -Fe stressed enough, the interaction could become positive and display ferromagnetism instead of antiferromagnetism.

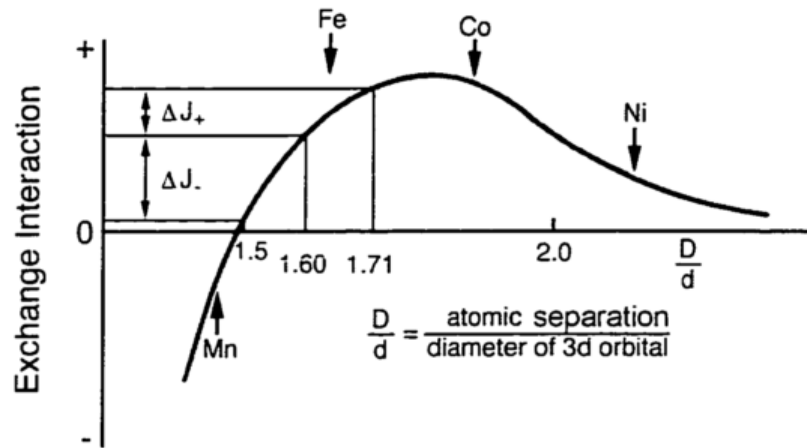


Figure 5.2: The Bethe-Slater curve showing the relative positions of Mn, Fe, Co, and Ni.

vi. Domains and Domain Walls

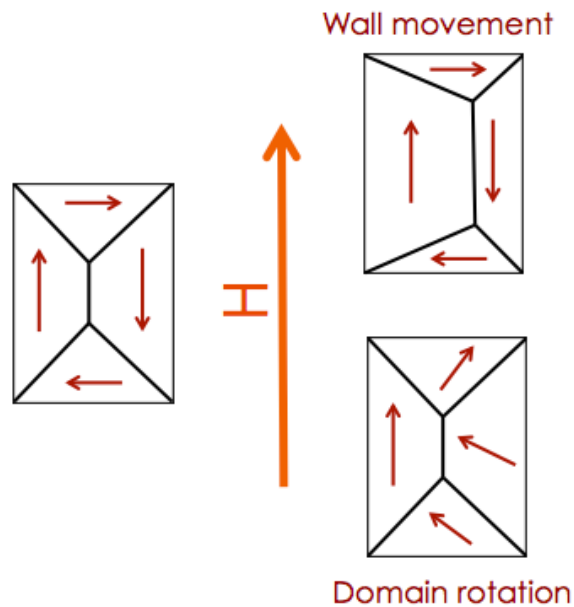


Figure 5.3: Sketch of demagnetized sample becoming magnetized via wall motion and domain rotation mechanisms.

In the absence of a magnetic field, soft ferromagnetic materials will not exhibit a magnetization even though local magnetic moments are aligned. This is due to the existence of magnetic domains. Within a domain, all magnetic dipole are

aligned, but a material will comprise many domains such that the overall magnetization is zero. The boundary between domains is called a domain wall. In domain walls, the directions of the dipoles gradually change from the direction of one neighboring domain to that of the other. When a field is applied, the domains will all become aligned through one of two processes. The first option is by domain wall movement. The domain that is most aligned with the applied field will grow at the expense of its neighbors by the movement of the domain walls. The second option is by domain rotation. Here, all the domains rotate until they are aligned with the applied field. These mechanisms are sketched in Fig. 5.3.

vii. Magnetostriction and Magnetic Anisotropy

Magnetostriction (λ) refers to a change in dimension or volume of a magnetic material with the application of a magnetic field. Magnetocrystalline anisotropy refers to the fact that different materials have different easy or hard directions for the magnetization to align with, such that it is energetically favorable for the magnetization to lie along the easy direction. For example, the easy direction for magnetization in iron is the $\langle 100 \rangle$ family, while it is the $\langle 111 \rangle$ family for nickel, and the $[0001]$ direction for Co. For cubic materials, such as Fe and Ni, the magnetocrystalline anisotropy energy density can be expressed as:

$$E_k = K_1(\alpha_1^2\alpha_2^2 + \alpha_2^2\alpha_3^2 + \alpha_3^2\alpha_1^2) + K_2(\alpha_1^2\alpha_2^2\alpha_3^2) \quad (5.7.1)$$

where K_1 and K_2 are materials specific anisotropy constants, and α are direction cosines.

It has traditionally been considered that near zero magnetostriction and anisotropy were required for high permeability¹¹¹. However, it was discovered that

reducing the crystal size to below the size for exchange coupling, the effective magnetocrystalline anisotropy is zero due to the random distribution of crystal axes⁴³. This argument however does not apply to magnetostriction. Since the magnetizations of the crystals are aligned regardless of easy magnetization direction, the strains do not cancel out. However, nanocomposites provide us with unique ways to achieve zero magnetostriction. It is not necessary for the crystals to have zero magnetostriction, since it may be possible to achieve an opposite magnetostriction in the amorphous phase such that the crystallites and amorphous phase cancel each other out.

In γ -FeNi alloys, significant work was done on alloys $\sim 80\%$ Ni due to zero crossings of the anisotropy energy (K), and λ_{111} and λ_{100} ⁴². Data for the γ -phase however is not available for much less than 40% Ni due the stability of the α phase with increasing Fe. The plots for K and λ_{111} and λ_{100} provided by Harada⁴² suggest that these values would again be at or near zero at 30% Ni if extrapolated. Ishio¹¹¹ observed that the saturation magnetostriction, λ_s is approximately zero near the fcc-bcc transition. However, it is not because both λ_{111} and λ_{100} are equal to zero, but rather λ_{100} is less than, and λ_{111} is more than zero. Both λ_{111} and λ_{100} are very sensitive to Fe composition near the fcc-bcc boundary. In addition, the anisotropy energy at 40% Ni is positive, but with a negative curvature such that it may be closer to zero at 30% Ni.

viii. Magnetization and T_C trends in Fe-Ni MANCs

In order to screen alloys of interest, it is critical to evaluate the saturation induction and Curie temperatures of the alloys in order to determine which are the most promising for specific applications. Magnetization and Curie temperature (T_C) data for as-cast ribbons are shown in Fig. 5.4 along with T_C of γ -FeNi. As expected, the saturation magnetization decreases with increasing Ni content. Comparing T_C of

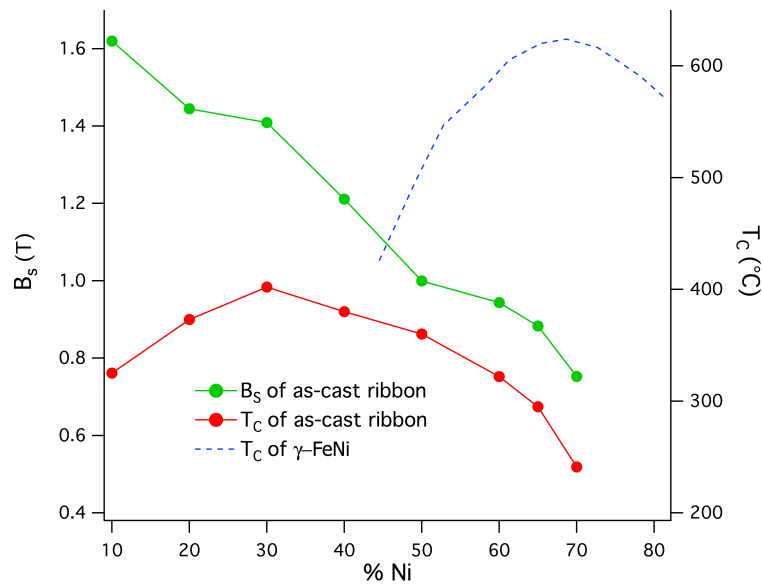


Figure 5.4: Saturation induction and Curie temperature for as-cast ribbon. Curie temperature for γ -FeNi is in blue.

γ -FeNi to the T_C of the amorphous phase shows a shift of the peak T_C from 70% Ni to 30%¹³. This can be understood qualitatively with respect to the Bethe-Slater curve^{21,110}. In the amorphous phase, there is a distribution of atomic spacings which contribute to a distribution of exchange energies⁸⁸. Fe-Fe interactions in the γ phase are negative, and extremely sensitive to atomic spacing while Ni-Ni and Fe-Ni interactions are positive and not as sensitive. It is for this reason that the peak in Curie temperature lies on the Ni-rich side of the binary phase diagram for the γ phase. Since Fe atoms bond distances cannot get much smaller than observed in

close-packed structures and the amorphous phase typically has ~2% free volume, the distribution will be weighted to larger spacings, which can lead to some positive Fe-Fe exchange interactions. It is therefore expected that the peak in T_C will shift to higher Fe contents with respect to γ -FeNi. The overall decrease in T_C can be explained by the fact that the alloy has a significant number of non-magnetic atoms that do not contribute to the overall exchange energy. Also, the total exchange energy may be lower due to the averaging of positive and negative exchange interactions among the Fe-Fe interactions.

Since the exchange interactions between atoms depends on the interatomic spacing, it follows that the interactions depend on applied pressure as well. If one could apply large enough pressures while making magnetic measurements, a Bethe-Slater like curve could be mapped for elements and alloys.

ix. Low Temperature Magnetic Phenomena

For a ferromagnetic material, as temperature decreases, M_s increases due to the decrease in thermal entropy, which allows more spins to be better aligned along the direction of magnetization. This was mathematically described earlier by the Mean Field Theory. Figure 5.5 depicts M vs. T for as-cast and annealed $(\text{Fe}_{70}\text{Ni}_{30})_{80}\text{Nb}_4\text{Si}_2\text{B}_{14}$. The cooling curves for both samples have a maximum M before 5 K. Furthermore, the heating curve does not follow the same path as the cooling curve. This hysteresis may be due to a ferromagnetic \rightarrow asperomagnetic transition, below which the spins become frozen in such a way that they are canted from one another, decreasing the overall magnetization⁴⁵. This phase then remains metastable upon heating causing the hysteresis. Alternatively, this phenomenon

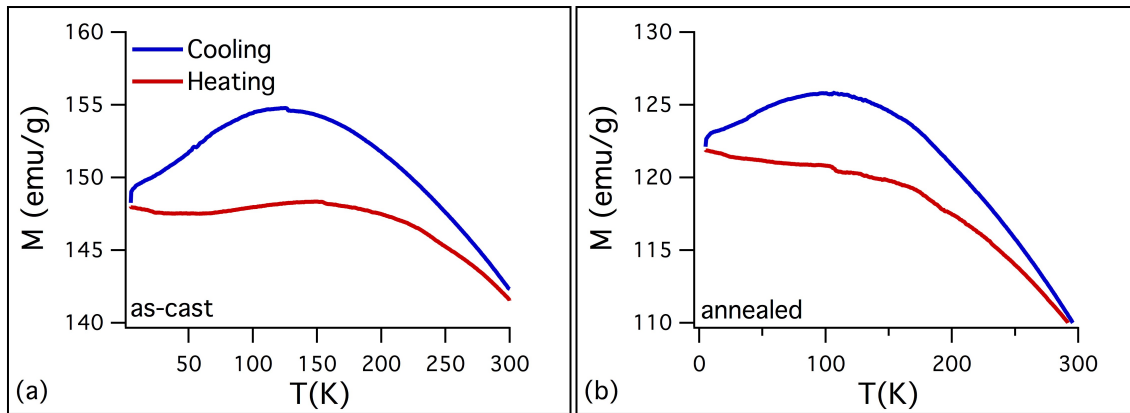


Figure 5.5: Cooling and heating M vs. T curves for (a) as-cast and (b) annealed $(\text{Fe}_{70}\text{Ni}_{30})_{80}\text{Nb}_4\text{Si}_2\text{B}_{14}$

may be attributed to the distributed exchange interaction in the amorphous phase. As temperature is decreased, atomic spacing decreases as well. The Fe-Fe interactions that are on the ferromagnetic-antiferromagnetic border may be pushed over to the antiferromagnetic side. Antiferromagnetic clusters can then remain metastable upon heating until higher temperatures.

x. Strain-Annealing effects on B-H Loops

Magnetic hysteresis loops are shown in Fig. 5.6. Most of the hysteresis loops become more square when strain-annealed, yielding higher permeabilities. The relative permeability, μ_r , of annealed $(\text{Fe}_{70}\text{Ni}_{30})_{80}\text{Nb}_4\text{Si}_2\text{B}_{14}$ increases from 4000 to 16000 when strain-annealed. This compares well with silicon steels, with typical relative permeabilities ranging from 1500 to 4000¹¹²⁻¹¹⁴, for high permeability applications. However, the $(\text{Fe}_{30}\text{Ni}_{70})_{80}\text{Nb}_4\text{Si}_2\text{B}_{14}$ B-H loop flattens when strain-annealed with the μ_r decreasing from 290 to 40. This is consistent with a change in the sign of the magnetostriction, λ , of the resultant Fe-Ni crystallites from annealing which has been demonstrated as a primary metric for the sign and magnitude of the strain induced anisotropy associated with residual stresses present after partial

devitrification¹¹⁵. The reduction of permeability is compounded by the crystallization of a magnetically hard phase, which would preclude the use of such alloys in transformer or motor applications. When the alloy is more Fe-rich than the permalloy composition, the magnetostriction is positive, resulting in square loops. When the alloy is more Ni-rich than permalloy, the magnetostriction is negative

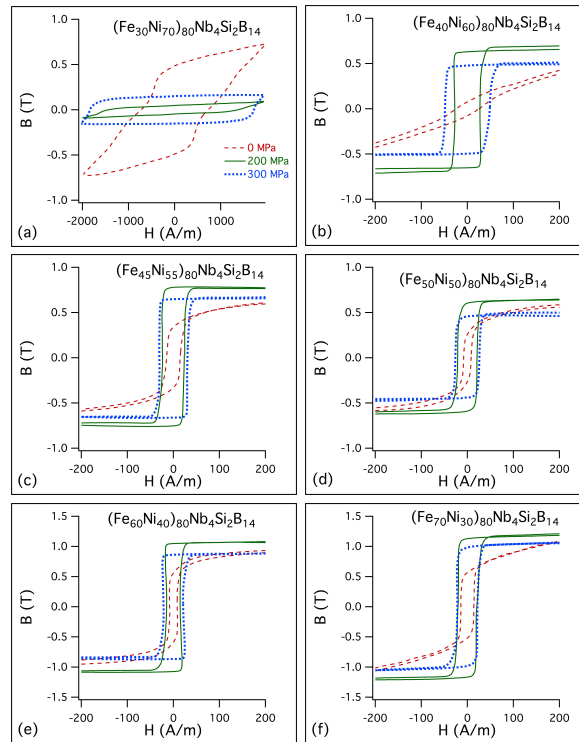


Figure 5.6: B vs. H loops for annealed and strain-annealed alloys. (a) $(\text{Fe}_{30}\text{Ni}_{70})_{80}\text{Nb}_4\text{Si}_2\text{B}_{14}$, (b) $(\text{Fe}_{40}\text{Ni}_{60})_{80}\text{Nb}_4\text{Si}_2\text{B}_{14}$, (c) $(\text{Fe}_{45}\text{Ni}_{55})_{80}\text{Nb}_4\text{Si}_2\text{B}_{14}$, (d) $(\text{Fe}_{50}\text{Ni}_{50})_{80}\text{Nb}_4\text{Si}_2\text{B}_{14}$, (e) $(\text{Fe}_{60}\text{Ni}_{40})_{80}\text{Nb}_4\text{Si}_2\text{B}_{14}$, (f) $(\text{Fe}_{70}\text{Ni}_{30})_{80}\text{Nb}_4\text{Si}_2\text{B}_{14}$.

yielding sheared loops⁴². The coercivity of the $(\text{Fe}_{30}\text{Ni}_{70})_{80}\text{Nb}_4\text{Si}_2\text{B}_{14}$ is also significantly higher due to the on-set of secondary crystallization at much lower annealing temperatures which produces a magnetic hardening by depleting the amorphous matrix and allowing crystal growth¹¹⁶. The coercivity of the major B-H loop also increases for the other alloys with strain annealing, although this effect becomes less significant in the more Fe-rich alloys. In addition, the difference in B_s

between treatments for all alloys except $(\text{Fe}_{30}\text{Ni}_{70})_{80}\text{Nb}_4\text{Si}_2\text{B}_{14}$ is due to uncertainty in the cross-sectional areas of the samples.

xi. Density of States and the Electronic Structure

Before we examine resistivity data in Fe-Ni based MANCs, we will provide background on the electronic structure of alloys, the density of states, and how these ideas provide the basis for understanding resistivity in both crystalline and amorphous alloys.

The density of states (DOS) denotes the number of electron states at a given energy level in a material. The particular energy that has the most energetic filled states is called the **Fermi Energy**, ε_F . It follows that integrating the DOS over energy from $-\infty$ up to ε_F yields the number of electrons in an atom. This is represented mathematically as:

$$N = \int_{-\infty}^{\varepsilon_F} g(\varepsilon) d\varepsilon \quad (5.10.1)$$

with N the number of electrons, and g the DOS. The DOS can be split into two distinct DOS's by considering spin up and spin down electrons separately. This is referred to as the spin-split DOS.

$$N^\uparrow = \int_{-\infty}^{\varepsilon_F} g^\uparrow(\varepsilon) d\varepsilon \quad (5.10.2)$$

$$N^\downarrow = \int_{-\infty}^{\varepsilon_F} g^\downarrow(\varepsilon) d\varepsilon \quad (5.10.3)$$

Combing eqs. 5.10.1-3 yields:

$$N = \int_{-\infty}^{\varepsilon_F} (g^\uparrow(\varepsilon) + g^\downarrow(\varepsilon)) d\varepsilon \quad (5.10.4)$$

Another important aspect of DOS to keep in mind is that s, p, and d-electrons have different band structures. Generally, s-bands have simple structures, and the DOS for most energy levels is lower than for the d-band, which also tends to have a far more complicated shape. For transition metal elements, the d-band DOS at ϵ_F is significantly greater than the s-band DOS at ϵ_F ¹¹⁷. Mott assumed that conduction is mostly carried out by s-electrons due to their low effective mass, as opposed to d-electrons. However, various interactions can scatter s-electrons into vacant d-states, and this scattering probability is proportional to the DOS where the electrons are scattered:

$$P_{kk'} \propto g(\epsilon_F) \quad (5.10.5)$$

Once an electron scatters into the d-band it can no longer contribute significantly to conductivity due to its high effective mass¹¹⁷. The scattering rate of electrons can be approximated as a relaxation time averaged over the Fermi surface, τ ¹¹⁸. The relaxation time allows us to express the Drude^{119,120} formula for resistivity:

$$\rho = \frac{m}{ne^2\tau} = \frac{mv}{ne^2\Lambda} \quad (5.10.6)$$

where m is the electron mass, e is the electron charge, n is the number of electrons per unit volume, v is electron velocity, and Λ is the electron mean free path^{118,121}.

The DOS and local density of states (LDOS) can be calculated using a spin-polarized relativistic Korringa-Kohn-Rostoker (SPRKKR) Green's method. This method is utilized by the package written by H. Ebert¹²².

xii. Resistivity

As already discussed, one of the advantages of MANCs over Si-steels is their higher resistivities which give lower eddy current losses. MANC resistivities however are generally lower than their parent amorphous alloy. This behavior has been discussed recently in terms of a multiphase model^{14,123}. This multiphase model considers an equivalent circuit where series and parallel paths are modeled through the amorphous, crystalline, and growth inhibitor rich shell phases. In nanocomposite systems, it is expected that the shell phase has the highest resistivity, followed by the amorphous phase, and then the crystalline phase having the lowest resistivity. Due to the structure of the nanocomposite, for the current to flow through the low resistivity crystalline phase, it will have to first flow through the thin and high resistivity shell phase. The total resistivity can be expressed as:

$$\frac{1}{\rho_{eq}} N^{1/3} = \frac{1}{\rho_{am}^{\parallel}} + \left(\left(\frac{1}{\rho_{sh}^{\perp} + \rho_{xtl}^{\perp}} + \frac{1}{\rho_{sh}^{\parallel}} \right)^{-1} + \rho_{am}^{\perp} \right)^{-1} \quad (5.12.1)$$

where N is the volume fraction of crystallites, and \perp and \parallel denote series and parallel paths respectively. This is drawn schematically in Fig. 5.7.

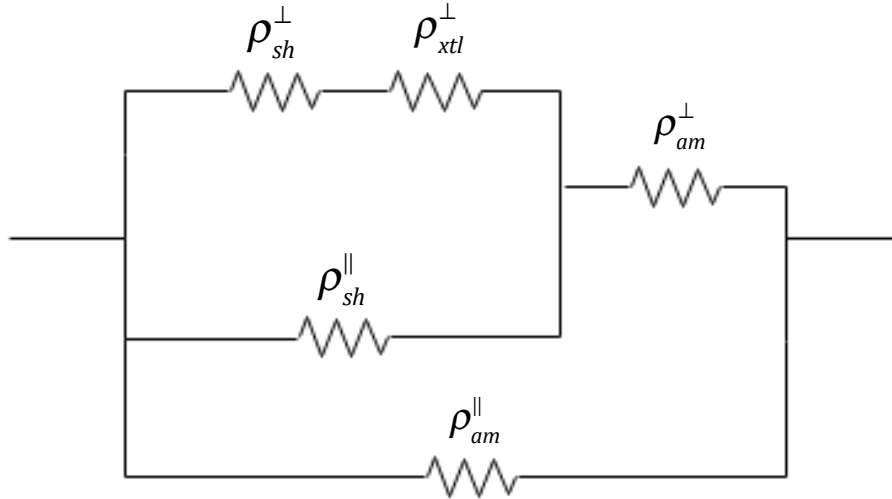


Figure 5.7: Circuit diagram depicting the 3-phase resistivity model.

From a device standpoint, the material laminates used must also be electrically insulated from each other, otherwise the effective thickness increases as does eddy current losses. Because of this, nonconductive filler is used which lowers the density of magnetic material and adds weight to the device. As such, it would be ideal to have a material with a thin oxide layer that can electrically insulate the laminates without the need of filler. In Table V.I, the resistivity for $(\text{Fe}_{70}\text{Ni}_{30})_{80}\text{Nb}_4\text{Si}_2\text{B}_{14}$ as-cast, annealed, and strain-annealed are shown. Both annealed ribbons were annealed at 440 °C. As shown, the resistivity for the as-cast sample is highest, while the annealed and strain-annealed samples have nearly identical resistivity.

Table V.I: Resistivity for $(\text{Fe}_{70}\text{Ni}_{30})_{80}\text{Nb}_4\text{Si}_2\text{B}_{14}$ for as-cast, annealed, and strain-annealed samples.

Alloy	$(\text{Fe}_{70}\text{Ni}_{30})_{80}\text{Nb}_4\text{Si}_2\text{B}_{14}$		
Heat Treatment	As-cast	440 °C	440 °C, 300 MPa
Resistivity ($\mu\Omega\text{-cm}$)	153	135	139

These results warrant future examination of resistivity measured across a stack of annealed material, or alternatively a measure of surface resistivity for as-cast and oxidized samples.

xiii. Virtual Bound States (VBS) and Resistivity

VBS have recently been demonstrated to enhance the resistivity and alter the magnetic properties of Co-based nanocomposites¹¹⁵. Generally, VBS theory describes the electronic effects from an impurity atom embedded in a crystal. Typically, the impurity atom has a less steep potential well once embedded in the

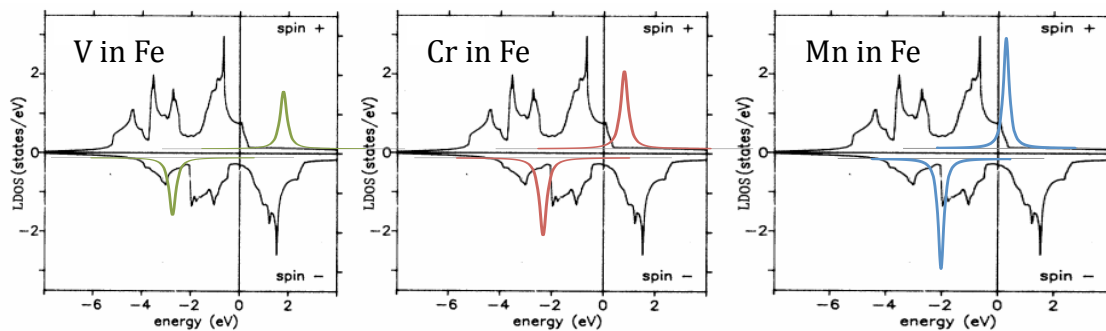


Figure 5.8: Schematic of 3d transition metal VBS in Fe matrix adapted from Drittler et al.¹²⁵

crystal, causing outer electrons to join the conduction band. The remaining ion provides a scattering potential for nearby conduction electrons whose magnitude depends on the electron wavefunction and energy. Practically, this causes nearby electrons to slow down and produce a screening cloud.¹²⁴ It is this screening cloud that is called a virtual bound state. More specifically, in this work, a VBS is produced when a dilute transition element (TE) d-electron moves through the Fermi energy of a parent alloy comprised of late transition metals (TL), and is added to empty spin states²⁶. Each TE atom will make contribution to the empty TL 3d states.

VBS additions generate new states on the local density of states (LDOS.) The system in this work consists primary of Fe and Ni. Fortunately, it is expected that TE elements behave similarly in Fe and Ni. For the transitions metals furthest to the

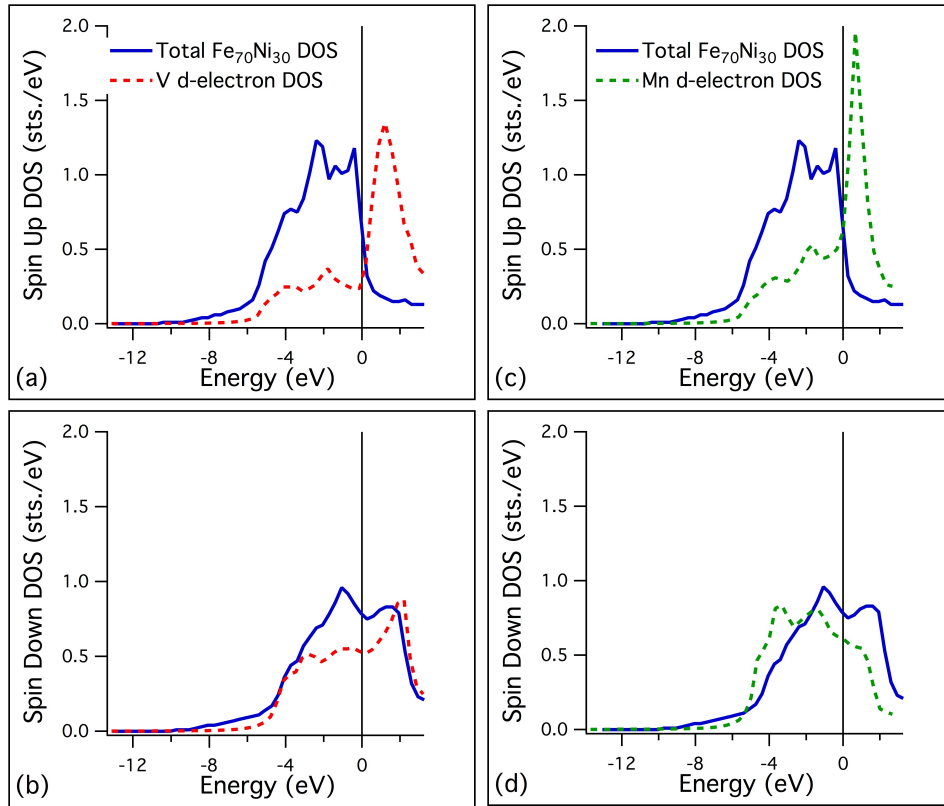


Figure 5.9: Calculated DOS for fcc $\text{Fe}_{70}\text{Ni}_{30}$ with impurity d-electron LDOS.

left in the periodic table, resonant LDOS peaks are created above the Fermi energy. As we move to the right along the row of the periodic table, the resonant LDOS peak moves closer to the Fermi energy, and gets sharper. Eventually, once the peak reaches the Fermi energy, the virtual state falls into the states of the host metal, and the LDOS becomes nearly indistinguishable from the host DOS. A schematic of transition metal VBS in Fe can be seen in Fig. 5.8¹²⁵.

The SPRKKR method mentioned earlier can calculate DOS and LDOS for ordered or disordered crystalline systems. Fig. 5.9 illustrates calculated spin-

polarized density of states for an fcc Fe₇₀Ni₃₀ crystal with the Fermi energy set to zero. Overlaid the host Fe-Ni DOS is the local V and Mn DOS. It can be seen that these results agree with the schematic in Fig. 5.6, showing the V resonance peak as shorter, broader, and further from the Fermi energy than the Mn resonance peak.

Resistivity for V, Cr, Nb, and Mo containing alloys can be seen in Fig. 5.10. From the V series, it can be seen that resistivity initially increases with increasing V. From 1% V to 3.5% V, the resistivity remains constant within the error of the measurement. Above 3.5%, resistivity increases again, however, as discussed

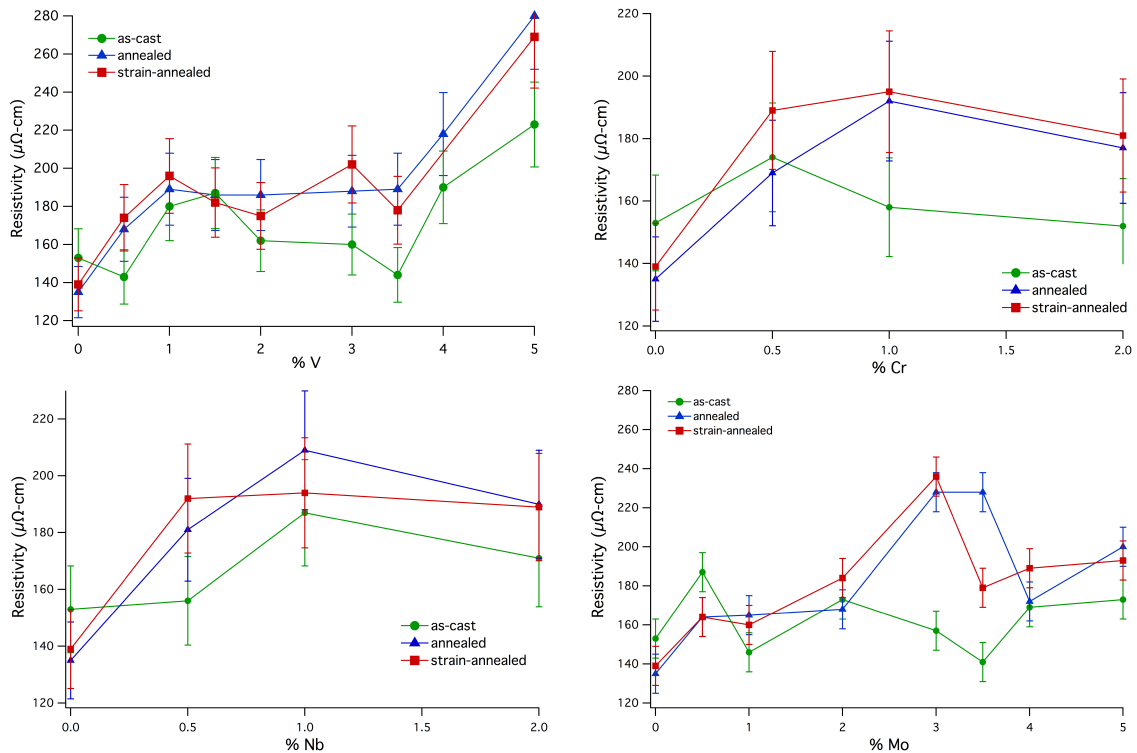


Figure 5.10: Resistivity of V, Cr, Nb, and Mo series.

below, this increase is accompanied by a significant worsening of magnetic properties. Analyzing the V series through a three phase resistivity model¹⁴, it is likely that the V is initially concentrated in the dispersed crystalline phase, which causes the initial resistivity rise. Once the crystal resistivity is on par or above the

resistivity of the shell and amorphous phase, the resistivity remains constant as it is controlled by the amorphous phase and shell structure. The final rise in resistivity can be tied to the crystalline phase saturating with V, causing additional V to reside in the amorphous phase, raising the resistivity further.

In the Mo series the resistivity increases with increasing Mo until 3% Mo, and then decreases. However, the as-cast Mo alloys have nearly constant resistivity. Since Mo is a large atom, it is expected to have low solubility in crystalline Fe-Ni, and will therefore accumulate in the shell structure around the crystals after annealing.

Resistivity for the Cr and Nb series follow the same trend as the V series with increasing resistivity up to 1% V, and then decreasing after that. Furthermore, the values of resistivity between the V and Cr series are almost identical.

xiv. Effects of VBS Elements on Magnetic properties

All VBS alloys were annealed at 440 °C and strain-annealed at 440 °C and 300 MPa. BH loops were then collected on the alloys from which B_s , H_c , and permeability can be determined. It should be noted that previous permeability measurements of the base alloy yielded μ_r of 4000 and 16000 for annealed and strain-annealed

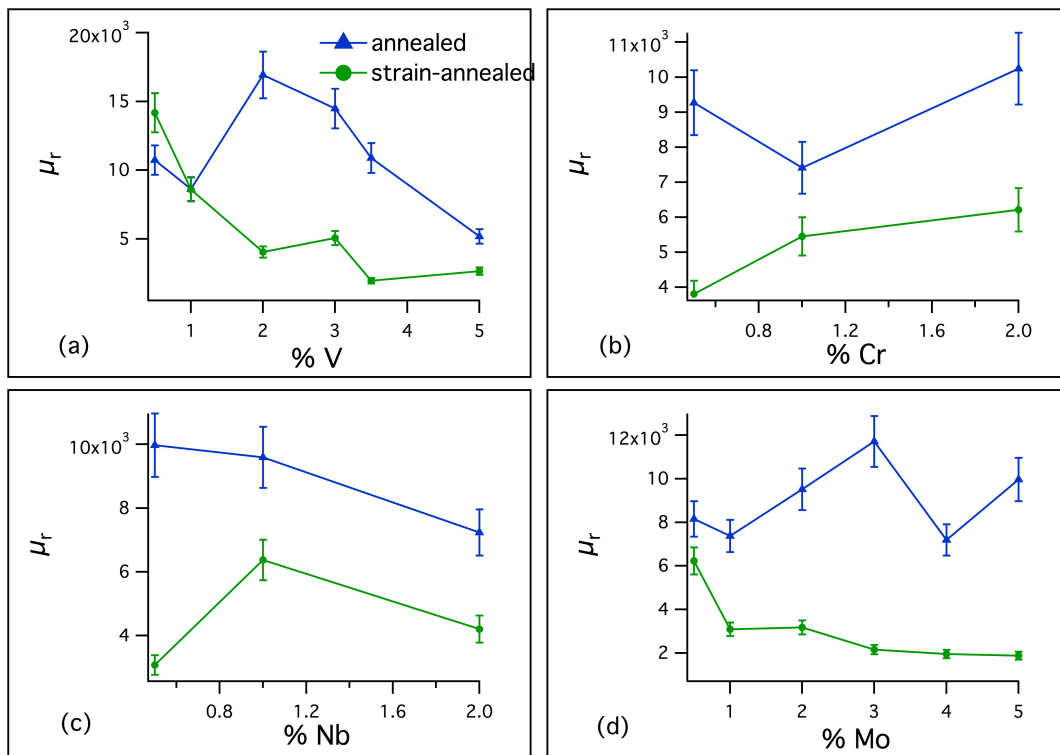


Figure 5.11: Permeability of annealed and strain-annealed V and Mo alloys.

treatments respectively¹²⁶. As is clear from Fig. 5.11, the addition of VBS elements quickly changes this trend of increasing μ_r with strain-annealing. As discussed above, this is likely due to changing the magnetostriction coefficient, λ , which has been demonstrated as a primary metric for the sign and magnitude of the strain-induced anisotropy associated with residual stresses present after primary crystallization¹¹⁵. Increasing permeability would be indicative of parallel (along the

ribbon direction) induced anisotropy, while decreasing permeability is indicative of

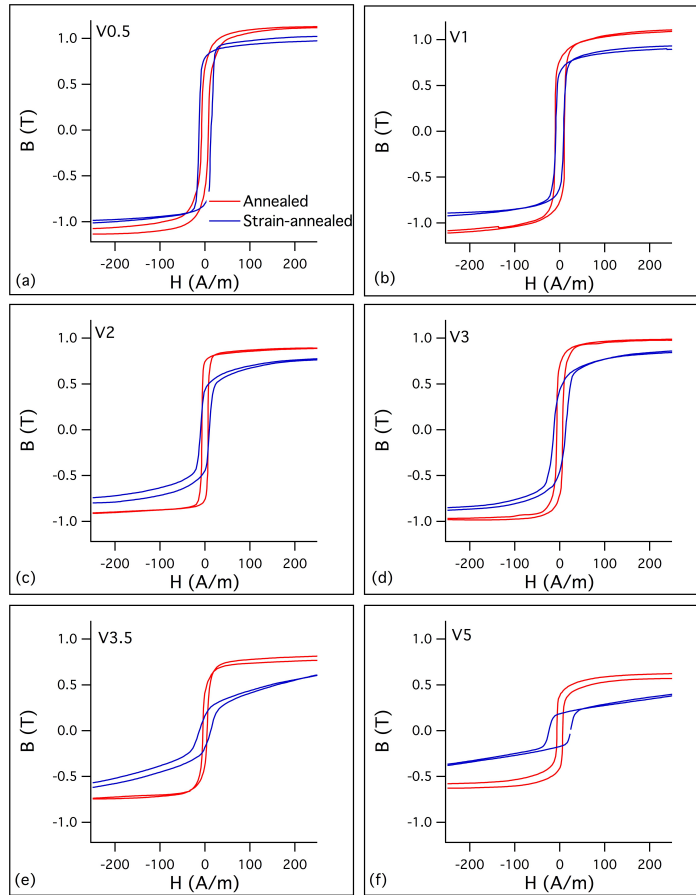


Figure 5.12: BH loops for the vanadium VBS series.

transverse induced anisotropy.

BH loops for the V and Mo series can be seen in Fig. 5.12 and 5.13 respectively. In the V series, as %V increases, the saturation induction, B_s , reduces down to 0.5 T at 5% V, from an induction greater than 1 T in the base alloy. In addition, there is a significant increase in the coercivity at 5% V. In the Mo series, B_s decreases from 3% Mo to 5% Mo to a minimum value of 0.6 T. However, there is no appreciable change in the coercivity.

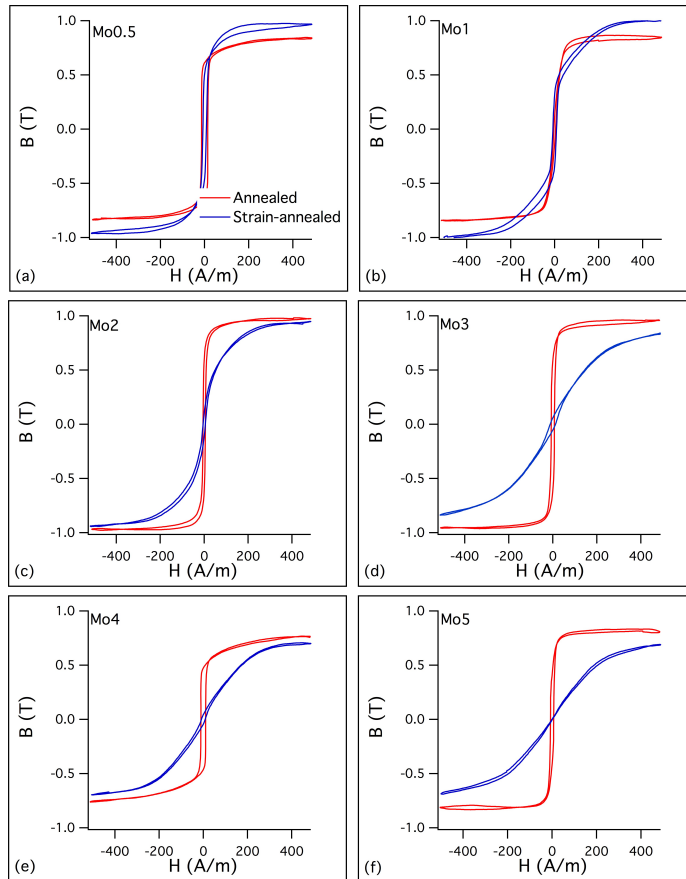


Figure 5.13: BH loops for the molybdenum VBS series.

xv. Introduction to FORC and the Preisach Distribution

First order reversal curves (FORCs) are a unique method to probe the

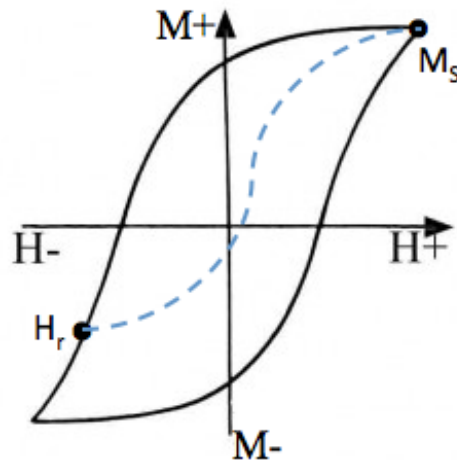


Figure 5.14: Schematic FORC curve within a BH loop.

magnetic behavior and interactions between phases in magnetic materials. The technique has been used extensively in paleo- and geo-magnetism¹²⁷. FORCs are obtained by magnetizing a sample to saturation with a field H_s , and then decreasing the applied field to a value H_r , called the reversal field. From the reversal field, the sample is saturated again. This curve going from H_r to H_s is a FORC, as seen in Fig. 5.10. This is then repeated for many values of H_r . This technique can be viewed as a “mapping” of the interior of a standard BH loop. From these curves, a Preisach distribution is generated and is defined as the second partial derivative of the magnetization with respect to the reversal field and the applied field:

$$\rho(H_r, H) = -\frac{1}{2} \frac{\partial^2 M(H_r, H)}{\partial H_r \partial H}$$

The factor of $\frac{1}{2}$ arises from the fact that switching the magnetization from $-M_s$ to $+M_s$ has a magnitude of $2M_s$ ¹²⁷.

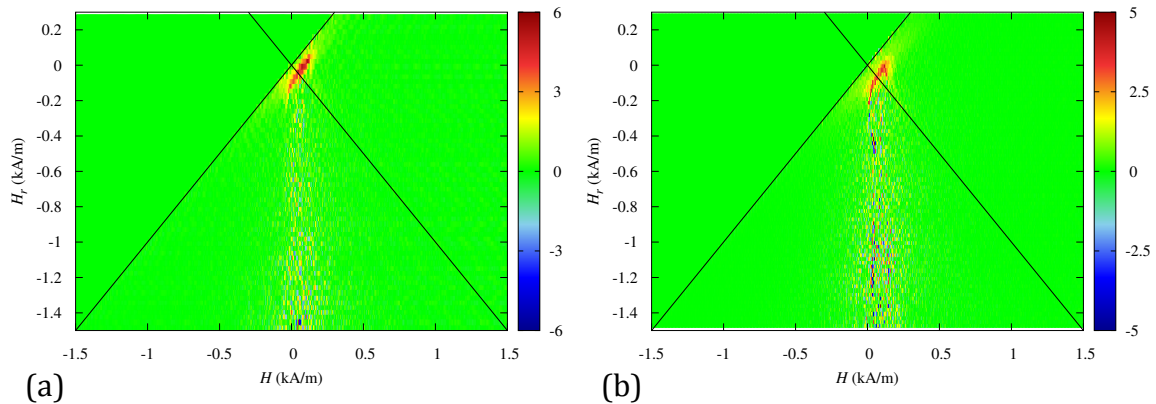


Figure 5.15: Preisach distributions for (a) as-cast $(\text{Fe}_{70}\text{Ni}_{30})_{80}\text{Nb}_4\text{Si}_2\text{B}_{14}$ and (b) strain-annealed $(\text{Fe}_{70}\text{Ni}_{30})_{80}\text{Nb}_4\text{Si}_2\text{B}_{14}$

AC FORC curves were carried out on strain-annealed $(\text{Fe}_{70}\text{Ni}_{30})_{80}\text{Nb}_4\text{Si}_2\text{B}_{14}$ by the group of Montserrat Rivas at the University of Oviedo. The Preisach distributions can be seen in Fig. 5.15. Unfortunately, due to the small width of the

ribbons used, the data is very noisy and no conclusions can be made. Annealed wide ribbon has been sent and the data is pending at the time of this writing.

xvi. Conclusions

Fundamentals of magnetism and magnetic measurement techniques were reviewed. The Bethe-Slater curve was introduced along with the idea of distributed exchange interactions, which are important in amorphous systems. Magnetization and Curie temperature trends in the Fe-Ni MANC system were presented. BH loops for annealed and strain-annealed samples were collected. It was found that alloys more Fe-rich than permalloy gained an increase in permeability, while an alloy more Ni-rich than permalloy decreased permeability. This variation is attributable to the zero crossing of magnetostriction. The maximum measured permeability was 16000. Resistivity was measured for $(\text{Fe}_{70}\text{Ni}_{30})_{80}\text{Nb}_4\text{Si}_2\text{B}_{14}$, and it was found that the strain annealed sample had the highest resistivity, although it also had the most significant oxidation. Virtual bound states were reviewed, and Cr-, V-, Nb-, and Mo-series were made. The affects of these additions on resistivity and magnetic properties were examined. For permeability, it was generally found that strain-annealing the VBS alloys decreased permeability compared to annealing. Lastly, FORC diagrams and Preisach distributions were introduced. AC FORC analysis on $(\text{Fe}_{70}\text{Ni}_{30})_{80}\text{Nb}_4\text{Si}_2\text{B}_{14}$ is ongoing.

It has been demonstrated that there are Fe-Ni MANCs with appropriate magnetic properties for electric motor applications as stated in hypothesis 1. Hypothesis 2 stated that anisotropy could be tuned with strain annealing, which was shown via permeability measurements. The addition of VBS states was shown to

increase the resistivity as proposed in hypothesis 3. VBS additions also affected other magnetic properties such as B_s , H_c , and μ_r as detailed above.

VI. Performance

i. Toroidal Losses

An $(\text{Fe}_{70}\text{Ni}_{30})_{80}\text{Nb}_4\text{Si}_2\text{B}_{14}$ alloy was chosen for further evaluation due to a relatively large saturation magnetization and improved thermal stability as compared to the Ni-rich alloys¹²⁸. The relative amounts of Si and B were varied to produce several different alloys. These were then wound into toroidal cores and annealed at 420 °C, 440 °C, and 460 °C. Toroidal losses were then measured with an

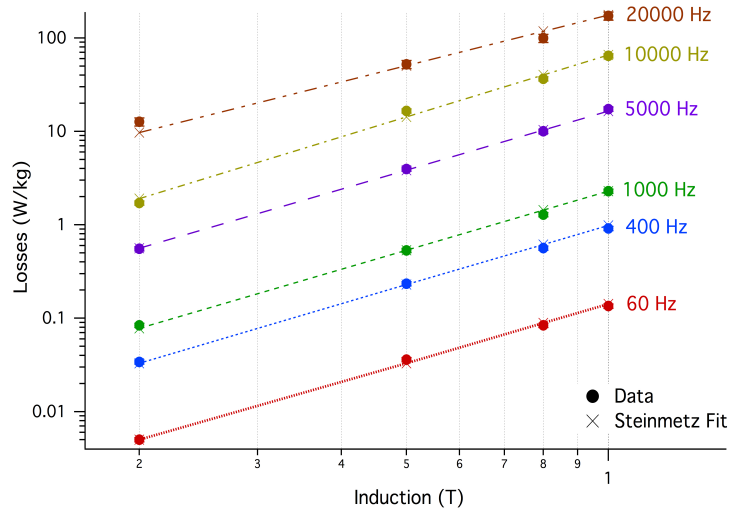


Figure 6.1: Losses for $(\text{Fe}_{70}\text{Ni}_{30})_{80}\text{Si}_2\text{Nb}_4\text{B}_{14}$ and Steinmetz fitting.

induction of .5 T and 10 kHz frequency. Lowest losses are obtained when the cores are annealed at 440 °C, with losses for all compositions between 9 and 15 W/kg. $(\text{Fe}_{70}\text{Ni}_{30})_{80}\text{Nb}_4\text{Si}_2\text{B}_{14}$ was used for more extensive loss measurements as seen in Fig. 6.1. Losses are plotted as a function of peak induction at multiple frequencies, along with Steinmetz fitting (see eq. 1.5.1), which is appropriate for sinusoidal excitations⁴⁸. These losses are lower than recently compiled data for some silicon steels, a Metglas Fe-based amorphous alloy, and a number of Fe-based

nanocomposites¹²⁹. Lower losses have been reported for other Fe-based nanocomposite alloys, but the poor mechanical properties of such alloys make the fabrication of motor components based upon them extremely challenging and raise significant questions about the integrity of fabricated parts during operation⁴⁰. It is also important to point out that while the absolute saturation induction of Si-steels is reported to be between 1.8-2.1 T, the functional B_s of Si-steels are significantly lower due to Goss texturing and greatly reduced permeabilities as induction levels approach 1.5-1.8 T. This reduction in permeability is due to magnetocrystalline anisotropy¹⁷. These results can all be seen in Table VI.I. For the Steinmetz fitting, the fit parameters k , α , and β range from 1 to 1.4, 1.12 to 1.21, and 1.8 to 2.1 respectively.

Table VI.I: Coercivity, saturation induction, thickness, losses at 1 T and 400 Hz, and losses at 1 T and 1 kHz for nanocrystalline $(Fe_{70}Ni_{30})_{79}Nb_4Si_2B_{14}V_1$, $(Fe_{70}Ni_{30})_{79}Nb_4Si_2B_{14}Cu_1$, $(Fe_{70}Ni_{30})_{80}Nb_4Si_2B_{14}$, nanocrystalline $Fe_{85}B_{13}Ni_2$, Fe-based Metglas 2605SA1, and non-oriented 3% Si-steel and 6.5% Si-steel. * H_c measured at 60 Hz and 1 T induction.

	H_c (A/m)	B_s (T)	t (μm)	$W_{1.0/400}$ (W/kg)	$W_{1.0/1k}$ (W/kg)
nc- $(Fe_{70}Ni_{30})_{79}Nb_4Si_2B_{14}V_1$	4.9*	1.1	20	2.1	6.0
nc- $(Fe_{70}Ni_{30})_{79}Nb_4Si_2B_{14}Cu_1$	4.2*	1.3	20	2.1	6.0
nc- $(Fe_{70}Ni_{30})_{80}Nb_4Si_2B_{14}$	7.0*	1.3	20	0.9	2.3
nc- $Fe_{85}B_{13}Ni_2$ ¹²⁹	4.6	1.9	13.4	2.3	6.3
nc- $Fe_{89}Hf_7B_4$ ¹³⁰	5.6	1.59	17	0.61	1.7
Fe-based amorphous ¹²⁹	2.4	1.56	23.9	1.6	4.7
3% Si-Steel ^{21,130}	55	2.05	100	8.5	27.1
6.5% Si-Steel ²¹	18.5	1.85	100	5.7	17.2

Other alloys based on $(\text{Fe}_{70}\text{Ni}_{30})_{80}\text{Nb}_4\text{Si}_2\text{B}_{14}$ were also fabricated, and losses measured. A Cu alloy was chosen due to its altered crystallization kinetics, which

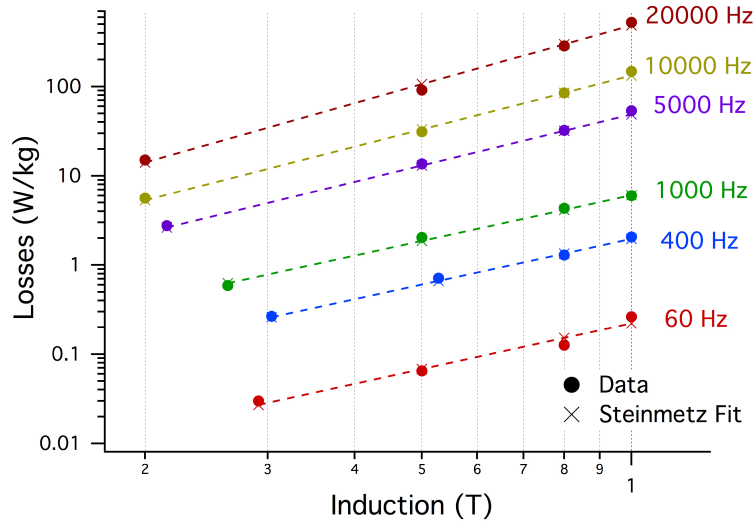


Figure 6.2: Losses for $(\text{Fe}_{70}\text{Ni}_{30})_{79}\text{Si}_2\text{Nb}_4\text{B}_{14}\text{Cu}_1$ and Steinmetz fitting.

may lead to lower hysteretic losses. In addition, a V alloy was chosen due to its higher resistivity, which will reduce eddy current losses. Losses for $(\text{Fe}_{70}\text{Ni}_{30})_{79}\text{Nb}_4\text{Si}_2\text{B}_{14}\text{Cu}_1$ and $(\text{Fe}_{70}\text{Ni}_{30})_{79}\text{Nb}_4\text{Si}_2\text{B}_{14}\text{V}_1$ can be seen in Figures 6.2 and 6.3 respectively. Losses in $(\text{Fe}_{70}\text{Ni}_{30})_{79}\text{Nb}_4\text{Si}_2\text{B}_{14}\text{Cu}_1$ and $(\text{Fe}_{70}\text{Ni}_{30})_{79}\text{Nb}_4\text{Si}_2\text{B}_{14}\text{V}_1$ are

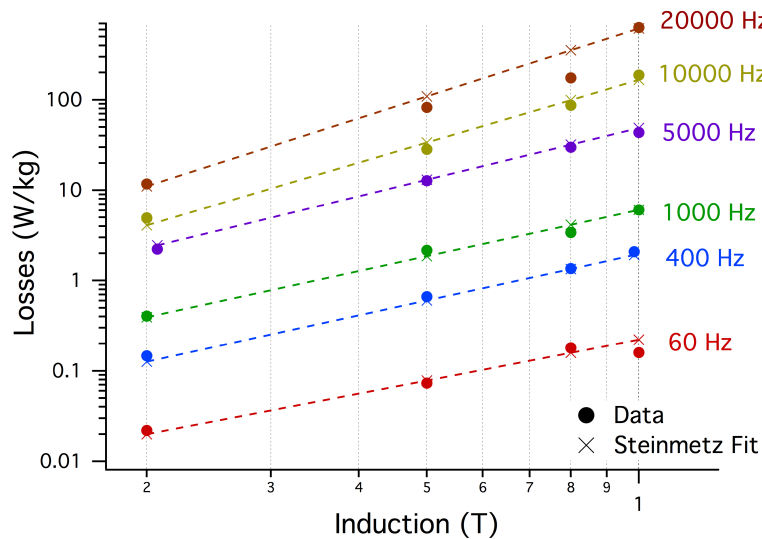


Figure 6.3: Losses for $(\text{Fe}_{70}\text{Ni}_{30})_{79}\text{Si}_2\text{Nb}_4\text{B}_{14}\text{V}_1$ and Steinmetz fitting.

rather similar, but both are higher than the losses shown in Fig. 6.1 for the base alloy. Steinmetz fitting yields k , α , and β values of 2, 1.15, and 1.7 respectively at low frequencies, up to 2.6, 1.25, and 2.5 respectively at high frequencies.

ii. COMSOL Modeling

COMSOL Multiphysics is a powerful tool to model power electronic devices such as electric motors. COMSOL relies on applying finite element computational

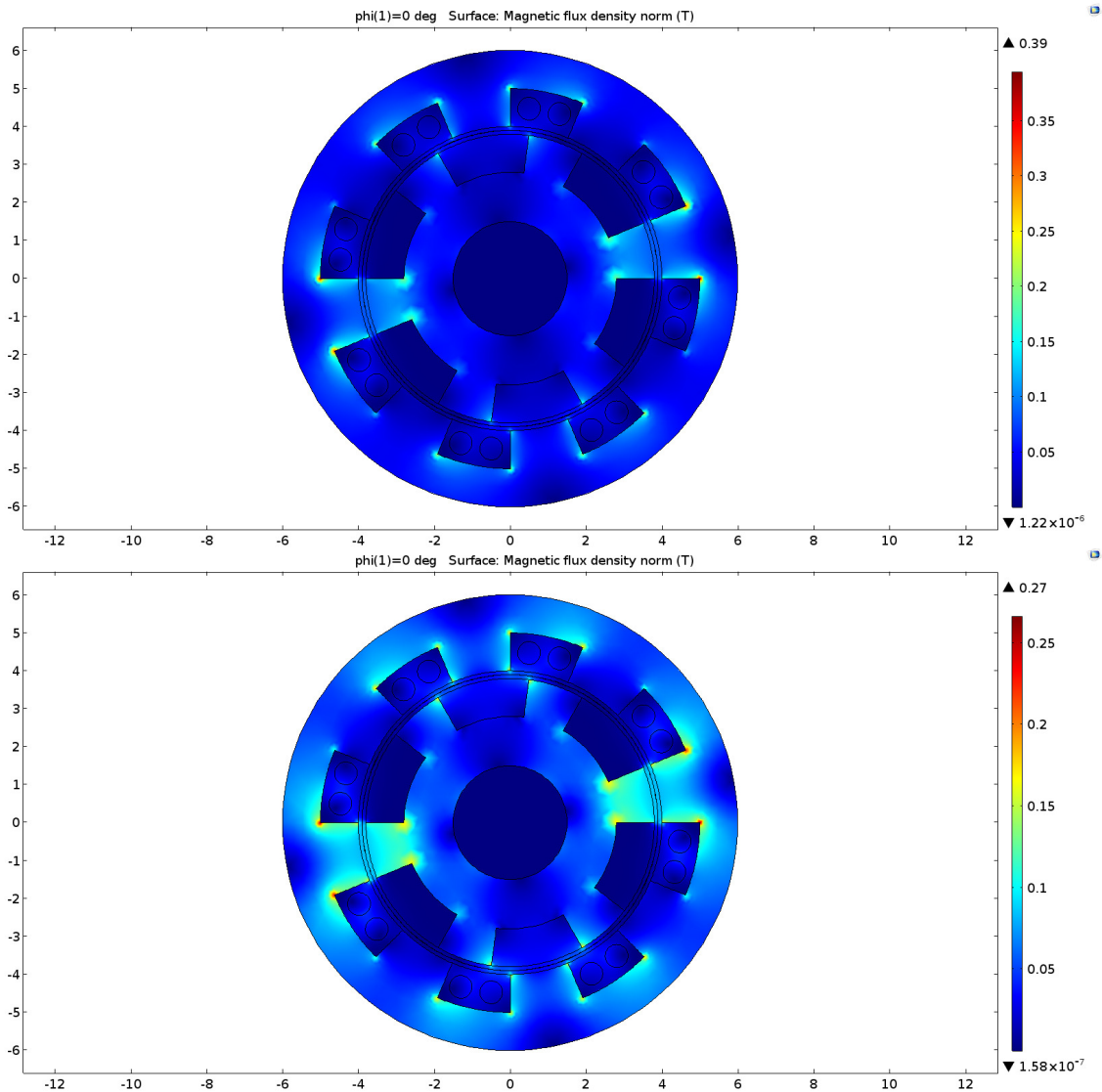


Figure 6.4: (top) flux density for Si-steel, (bottom) flux density for $(\text{Fe}_{70}\text{Ni}_{130})_{80}\text{Nb}_4\text{Si}_2\text{B}_{14}$

methods on a given geometry to solve the relevant physics required. Here, it is used

to model a switched reluctance motor (SRM). We are interested in modeling 2.5 kW motors, and to compare the performance of a 3.5%Si-steel with an Fe-Ni MANC. For ease of modeling, a sinusoidal excitation is used, and magnetic response is modeled using an anhysteretic approximation of the B-H loop.

SRMs are permanent magnet free motors that use induction to turn the rotor. The stator teeth have windings to supply an AC current inducing a magnetization in the stator. The rotor has a smaller number of teeth than the stator. Since the teeth between the rotor and stator are not aligned, the rotor will turn to align the teeth in order to minimize the reluctance. Different stator teeth have different AC phases allowing for continuous rotation.

For this modeling, a COMSOL built-in Si-steel was chosen to compare to $(\text{Fe}_{70}\text{Ni}_{30})_{80}\text{Nb}_4\text{Si}_2\text{B}_{14}$ in an 8-6 SRM. Losses for $(\text{Fe}_{70}\text{Ni}_{30})_{80}\text{Nb}_4\text{Si}_2\text{B}_{14}$ were modeled using the Steinmetz equation with parameters discussed in section 6.1, while Si-steel was modeled using a variant of the Steinmetz equation¹³¹, where the various contributions to the losses are separated as:

$$P_L = k_{hys} f B^\beta + k_{eddy} f^2 B^2 + k_{ano} f^{1.5} B^{1.5} \quad (6.2.1)$$

k 's are the prefactors for hysteretic, eddy, and anomalous losses. Flux densities for the Si-steel and $(\text{Fe}_{70}\text{Ni}_{30})_{80}\text{Nb}_4\text{Si}_2\text{B}_{14}$ can be seen in Fig. 6.4. While the maximum induction is higher in the Si-steel, because the flux is more evenly distributed in the Fe-Ni MANC, integrating the flux density over the surface yields a slightly higher induction in the Fe-Ni MANC than for the Si-steel motor.

To calculate the power output, values of torque are required. Torque can be calculated using Arkkio's method¹³²:

$$\tau = \int \frac{rL B_r B_{phi}}{\mu_0 (g/2)} dr \quad (6.2.2)$$

where B_r is the radial component of the flux density, B_{phi} is the azimuthal component, g is the air gap size, L is the length of the motor, and r is the rotor size. B_r and B_{phi} are in turn calculated from the x- and y-components of the magnetic induction which are calculated using Amperes Law:

$$\Delta \times B = \mu_0 J \quad (6.2.3)$$

Temperature rise can be estimated by²:

$$\Delta T = \frac{P_T h}{\lambda A} \quad (6.2.4)$$

where P_T is the total power loss, h is the thermal path, λ is the thermal conductivity,

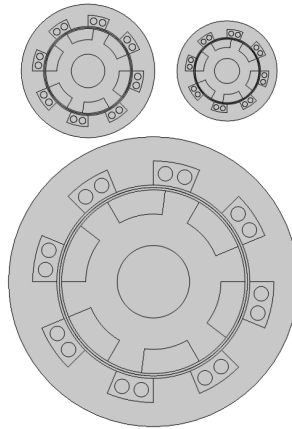


Figure 6.5: Size comparison of Si-steel motors at 60 Hz and 400 Hz, and Fe-Ni MANC at 1 kHz.

and A is the area through which heat can leave the system. Values of thermal conductivity are taken from Rylko et al. (Fe-Ni MANC was assumed to have same thermal conductivity as Fe-based amorphous and Fe-based nanocomposite.)¹³³ For an arbitrarily designed motor with a radius of 6 cm, 20 turns, 15 A input, and run at

1 kHz, the losses with Si-steel are 3.7 W/kg, and for $(\text{Fe}_{70}\text{Ni}_{30})_{80}\text{Nb}_4\text{Si}_2\text{B}_{14}$, the losses are 0.082 W/kg. These lead to temperature changes of 223 °C and 10 °C respectively by equation 6.2.3. A size comparison between a 60 Hz, 400 Hz, and 1 kHz motor, all with 2.5 kW output can be seen in Fig. 6.5. Table VI.II enumerates the specifications for each motor to achieve 2.5 kW output. It should be noted that this geometry is not optimized, and further size reductions could likely be made with further optimization of geometry and input parameters such as number of windings and current.

Table VI.II: A comparison of the materials, frequency, number of windings, current, and scale required for 2.5 kW output for the three motors shown in Fig. 6.3.

Material	Si-Steel	Si-Steel	MANC
Frequency (Hz)	60	400	1000
N_0 (turns)	25	17	10
I (A)	15	8.5	10.5
Scale	1.56	1	0.75

iii. Conclusions

Steinmetz fitting was done for an $(\text{Fe}_{70}\text{Ni}_{30})_{80}\text{Nb}_4\text{Si}_2\text{B}_{14}$ alloy and losses were compared to Si-steel and other amorphous and nanocomposite materials. COMSOL modeling was done for a switched reluctance motor, and $(\text{Fe}_{70}\text{Ni}_{30})_{80}\text{Nb}_4\text{Si}_2\text{B}_{14}$ was compared to a Si-steel. The losses for Si-steel are too high for use at 1 kHz frequency, and size reductions possible by running $(\text{Fe}_{70}\text{Ni}_{30})_{80}\text{Nb}_4\text{Si}_2\text{B}_{14}$ at 1 kHz were demonstrated.

VII. Conclusions and Future Work

The work in this thesis focused on developing new Fe-Ni based metal amorphous nanocomposites. Alloys with a broad range of Fe-Ni compositions were cast and screened for basic magnetic properties, and phase stability of the amorphous phase after primary crystallization. Crystallization products were determined by a variety of techniques. Once a primary alloy of interest was identified, it was thoroughly investigated, and 2nd generation alloys based on it were researched. These 2nd generation alloys consisted of adding various early transition elements to create virtual bound states in order to increase the resistivity. This can be particularly beneficial at high frequencies. This work has contributed the following to the field:

1. A new Fe-rich alloy was identified as being of particular interest due to its high induction and good amorphous phase stability. This alloy is also magnetically stable above temperatures typically seen by electric motors.
2. Strain-annealing can be used as an effective method for tuning the permeability of these alloys. Depending on slight compositional variations, this tuning can be positive or negative.
3. Toroidal core data has demonstrated that these alloys can achieve very low losses. This is particularly interesting in light of their significantly better mechanical properties compared with Fe-based nanocomposite alloys.

Ongoing work includes extending the COMSOL model. This involves adding Cu losses to see how miniaturizing a motor affects these losses as well, and also creating 3-dimensional models. In addition, temperature dependent AC first order

reversal curves (FORC) will be collected on annealed and strain-annealed wide $(\text{Fe}_{70}\text{Ni}_{30})_{80}\text{Nb}_4\text{Si}_2\text{B}_{14}$ samples.

Developing an understanding of the mechanical properties of these alloys is also important from a device standpoint, especially since these materials are being designed for use at high rotational frequencies. To this end, performing temperature dependent tensile tests would be a good place to start. Evaluating the data in light of what is known in the literature regarding the mechanical properties of amorphous ribbons may be fruitful.

Another important aspect of these alloys to understand is the cause of the induced anisotropy. For the recent Co-based alloys, it was shown to be stacking faults that arise from the similar energies of the fcc and hcp phases. However, only bcc and fcc are available in the Fe-Ni system.

This thesis focused on new alloy development, but there are always more alloys that can be tested. For the Fe-Ni MANC system, it may be worth trying to add other transition elements, especially from further down on the periodic table such as tungsten or tantalum. These elements will likely increase resistivity, and may impact mechanical properties as well.

The majority of the work in this thesis was performed on lab scale ribbon, which was typically $\sim 1\text{mm}$ wide. Any device however would require ribbon cast at several inches wide. With wide ribbon, toroidal cores should be made with annealed and strain-annealed ribbon, and magnetic and electrical properties evaluated. For electric motor applications, various topologies will have to be created. The method to be used for cutting is still to be determined, however water-

jet cutting seems to be a likely avenue. Once a cutting method is decided on, a multi kW motor will be built¹³⁴.

References:

- ¹ P. Waide and C.U. Brunner, *Energy-Efficiency Policy Opportunities for Electric Motor-Driven Systems* (2011).
- ² A.M. Leary, P.R. Ohodnicki, and M.E. McHenry, *JOM* **64**, 772 (2012).
- ³ J.M. Silveyra, A.M. Leary, V. DeGeorge, S. Simizu, and M.E. McHenry, *J. Appl. Phys.* **115**, 17A319 (2014).
- ⁴ J.M. Silveyra, P. Xu, V. Keylin, V. DeGeorge, A. Leary, and M.E. McHenry, *J. Electron. Mater.* **45**, 219 (2016).
- ⁵ N. Carsen, R. Fingers, M.E. McHenry, D. Chaumette, and L. Alger, *Risks to the Rare Earth Elements Supply Chain* (2015).
- ⁶ R.G. Eggert, A.S. Carpenter, T.E. Graedel, D.A. Meyer, T. McNulty, B.M. Moudgil, M.M. Poulton, and L.J. Surges, *Minerals, Critical Minerals, and the U.S. Economy* (The National Academies Press, Washington D.C., 2008).
- ⁷ R. Jaffe, J. Price, G. Ceder, R. Eggert, T. Graedel, K. Gschneidner, M. Hitzman, F. Houle, A. Hurd, R. Kelley, A. King, D. Milliron, B. Skinner, and F. Slakey, *Energy Critical Elements: Securing Materials for Emerging Technologies* (2011).
- ⁸ Stormcrow, Stat. - Stat. Portal (2014).
- ⁹ R. Kolano, A. Kolano-Burian, M. Polak, and J. Szynowski, *IEEE Trans. Magn.* **50**, (2014).
- ¹⁰ A.T. de Almeida, F.J.T.E. Ferreira, and G. Baoming, *IEEE Trans. Ind. Appl.* **50**, 2103 (2014).
- ¹¹ N. Ertugrul, R. Hasegawa, W.L. Soong, J. Gayler, S. Kloeden, and S. Kahourzade, *IEEE Trans. Magn.* **51**, 1 (2015).
- ¹² Z. Wang, R. Masaki, S. Morinaga, Y. Enomoto, H. Itabashi, M. Ito, and S. Tanigawa, *IEEE Trans. Ind. Appl.* **47**, 1293 (2011).
- ¹³ M.E. McHenry, M.A. Willard, and D.E. Laughlin, *Prog. Mater. Sci.* **44**, 291 (1999).
- ¹⁴ V. DeGeorge, S. Shen, P. Ohodnicki, M. Andio, and M.E. McHenry, *J. Electron. Mater.* **43**, 96 (2014).
- ¹⁵ M. Kurniawan, V. Keylin, and M.E. McHenry, *J. Mater. Res.* **30**, 2231 (2015).
- ¹⁶ M. Kurniawan, V. Keylin, and M.E. McHenry, *J. Mater. Res.* **30**, (2015).
- ¹⁷ www.infomine.com, (n.d.).
- ¹⁸ www.alfa.com, (n.d.).
- ¹⁹ www.metalprices.com, (n.d.).
- ²⁰ J. Hopkinson, *Philos. Trans. R. Soc. London* **176**, 455 (1885).
- ²¹ C.-W. Chen, *Magnetism and Metallurgy of Soft Magnetic Materials* (Dover Publications, Amsterdam, 1986).
- ²² R.M. Bozorth, *Phys. Rev.* **79**, (1950).
- ²³ D. Jiles, *Introduction to Magnetism and Magnetic Materials*, 3rd ed. (CRC Press, Boca Raton, 1991).
- ²⁴ H.D. Arnold and G.W. Elmen, *J. Franklin Inst.* **195**, 621 (1923).
- ²⁵ F.E. Luborsky, *J. Magn. Mater.* **7**, 143 (1978).
- ²⁶ M.E. McHenry and D.E. Laughlin, *19 - Magnetic Properties of Metals and Alloys*, Fifth Edit (Elsevier B.V., 2015).
- ²⁷ M.E. McHenry and D.E. Laughlin, *Acta Mater.* **48**, 223 (2000).
- ²⁸ Y. Yoshizawa, S. Oguma, and K. Yamauchi, *J. Appl. Phys.* **64**, 6044 (1988).

- ²⁹ K. Suzuki, A. Makino, N. Kataoka, A. Inoue, and T. Masumoto, *Mater. Trans. JIM* **32**, (1991).
- ³⁰ M.A. Willard, D.E. Laughlin, M.E. McHenry, D. Thoma, K. Sickafus, J.O. Cross, and V.G. Harris, *J. Appl. Phys.* **84**, (1998).
- ³¹ H. Ucar, J.J. Ipus, V. Franco, M.E. McHenry, and D.E. Laughlin, *JOM* **64**, 782 (2012).
- ³² H. Ucar, J.J. Ipus, D.E. Laughlin, and M.E. McHenry, *J. Appl. Phys.* **113**, 17A918 (2013).
- ³³ N.J. Jones, H. Ucar, J.J. Ipus, M.E. McHenry, and D.E. Laughlin, *J. Appl. Phys.* **111**, (2012).
- ³⁴ J.J. Ipus, P. Herre, P. Ohodnicki, and M.E. McHenry, *J. Appl. Phys.* **111**, (2012).
- ³⁵ G. Cacciamani, A. Dinsdale, M. Palumbo, and A. Pasturel, *Intermetallics* **18**, 1148 (2010).
- ³⁶ W. Pepperhoff and M. Acet, *Constitution and Magnetism of Iron and Its Alloys* (Springer-Verlag, New York, 2001).
- ³⁷ C.E. Guillaume, *C. R. Acad. Sci.* **125**, (1897).
- ³⁸ J.F. Albertsen, *Phys. Scr.* **23**, 301 (1981).
- ³⁹ M. Kotsugi, C. Mitsumata, H. Maruyama, T. Wakita, T. Taniuchi, K. Ono, M. Suzuki, N. Kawamura, N. Ishimatsu, M. Oshima, Y. Watanabe, and M. Taniguchi, *Appl. Phys. Express* **3**, (2010).
- ⁴⁰ L.H. Lewis, A. Mubarok, E. Poirier, N. Bordeaux, P. Manchanda, A. Kashyap, R. Skomski, J. Goldstein, F.E. Pinkerton, R.K. Mishra, R.C. Kubic Jr, and K. Barmak, *J. Phys. Condens. Matter* **26**, (2014).
- ⁴¹ L.H. Lewis, F.E. Pinkerton, N. Bordeaux, A. Mubarok, E. Poirier, J.I. Goldstein, R. Skomski, and K. Barmak, *IEEE Magn. Lett.* **5**, (2014).
- ⁴² H. Harada, M. Muller, and H. Warlimont, in *Springer Handb. Condens. Matter Mater. Data*, edited by W. Martienssen and H. Warlimont (Springer, New York, 2005), pp. 755–815.
- ⁴³ G. Herzer, in *NATO Sci. Ser. II Math. Phys. Chem.*, edited by B. Idzikowski, P. Svec, and M. Miglierini (Kluwer Academic, Budmerice, Slovakia, 2003).
- ⁴⁴ G. Bertotti, *Hysteresis in Magnetism: For Physicists, Materials Scientists, and Engineers* (Academic Press, New York, 1998).
- ⁴⁵ J.M.D. Coey, *Magnetism and Magnetic Materials* (Cambridge University Press, New York, 2009).
- ⁴⁶ K. Suzuki, G. Herzer, and J.M. Cadogan, *J. Magn. Mater.* **177–181**, 949 (1998).
- ⁴⁷ S. Shen, P.R. Ohodnicki, S.J. Kernion, and M.E. McHenry, *J. Appl. Phys.* **112**, 103705 (2012).
- ⁴⁸ C.P. Steinmetz, *Am. Inst. Electr. Eng. Trans.* **3**, 3 (1892).
- ⁴⁹ A.M. Leary, V. Keylin, P.R. Ohodnicki, and M.E. McHenry, *J. Appl. Phys.* **117**, 17A338 (2015).
- ⁵⁰ P.H. Steen and C. Karcher, *Annu. Rev. Fluid Mech.* **29**, 373 (1997).
- ⁵¹ K. Suzuki, *Mater. Sci. Forum* **312–314**, 521 (1999).
- ⁵² M.A. Willard, *Structural and Magnetic Characterization of HITPERM Soft Magnetic Materials for High Temperature Applications*, Carnegie Mellon University, 2000.
- ⁵³ T.B. Massalski, *Binary Alloy Phase Diagrams* (ASM International, Materials Park, OH, 1990).

- ⁵⁴ T.G. Nieh, J. Wadsworth, C.T. Liu, T. Ohkubo, and Y. Hirotsu, *Acta Mater.* **49**, 2887 (2001).
- ⁵⁵ Y. Kawamura, T. Shibata, A. Inoue, and T. Masumoto, *Scr. Mater.* **37**, 431 (1997).
- ⁵⁶ C.A. Pampillo, *J. Mater. Sci.* **10**, 1194 (1975).
- ⁵⁷ C. Barrett and T.B. Massalski, *Structure of Metals: Crystallographic Methods, Principles, and Data*, 3rd ed. (Pergamon, Oxford, 1980).
- ⁵⁸ S.K. Bhattacharyya, J.H. Perepezko, and T.B. Massalski, *Acta Metall.* **22**, (1974).
- ⁵⁹ J. Friedel, in *Phys. Met.*, edited by J.M. Zinman (Cambridge University Press, New York, 1969), pp. 340–408.
- ⁶⁰ W.A. Johnson and R.F. Mehl, *Trans. AIME* **135**, 396 (1939).
- ⁶¹ M. Avrami, *J. Chem. Phys.* **7**, 103 (1939).
- ⁶² A.N. Kolmogorov, *Bull. Acad. Sci. USSR* 355 (1937).
- ⁶³ H. Hermann, N. Mattern, S. Roth, and P. Uebele, (n.d.).
- ⁶⁴ H. Hermann, *Eur. Lett* **41**, 245 (1998).
- ⁶⁵ D. Crespo and T. Pradell, *Phys. Rev. B* **54**, (1996).
- ⁶⁶ D. Crespo, T. Pradell, M.T. Clavaguera-Mora, and N. Clavaguera, *Phys. Rev. B* **55**, (1997).
- ⁶⁷ T. Pradell, D. Crespo, N. Clavaguera, and M.T. Clavaguera-Mora, *J. Phys. Condens. Matter* **10**, 3833 (1998).
- ⁶⁸ G.S. Rohrer, *Structure and Bonding in Crystalline Materials* (Cambridge University Press, Cambridge, 2001).
- ⁶⁹ V.L. Moruzzi, A.R. Williams, and J.F. Janak, *Phys. Rev. B* **15**, (1977).
- ⁷⁰ J.C. Slater, *J. Appl. Phys.* **8**, 385 (1937).
- ⁷¹ L. Pauling, *Phys. Rev.* **54**, 899 (1938).
- ⁷² I.W. Donald and H.A. Davies, *Philos. Mag. A* **42**, 277 (1980).
- ⁷³ M.E. McHenry, F. Johnson, H. Okumura, T. Ohkubo, V.R.V. Ramanan, and D.E. Laughlin, *Scr. Mater.* **48**, 881 (2003).
- ⁷⁴ A. Hsiao, *The Crystallization Kinetics of Fe-Zr-Based Amorphous and Nanocrystalline Soft Magnetic Materials*, Carnegie Mellon University, 2001.
- ⁷⁵ H.E. Kissinger, *Anal. Chem.* **29**, 1702 (1957).
- ⁷⁶ J.A. Augis and J.E. Bennett, *J. Therm. Anal.* **13**, 283 (1978).
- ⁷⁷ F.J. Gotor, J.M. Criado, and J. Málek, (n.d.).
- ⁷⁸ M.E. McHenry and D.E. Laughlin, in *Phys. Metall.*, 5th ed. (2015).
- ⁷⁹ S.J. Kernion, K.J. Miller, S. Shen, V. Keylin, J. Huth, and M.E. McHenry, *IEEE Trans. Magn.* **47**, 3452 (2011).
- ⁸⁰ J. Šesták, *Thermophysical Properties of Solids - Their Measurements and Theoretical Thermal Analysis* (Elsevier, Amsterdam, 1984).
- ⁸¹ E.J. Mittemeijer, *J. Mater. Sci.* **27**, 3977 (1992).
- ⁸² V. DeGeorge, E. Zoghlin, V. Keylin, and M. McHenry, *J. Appl. Phys.* **117**, 17A329 (2015).
- ⁸³ J. Schroers, *JOM* **57**, (2005).
- ⁸⁴ S. Ding, Y. Liu, Y. Li, Z. Liu, S. Sohn, F.J. Walker, and J. Schroers, *Nat. Mater.* **13**, (2014).
- ⁸⁵ Z. Alam, D. Eastman, M. Jo, and K. Hemker, *JOM* **68**, 2754 (2016).
- ⁸⁶ M. Daniil, P.R. Ohodnicki, M.E. McHenry, and M.A. Willard, *Philos. Mag.* **90**, 1547 (2010).

- ⁸⁷ M.A. Willard, D.E. Laughlin, and M.E. McHenry, *J. Appl. Phys.* **87**, 7091 (2000).
- ⁸⁸ K.A. Gallagher, M.A. Willard, V.N. Zabenkin, D.E. Laughlin, and M.E. McHenry, *J. Appl. Phys.* **85**, 5130 (1999).
- ⁸⁹ A. Yamada, Y. Wang, T. Inoue, W. Yang, C. Park, T. Yu, and G. Shen, *Rev. Sci. Instrum.* **82**, 015103 (2011).
- ⁹⁰ Y. Kono, C. Park, C. Kenney-Benson, G. Shen, and Y. Wang, *Phys. Earth Planet. Inter.* **228**, 269 (2014).
- ⁹¹ M. Abuin, Z. Turgut, N. Aronhime, V. Keylin, A. Leary, V. DeGeorge, J. Horwath, S.L. Semiatin, D.E. Laughlin, and M.E. McHenry, *Metall. Mater. Trans. A* **46**, 5002 (2015).
- ⁹² D.L. Anderson, in *Theory of the Earth* (Blackwell Scientific Publications, Boston, 1989), pp. 79–102.
- ⁹³ B. Buras, W.I.F. David, L. Gerward, J.D. Jorgensen, and B.T.M. Willis, in *Int. Tables Crystallogr.* (International Union of Crystallography, Chester, England, 2006), pp. 84–88.
- ⁹⁴ S.M. Clark, *Crystallogr. Rev.* **8**, 57 (2002).
- ⁹⁵ M.-A.A. Van Ende and I.-H.H. Jung, *J. Alloys Compd.* **548**, 133 (2013).
- ⁹⁶ M.E. McHenry, S.A. Majetich, J.O. Artman, M. DeGraef, and S.W. Staley, *Phys. Rev. B* **49**, (1994).
- ⁹⁷ D. Apel, M. Klaus, C. Genzel, and D. Balzar, *Zeitschrift Fur Krist.* **226**, 934 (2011).
- ⁹⁸ F. Faupel and K. Rätzke, in *Diffus. Condens. Matter* (Springer-Verlag, Berlin/Heidelberg, 2005), pp. 249–282.
- ⁹⁹ A.T. Dinsdale, *CALPHAD* **15**, 317 (1991).
- ¹⁰⁰ T.B. Massalski and D.E. Laughlin, *Calphad* **33**, 3 (2009).
- ¹⁰¹ A. Inoue, A. Takeuchi, A. Makino, and T. Masumoto, *Mater. Trans. JIM* **36**, 962 (1995).
- ¹⁰² P.R. Ohodnicki, Y. Hanlumyuang, D.E. Laughlin, and M.E. McHenry, *Metall. Mater. Trans. A* **38**, (2007).
- ¹⁰³ Y. Hanlumyuang, P.R. Ohodnicki, D.E. Laughlin, and M.E. McHenry, *J. Appl. Phys.* **99**, 8 (2006).
- ¹⁰⁴ P.R. Ohodnicki, N.C. Cates, D.E. Laughlin, M.E. McHenry, and M. Widom, *Phys. Rev. B* **78**, 144414 (2008).
- ¹⁰⁵ J. Long, P.R. Ohodnicki, D.E. Laughlin, M.E. McHenry, T. Ohkubo, and K. Hono, *J. Appl. Phys.* **101**, (2007).
- ¹⁰⁶ H.R. Schober, *Phys. Rev. Lett.* **88**, (2002).
- ¹⁰⁷ H. Mehrer, *Diffusion in Solids* (Springer-Verlag, New York, 2007).
- ¹⁰⁸ F. Ye and K. Lu, *Acta Mater.* **47**, 2449 (1999).
- ¹⁰⁹ R.M. Bozorth, *Ferromagnetism* (van Nostrand, New York, 1951).
- ¹¹⁰ J.C. Slater, *Phys. Rev.* **36**, 57 (1930).
- ¹¹¹ S. Ishio, T. Kobayashi, H. Saito, S. Sugawara, and S. Kadowaki, *J. Magn. Magn. Mater.* **164**, 208 (1996).
- ¹¹² C.W.T. McLyman, *TRANSFORMER AND INDUCTOR DESIGN HANDBOOK*, 3rd ed. (Marcel Dekker Inc., New York, 2004).
- ¹¹³ F. Landgraf and M. Emura, *J. Magn. Magn. Mater.* **242–245**, 152 (2002).
- ¹¹⁴ J.C. Bavay and J. Verdun, *J. Mater. Eng. Perform.* **2**, 169 (1993).
- ¹¹⁵ A. Leary, V. Keylin, A. Devaraj, V. DeGeorge, P. Ohodnicki, and M.E. McHenry, *J. Mater. Res.* **23**, 1 (2016).

- ¹¹⁶ A. Hsiao, M.E. McHenry, D.E. Laughlin, M.J. Kramer, C. Ashe, and T. Ohkubo, *IEEE Trans. Magn.* **38**, 3039 (2002).
- ¹¹⁷ N.F. Mott and H. Jones, *The Theory of the Properties of Metals and Alloys* (Oxford, 1936).
- ¹¹⁸ P.L. Rossiter, *The Electrical Resistivity of Metals and Alloys* (Cambridge University Press, New York, 1987).
- ¹¹⁹ P. Drude, *Ann. Phys.* **308**, (1900).
- ¹²⁰ P. Drude, *Ann. Phys.* **306**, (1900).
- ¹²¹ T. Fujiwara, *J. Phys. F Met. Phys.* **9**, (1979).
- ¹²² H. Ebert, (n.d.).
- ¹²³ V. DeGeorge, *Chemical and Electronic Structure of Co-Based Magnetic Nanocomposites for Electric Motors*, Carnegie Mellon University, 2017.
- ¹²⁴ V.A. Gubanov, A.I. Liechtenstein, and A. V. Postnikov, *Magnetism and the Electronic Structure of Crystals* (Springer-Verlag, New York, 1992).
- ¹²⁵ B. Drittler, N. Stefanou, S. Bliigel, R. Zeller, and P.H. Dederichs, *Phys. Rev. B* **40**, (1989).
- ¹²⁶ N. Aronhime, V. DeGeorge, V. Keylin, P. Ohodnicki, and M.E. McHenry, *JOM* **69**, 2164 (2017).
- ¹²⁷ A.P. Roberts, D. Heslop, X. Zhao, and C.R. Pike, *Rev. Geophys.* **52**, 557 (2014).
- ¹²⁸ N. Aronhime, E. Zoghlin, V. Keylin, X. Jin, and M.E. McHenry, in *Magn. Magentic Mater.* (New Orleans, 2016).
- ¹²⁹ K. Suzuki, R. Parsons, B. Zang, K. Onodera, H. Kishimoto, and A. Kato, *Appl. Phys. Lett.* **110**, 012407 (2017).
- ¹³⁰ K. Suzuki, A. Makino, A. Inoue, and T. Masumoto, *J. Appl. Phys.* **74**, 3316 (1993).
- ¹³¹ J.M. Silveyra, S. Simizu, and M.E. McHenry, in *TMS* (San Diego, 2017).
- ¹³² A. Arkkio, *Analysis of Induction Motors Based on the Numerical Solution of the Magnetic Field and Circuit Equations*, Helsinki University of Technology, 1987.
- ¹³³ M.S. Rylko, K.J. Hartnett, J.G. Hayes, and M.G. Egan, in *2009 Twenty-Fourth Annu. IEEE Appl. Power Electron. Conf. Expo.* (IEEE, 2009), pp. 2043–2049.
- ¹³⁴ S. Simizu, P.R. Ohodnicki, and M.E. McHenry, *IEEE Trans. Magn.* **PP**, 1 (2018).